Induced uniaxial magnetic anisotropy in polycrystalline, single crystal and superlattices of permalloy

Movaffaq Kateb

Faculty of Physical Sciences
University of Iceland
2019

Induced uniaxial magnetic anisotropy in polycrystalline, single crystal and superlattices of permalloy

Movaffaq Kateb

Dissertation submitted in partial fulfillment of a
Philosophiae Doctor degree in Applied Physics

Advisor
Snorri Þorgeir Ingvarsson

PhD Committee
Snorri Þorgeir Ingvarsson
Jón Tómas Guðmundsson
Friðrik Magnus

Opponents
Sigurður Ingi Erlingsson
Victor Kuncser

Faculty of Physical Sciences
School of Engineering and Natural Sciences
University of Iceland
Reykjavik, December 2019

Induced uniaxial magnetic anisotropy in polycrystalline, single crystal and superlattices of permalloy
Magnetic anisotropy
Dissertation submitted in partial fulfillment of a *Philosophiae Doctor* degree in Applied Physics

Faculty of Physical Sciences
School of Engineering and Natural Sciences
University of Iceland
Dunhaga 3
107, Reykjavik
Iceland

Telephone: 525-4000

Bibliographic information:
Movaffaq Kateb, 2019, *Induced uniaxial magnetic anisotropy in polycrystalline, single crystal and superlattices of permalloy*, PhD dissertation, Faculty of Physical Sciences, University of Iceland, 110 pp.

ISBN 978-9935-9452-3-5

Printing: Háskólaprent, Fálkagata 2, 107 Reykjavík
Reykjavik, Iceland, December 2019

Abstract

Permalloy $Ni_{80}Fe_{20}$ atomic % (which will be referred to as Py here after) is a well-known ferromagnet utilized in anisotropic magnetoresistance and planar Hall effect sensors as well as magnetic read heads in magnetic memories. These applications rely on the *uniaxial magnetic anisotropy* in permalloy thin films. Various methods have been developed to achieve uniaxial anisotropy such as post-annealing, *in-situ* growth and ion beam irradiation in the presence of a magnetic field, deposition under an angle with respect to the substrate normal and mechanical deformation. Among these we found tilt deposition as the most general case since most of ferromagnetic films are grown in co-deposition vacuum systems under an angle.

In the first stage we compared the effect of tilt deposition with that of applying *in-situ* magnetic field, in definition of the easy magnetization axis direction, and showed that in a competition of both effects, the former has a major effect (paper I). It has also been shown that tilt deposition gives very well-defined uniaxial anisotropy over a wide range of working gas pressures (paper II). Since the sputter flux might scatter off at higher pressures, utilizing high power impulse magnetron sputtering (HiPIMS) is required to provide higher adatom energy and maintain high mass density and magnetic softness of the Py films. Then it is shown that very well-defined uniaxial anisotropy can be achieved in a series of Py films, with variable thicknesses. This is achieved in the absence of self-shadowing and off-normal texture which have been mentioned in the literature to explain the origin of uniaxial anisotropy (paper III). None of these, however, explained the origin of induced uniaxial anisotropy in Py films. Thus in the second stage we deposited single crystal Py films on (001) MgO using tilt geometry and made a systematic comparison of dc magnetron sputtering (dcMS) and HiPIMS (paper IV). Based on X-ray diffraction (XRD) and resistivity measurements it has been demonstrated that single crystal films prepared by dcMS present an ordered microstructure towards $L1_2$ Ni_3Fe superlattice while the high instantaneous deposition rate of HiPIMS (more 50 times of dcMS during the pulse) gives a disordered single crystal. Surprisingly, the single crystal prepared by HiPIMS showed uniaxial behavior along the $\langle 001 \rangle$ orientation. The more ordered single crystal grown by dcMS presented biaxial anisotropy along the $\langle 011 \rangle$ orientation which is in agreement with magnetocrystalline anisotropy along the $\langle 111 \rangle$ orientation and being forced into the film plane by the demagnetization field (shape anisotropy). It is worth mentioning that previously post annealing and *in-situ* magnetic field failed to induce uniaxial anisotropy along the $\langle 001 \rangle$ orientation. The latter controversy can be explained by the fact that normally very low deposition rates are utilized for the growth of single crystals. Thus they were unable to achieve enough disorder required for uniaxial anisotropy to appear. Later it is shown that although it is very hard to detect the atomic order using XRD in polycrystalline films, one can utilize resistivity

measurements to study the microscopic origin of uniaxial anisotropy (Paper IV). It has been shown that the resistivity of a film prepared by *in-situ* field is minimum along the hard axis and maximum along the easy axis. We explain this by atomic arrangement of Ni and Fe (or *order*) along the easy axis of the film.

In order to study interface or surface anisotropy, we prepared multilayers of Py using dcMS and HiPIMS. It was shown that a sharp interface can be achieved using the HiPIMS method. However, this is accompanied by large strain in the case of Py/Pt that increases coercivity and gives an open hard axis. On the other hand, Py/X using Cu or CuPt as spacer, X, exhibit well defined uniaxial anisotropy.

Útdráttur

Permalloy $Ni_{80}Fe_{20}$ samsetning (Py) er vel þekktur járnsegull, notaður í anisotropic magnetoresistance og planar Hall effect skynjara ásamt því að vera nýttur í leshausa harðra diska í tölvum og í segulminni. Þessar hagnýtingar reiða sig á einása seguláttun í permalloy þunnhúðum. Ýmsar aðferðir hafa verið þróaðar til þess að ná einása seguláttun í efninu, svo sem að setja á segulsvið við bökun eftir ræktun, á meðan á ræktun stendur, eða við jónaágeislun. Einnig með ræktun undir hvössu horni og, að síðustu, aflfræðileg bjögun. Á meðal þessara aðferða höfum við mest beitt ræktun undir hvössu horni, en eitt ræktunartækið okkar er einmitt þannig hannað að ræktun fer öll fram undir hvössu horni.

Í fyrsta hluta þessa verkefnis bárum við saman áhrif ræktunar undir hvössu horni og beitingu segulsviðs á spönun einása seguláttunar og sýndum að í samkeppni þeirra á milli þá hafði fyrri aðferðin betur (grein I). Við sýndum líka að ræktun undir hvössu horni veldur mjög vel skilgreindri einása seguláttun jafnvel á breiðu sviði ræktunarþrýstings (grein II). Þar sem spættar jónir gætu skondrað af undirlaginu við háan ræktunarþrýsting, í stað þess að festast, þá nýtum við háaflspúlsaða segulspætun (HiPIMS) til þess að auka orku þeirra og viðhalda þannig háum massaþéttleika og mjúkri segulhegðun Py húðanna. Þá sýnum við hvernig mjög góðri einása seguláttun var náð í röð Py-sýna af mismunandi þykkt. Það var án nokkurar sjálfskýlingar eða hallandi frumeindauppröðunar, hvort tveggja skýringar sem notaðar hafa verið fyrir uppruna einása seguláttunar (grein III). Hvorug þeirra getur hins vegar verið ástæða seguláttunar í okkar Py húðum. Í næsta fasa verkefnisins ræktuðum við því einkristallaðar Py húðir á (001) MgO, undir hvössu horni og bárum saman dc segulspætun (dcMS) og HiPIMS (grein IV). Á grundvelli röntgenmælinga (XRD) og rafviðnámsmælinga getum við sagt að einkristallaðar húðir ræktaðar með dcMS leiða til reglulegrar kristalbyggingar með $L1_2$ Ni_3Fe ofurgrind en mikill ræktunarhraði í HiPIMS (meira en 50-faldur dcMS ræktunarhraði á meðan á púlsi stendur) gefur óreglulegri kristalbyggingu. Það kom á óvart að einkristallaðar húðir ræktaðar með HiPIMS höfðu einása seguláttun í $\langle 001 \rangle$ stefnu. Hins vegar leiddi reglulega kristalbyggingin sem kom með dcMS ræktun til tvíása seguláttunar í $\langle 011 \rangle$ stefnur, sem rímar við að seguláttun í bolefninu er í $\langle 111 \rangle$ stefnur, en er þvinguð niður í planið af afsegulmögnunarþættinum vegna lögunar þunnhúðarinnar. Vert er að nefna að hvorki segulsvið í ræktun né bökun að lokinni ræktun dugðu til að spana einása seguláttun í $\langle 001 \rangle$ stefnu. Það kann að stafa meðal annars af því að við ræktun einkristalla er notaður mjög lágur ræktunarhraði. Því verður ekki næg óregla í byggingunni til þess að valda einása seguláttun. Við sýndum síðar að jafnvel þótt mjög erfitt sé að nema óreglu í frumeindaröðun með XRD í fjölkristölluðum húðum þá má nota rafviðnámsmælingar til þess að segja eitthvað til um uppruna einása seguláttunar (grein IV). Við sýndum að eðlisviðnám húðar sem var ræktuð í segulsviði er í lágmarki í stefnu harða segulássins

en í hámarki í stefnu auðvelda segulássins. Við færum rök fyrir þessu með röðun frumeindanna Ni og Fe í stefnu auðvelda seguláss húðarinnar.

Til þess að rannsaka áhrif yfirborðs eða yfirborðsáttun útbjuggum við marglög, sem innihalda Py, með dcMS og HiPIMS. Við sýndum að það er hægt að fá mjög skörp, vel skilgreind, skil með HiPIMS aðferð. Þessu fylgir hins vegar töluverð bjögun efnisins í tilfellinu Py/Pt sem eykur coercivity og eykur á segulheldni eftir erfiða segulásnum. Ef notað er Cu eða CuPt í stað Pt fæst vel skilgreind einása seguláttun.

Dedication

To Sahar, Amirhossein, Taha and Yasin who make my life more than what I value.

Table of Contents

Abstract iii

Útdráttur v

Dedication vii

Table of Contents ix

List of Figures xi

List of Tables xv

List of Original Papers xvii

Abbreviations xix

Acknowledgments xxiii

1 Introduction 1

1.1 Introduction . . . 1

1.2 Thesis outline . . . 1

2 Phenomenology of magnetic anisotropy 3

2.1 Energy terms . . . 3

2.2 Zeeman energy . . . 4

2.3 Shape anisotropy . . . 4

2.4 Magnetocrystalline anisotropy . . . 6

2.4.1 Physical origin of magnetocrystalline anisotropy . . . 6

2.4.2 Cubic anisotropy . . . 6

2.4.3 Uniaxial anisotropy . . . 8

2.4.4 Permalloy . . . 9

2.4.5 Polycrystalline permalloy . . . 9

2.5 Induced Magnetic Anisotropy . . . 9

2.5.1 Post annealing . . . 10

2.5.2 Tilt deposition . . . 11

2.5.3 Ion irradiation . . . 11

2.5.4 Plastic deformation . . . 12

2.6 Exchange anisotropy . . . 13

2.7 Stress anisotropy . . . 14

2.8 The origin of induced uniaxial anisotropy in permalloy . . . 15

2.8.1 Magnetostriction . . . 15

2.8.2 Pair ordering . . . 16

2.8.3 Shape anisotropy of ordered phase . . . 17

2.8.4 Corrected directional order . . . 17

2.8.5 Atomic order . . . 18

3 Preparation and measurements 21
3.1 Thin film deposition . . . 21
3.1.1 dcMS . . . 21
3.1.2 HiPIMS . . . 22
3.1.3 Importance of ionization fraction . . . 23
3.1.4 Advantage of HiPIMS for magnetic materials . . . 25
3.2 Anisotropic magnetoresistance . . . 27
3.3 Anisotropic magnetoresistance measurement . . . 27
3.3.1 Anisotropic resistivity measurement . . . 29
3.3.2 van der Pauw measurement . . . 29
3.3.3 Price extension to anisotropic medium . . . 30
3.3.4 Kleiza extension to anisotropic medium . . . 31
3.3.5 Extended van der Pauw method of anisotropic magnetoresistance measurement 31
4 Uniaxial anisotropy induced by tilt deposition 33
4.1 Polycrystalline permalloy film . . . 33
4.1.1 Tilt deposition vs *in-situ* magnetic field . . . 33
4.1.2 Effect of self-shadowing . . . 34
4.1.3 Comparison of dcMS and HiPIMS . . . 36
4.2 Permalloy single crystal . . . 38
4.2.1 Characterization single crystals . . . 38
4.2.2 Inducing uniaxial anisotropy using HiPIMS . . . 40
4.2.3 Proof of atomic order via AMR measurement . . . 41
4.3 The origin of uniaxial anisotropy induced by tilt angle . . . 42
4.4 Magnetic anisotropy in permalloy multilayers . . . 44
4.4.1 Strain and texture . . . 44
4.4.2 Interface roughness and mixing . . . 45
4.4.3 Magnetic behavior . . . 47
4.4.4 The interplay between intermixing and magnetic property . . . 48
5 Summary and conclusion 51
6 Summary of papers 53
Paper I 54
Paper II 60
Paper III 69
Paper IV 82
Paper V 91
References 100
7 Appendix MOKE 109
7.1 Kerr effect . . . 109
7.2 Faraday effect . . . 110

List of Figures

2.1 Schematic illustration of $M-H$ loops along different directions (Cullity and Graham, 1972, p. 317). . . . 4
2.2 Division of a crystal into domains will reduce magnetostatic energy (Cullity and Graham, 1972, p. 293). . . . 5
2.3 Schematic illustration of spin–orbit–lattice interaction (Cullity and Graham, 1972, p. 205) . . . 6
2.4 Magnetization curves for (a) bcc iron and (b) fcc Ni crystals along selected crystal orientation (Cullity and Graham, 1972, p. 199). . . . 7
2.5 Variation of domain structures in a single-crystal disk with H applied in the easy direction. (Cullity and Graham, 1972, p. 200). . . . 7
2.6 Variation of domain structures in a single-crystal disk with H applied in the hard direction. (Cullity and Graham, 1972, p. 201). . . . 7
2.7 Polar plots of magnetocrystalline anisotropy (E_{ca}) for the cubic anisotropy cases (left) $K_1 > 0$ and (right) $K_1 < 0$ with their minimum along the [100] and [111], respectively (d'Aquino, 2004) . . . 8
2.8 Uniaxial anisotropy with (left) easy axis $K_{u1} > 0$ and (right) easy plane $K_{u1} < 0$ (d'Aquino, 2004) . . . 9
2.9 Schematic illustration of a material with positive magnetostriction (Cullity and Graham, 1972, p. 257). . . . 10
2.10 Uniaxial anisotropy and direction of magnetic axes determined by the tilt geometry. . . . 11
2.11 Schematic illustration of self-shadowing (Kwon et al., 2015). . . . 11
2.12 Uniaxial anisotropy constant K_{u1} of rolled polycrystalline NiFe alloys. (a) Randomly oriented grains rolled to 33% reduction in thickness. (b) [100]-textured material rolled to 55% reduction (Cullity and Graham, 1972, p. 350). . . . 13
2.13 Effect of 10000 lb/in^2 (69 MPa) tensile (+) and compressive (−) stress on the $M-H$ behavior of Polycrystalline nickel (Cullity and Graham, 1972, p. 259). . . . 14
2.14 Schematic illustration of a material with positive magnetostriction under tensile stress. . . . 15
2.15 The different superlattices that can be found in the Fe–Ni system (Vernyhora et al., 2012). . . . 16
2.16 Variation of K_{u1} with the composition of Fe–Ni system (Chikazumi and Oomura, 1955). . . . 17

3.1 The discharge current-voltage waveform at different pressures, for a 75 mm diameter $Ni_{80}Fe_{20}$ target with Ar as working gas. The line style of the legend applies to both discharge voltage and current traces. 23
3.2 The surface topology obtained using (a) thermal evaporation (b) dcMS and (b) HiPIMS deposition with similar deposition time and energy distribution. The deep blue indicates substrate surface and red denotes 6 nm above the substrate surface. 24
3.3 The sequence of amorphization and crystallization during HiPIMS deposition due to high energy ion bombardment. (a) Before collision at 890 ps, (b) right after high energy collision at 892 ps, and (c – d) after secondary collisions at 906 – 910 ps. The red, green, blue and white atoms respectively are fcc, hcp, bcc and disordered atoms. 25
3.4 Schematic illustration of growth of multilayer using (a) HiPIMS and (b) dcMS. The black, white and gray atoms respectively are substrate, underlayer and top layer atoms. Arrows are indicating probability of diffusion. 26
3.5 Typical AMR measurement of Py film obtained by sweeping magnetic field parallel (orange) and perpendicular (gray) to the current probes. . . . 28
3.6 Typical AMR measurement of Py film obtained by rotation of M_{sat} and fixed current probes. 29
3.7 Schematic illustration of two sets of measurements in the vdP method. . . 30
3.8 Schematic illustration of (left) five points (Ašmontas et al., 2008) and (right) reshaping (Kleiza et al., 2007) methods for determining full resistivity tensor of the film. 31
4.1 The measured and fit XRR curves of different Py films with 10–250 nm thicknesses. The curves have been offset manually in the vertical direction for clarity. 34
4.2 Pole figures of the (111) planes of 50–250 nm thick films. Raw data (left) before, (middle) after subtracting the substrate and (right) after subtracting the next thinner film patterns. The white line indicates the direction of the sputtered flux during stop time. Colorbar indicate normalized intensity. 35
4.3 Variation of resistivity with the film thickness in present study in comparison with Solt (1985) result. The solid black line in our result is plotted to aid the eye. The dashed line indicate the best fit to Fuchs (1938) model. 36
4.4 The MOKE response of the films deposited by dcMS and HiPIMS at room temperature measured along hard and easy axes of the films. 37
4.5 The (a) anisotropy field (H_k) and (b) coercivity field (H_c) of the film deposited with the same thickness at different working gas pressures. These values extracted from MOKE measurements along hard and easy axis, respectively. The figure inset shows density variation at different pressures. 37
4.6 The symmetric XRD pattern of the epitaxial films deposited by dcMS and HiPIMS. The vertical dashed lines show the peak position of bulk Py and MgO. The curves are shifted manually for clarity. 39

4.7 The pole figures obtained for Py {111}, {200} and {220} planes of epitaxial films deposited by dcMS and HiPIMS. The height represents normalized log intensity (arb. units). 40
4.8 The average hysteresis loops of the epitaxial films obtained by MOKE measurements along the [100] and [110] directions of the epitaxial Py films. 41
4.9 The AMR obtained by resistivity measurements along the [100] directions of Py films deposited by (a – b) dcMS and (c – d) HiPIMS during rotation of 24 Oe magnetic field. The θ here stands for angle of in-plane magnetization with the $\langle 100 \rangle$ direction. The black lines indicate the result of fitting with Eq. (3.5). The vertical dashed lines indicate the direction of easy axes. 42
4.10 Single crystal Py (111) and (002) peaks obtained by dcMS and HiPIMS using tilt ($\angle$) and normal ($\perp$) geometry. The vertical dashed lines indicate peak position for the bulk. All these sample grown at same power density of 1.91 W/cm^2 except HiPIMS* which is grown at 3 times larger power density. 43
4.11 XRD patterns of Py/Pt multilayers deposited on p-Si (001) with native oxide and 100 nm thermally grown oxide. The legend indicates method and sputtering power utilized for Py deposition while Pt layers were deposited by dcMS at 20 W. The vertical dashed lines in black and red are indicating (111) peak position for the bulk Pt and Py, respectively. . . 45
4.12 Comparison of Py/Pt multilayer deposited on p-Si (001) with native oxide and 100 nm thermally grown oxide. The legend indicates sputtering method and power utilized for Py while Pt layers deposited by dcMS at 20 W. The vertical dashed lines in black critical angle θ_c. δ, Δ and Λ are proportional to the total thickness, Ta under-layer thickness and repetition thickness, respectively. 46
4.13 The MOKE response of Py/Pt multilayer deposited on the p-Si (001) with native oxide and 100 nm thermally grown oxide. The legend indicates sputtering method and power utilized for Py deposition while the Pt layers were deposited by dcMS at 20 W. 48
4.14 The MOKE response of Py/(Cu, CuPt and Pt) multilayer deposited at 0.25/0.4 Pa on p-Si (001) substrate with a smooth 100 nm thermally grown oxide. In all cases Py layers has been deposited by HiPIMS while spacer layers were deposited by dcMS. 49
7.1 The principle of domain characterization by MOKE. 109

List of Tables

4.1 Resistivity measurements along hard and easy axes of 40 nm thick polycrystalline film grown by normal deposition within *in-situ* magnetic field and tilt deposition with assisting field. 43
4.2 Values of layers thickness (t), density (ρ) and surface roughness (R) obtained by fitting the XRR measurement results. 47

List of Original Papers

Papers included in thesis

I: M. Kateb & S. Ingvarsson, Thickness-dependent magnetic and magnetoresistance properties of permalloy prepared by field assisted tilt sputtering, **2017 IEEE Sensors Applications Symposium (SAS)** (2017) 1–5.

II: M. Kateb et al., Comparison of magnetic and structural properties of permalloy $Ni_{80}Fe_{20}$ grown by dc and high power impulse magnetron sputtering, **Journal of Physics D: Applied Physics 51** (28) 2018, 285005 (8pp).

III: M. Kateb et al., Application of an extended van der Pauw method to anisotropic magnetoresistance measurements of ferromagnetic films, **Journal of Physics D: Applied Physics 52** (7) 2019, 075002 (12pp).

IV: M. Kateb et al., Effect of atomic ordering on the magnetic anisotropy of single crystal $Ni_{80}Fe_{20}$, **AIP Advances 9** (3) 2019, 035308 (5 pp).

V: M. Kateb et al., Role of ionization fraction on the surface roughness, density, and interface mixing of the films deposited by thermal evaporation, dc magnetron sputtering, and HiPIMS: An atomistic simulation, **Journal of Vacuum Science & Technology A 37** (3) 2019, 031306 (8 pp).

Papers not included in thesis

I: H. Hajihoseini, M. Kateb, S. Ingvarsson & J. T. Gudmundsson, Oblique angle deposition of nickel thin films by high power impulse magnetron sputtering, **Beilstein Journal of Nanotechnology 10**, 2019, 1914–1921.

II: M. Kateb & S. Ingvarsson, Microscopic origin of uniaxial magnetic anisotropy induced by *in-situ* magnetic field during the growth, **Manuscript** (5 pp).

III: M. Kateb et al., Tuning atomic order and magnetic anisotropy of single crystal $Ni_{80}Fe_{20}$, **Manuscript** (8 pp).

IV: M. Kateb et al., Tailoring interface mixing and magnetic properties of Permalloy/Pt multilayers, **International Workshop on Thin Films for Electronics, Electro-Optics, Energy, and Sensors** 2019.

V: M. Kateb et al., Effect of substrate bias on microstructure of epitaxial film grown by HiPIMS: An atomistic simulation, **Manuscript** (7 pp).

Abbreviations and symbols

a & b	Proportionality constants in anomalous Hall effect
AFM	Atomic force microscopy
AMR	Anisotropic magnetoresistance
α_i	The cosine of the angle between saturated magnetization and crystal axis i
β_i	The cosine of the angle between applied magnetic field and crystal axis i
C_i	Concentration of i element
c	Elastic modulus
D	Magnetic domain width
d	Film thickness
Δ	The angular difference between X-ray reflectivity fringes that corresponds to the capping and/or buffer layer
δ	The angular difference between X-ray reflectivity fringes that corresponds to the film thickness
dcMS	Direct current magnetron sputtering
E_{tot}	Total energy of a ferromagnetic system
E_{an}	Magnetic anisotropy energy
E_{ca}	Magnetocrystalline anisotropy energy
E_{ex}	Magnetic exchange energy
E_{λ}	Magnetoelastic energy
E_{st}	Magnetostatic energy
E_{Zeeman}	Zeeman energy
f	A function of resistance ratio used in order to solve van der Pauw equation
fcc	Face-centered cubic crystal structure
FMR	Ferromagnetic resonance

FWHM	Full width half maximum of an XRD peak
H	Magnetic field
H_c	Magnetic coercivity
H_k	Magnetic anisotropy field
HiPIMS	High power impulse magnetron sputtering
K_0, K_1 & K_2	Magnetocrystalline anisotropic constants of cubic system
k_B	Boltzmann constant
K_{u1} & K_{u2}	Uniaxial anisotropy constants
$L1_0$	An fcc crystal of 1:1 alloy those stacked layer by layer along the <100> orientation
$L1_2$	An fcc crystal with one element sitting on the corners and another one sitting on the faces that reproduce 1:3 composition
Λ	The angular difference between X-ray diffraction multilayer peak that corresponds to multilayer period thickness
λ	The magnetostiction coefficient
$\lambda_{\langle vdw \rangle}$	The magnetostiction coefficient in $\langle vdw \rangle$ crystal orientation
M	Magnetization
M_{sat}	Saturated magnetization
$M-H$	Magnetization vs. field
MOKE	Magneto-optical Kerr effect
N_d	Demagnetization factor
Py	Permalloy containing $Ni_{80}Fe_{20}$ at. % or $Ni_{81}Fe_{29}$ wt. %
ρ	Electrical resistivity (scaler or a tensor)
ρ_0	Electrical resistivity at zero magnetic field
ρ_1 & ρ_2	Principle resistivity axes in the film plane
ρ_{ave}	Average resistivity utilized in anisotropic magnetoresistance measurements
ρ_{ii}	A diagonal element of resistivity matrix
ρ_{ij}	An off-diagonal element of resistivity matrix
ρ_{iso}	Electrical resistivity of isotropic specimen
$\rho_{\parallel}$	Resistivity obtained by applied saturating magnetic field parallel to the current direction

$\rho_\perp$	Resistivity obtained by applied saturating magnetic field perpendicular to the current direction
R	Electrical resistance
r	Spatial coordination
σ	Mechanical stress
T	Absolute temperature
TEM	Transmission electron microscope
θ	Angle between easy magnetization axis and saturated magnetization direction
$\theta - 2\theta$	Symmetric XRD scan i.e. equal incidence and detector angles with respect to the substrate normal
v	Volume fraction of ordered phase
Ω	Volume of specimen
γ_i	The cosine of the angle between applied stress and crystal axis i
Φ	Angle between current and saturated magnetization direction
ϕ	Angle between easy magnetization axis and saturated magnetization direction
ϕ & ψ	In-plane and out-of-plane polar angles of X-ray diffraction
XRD	X-ray diffraction
XRR	X-ray reflectivity
z	Atomistic coordination number or number of first nearest neighbors

Acknowledgments

I know this acknowledgment is nothing compared to the infinite supports I received from everybody in VR-III. First of all, I would like to thank my supervisor Snorri Þorgeir Ingvarsson for his endless help and patience. This Ph.D. could not be done without his guidance and encouragement. I will not forget his favors since my arrival to Iceland and owe him forever. I would like to also thank Jón Tómas Guðmundsson for giving me the opportunity to enjoy his support and guidance. Viðar Guðmundsson, Ari Ólafsson, Kristján Leósson, Sveinn Ólafsson and Einar Örn Sveinbjörnsson which I am indebted for their help.

I would also like to thank all the members of sputtering Lab and Grain Research. In particular I would like to thank my forever friends Tryggvi Kr. Tryggvason (Kibbi), Unnar Bjarni Arnalds and Einar Baldur Þorsteinsson. I appreciate the kindness and patience of all XRD users namely Muhammad Taha Sultan, Kristbjörg Anna Þórarinsdóttir, Ásgeir Tryggvason and Hákon Örn Árnason. I would like to thank Friðrik Magnus and Árni Sigurður Ingason for their useful suggestion and discussion. Kristján Jónsson and Marian Ivanov Siarov that without their help I could not complete my experimental setup.

Bing Cui Qi, Anna-Karin Eriksson, Rabia Yasmin Khosa, Margherita Zuppardo, Hamid Hajihoseini, Ragnar Dzosua Builong Jónsson, Davíð Ingvi Snorrason at office next door whom I wish to thank for the good time we shared together.

Completing this work could have been much more difficult without my Iranian friends Younes Abghoui, Aysan Safavi, Mahdi Maghsoudi, Saye Hanifpour, Ebrahim Tayyebi, Narges Atrak, Reza Tafrishi, Ali Kamali, Iman Mehrabinejad, Mostafa Ghasemi, Hamze Mohammadi, Saeed Manshari, Elham Niazi, Farhad Zare, Sara Sayyadi, Hadi Rezaei, Elham Fakhri, Hamed Geramizadeh, Arash Sheikhlar and also Javed Hussain and Arnar Sveinbjörnsson for joining us.

1 Introduction

1.1 Introduction

A physical property of a material is said to exhibit anisotropy when it is a function of direction. Whether a specimen magnetization arises from its atoms, orbitals or domains, the preference for a average magnetic moment to lie in a particular direction in a specimen is called *magnetic anisotropy*. It is exploited in the design of most magnetic materials and spintronic devices of commercial importance. For instance, various magnetic recording devices have been built based on reversing magnetization direction using a current signal passing through a coil as a recording head. Regardless of the hard or soft characteristic of the utilized ferromagnet, the writing process is essentially switching between two directions with the minimum anisotropic energy. This concept stands true for the state of the art high density (1 Tb/in^2) heat-assisted magnetic recording, that utilizes laser heating for softening of a hard magnetic film (Rottmayer et al., 2006), and future low power consumption and ultrafast alternative based on femtosecond laser pulse switching (Beaurepaire et al., 1996; Kirilyuk et al., 2010). Another example is a magnetic field sensor which must present linear variation of resistivity with the strength of external magnetic field. This can be achieved using planar Hall effect or anisotropic magnetoresistance effect. In both cases, it is necessary that the magnetic axis with the maximum anisotropic energy to be aligned with the external magnetic field. In such a condition the magnetization inside the ferromagnet rotates gradually with the strength of the external field. This changes resistivity due to above mentioned effects and e.g. can be detected by a voltage change at a constant current. These examples clearly show the practical importance of magnetic anisotropy.

1.2 Thesis outline

The aim of this thesis is to develop an understanding of the key features defining magnetic anisotropy of various films; namely, polycrystalline, single crystal and superlattice with particular focus on the permalloy $Ni_{80}Fe_{20}$, with subscript being atomic %, (which we refer to as Py). There are several reasons for the choice of Py. The most important one is that several explanations were proposed for magnetic anisotropy observed in Py but none of them seems to explain all instances of anisotropy in Py (Kateb et al., 2019a). In particular, induced uniaxial anisotropy due to the tilt deposition with respect to substrate normal has not been systematically studied in Py (Kateb et al., 2019a,d). Besides, Py is known as a ferromagnet with nearly zero magnetostriction, low magnetocrystalline anisotropy constant, low anisotropy field and coercivity (Yin et al., 2006).

These properties, will be introduced in the next chapter, indicate Py is a unique candidate to study *induced uniaxial anisotropy* by different preparation methods which is the main objective of this thesis. As microstructure changes, e.g. from polycrystalline to single crystal, we expect some of the properties to appear, magnetocrystalline anisotropy in this example. During the thesis, we are adding a few effects one by one and try to understand which one has a major effect on the definition of magnetic anisotropy. In this sense, our results lead to a comprehensive understanding of the magnetic anisotropy in Py rather than individual effects.

The background required to understand the discussions will be described in the next chapter including various energy terms in a ferromagnet and definition of magnetic anisotropy and its different types. The effect of other energy terms and magnetic anisotropy has been also reviewed. Then we focus more on previous theories for the occurrence of uniaxial anisotropy in Py and their physical basis. The 3rd chapter is devoted to our thin film preparation and measurement methods. We begin to explain high power impulse magnetron sputtering (HiPIMS) deposition, developed in the last two decades, and its difference with the more conventional dc magnetron sputtering. Apparently the former is not well introduced to or sometimes misunderstood by the magnetism community. We discuss several advantages of HiPIMS method for the preparation of magnetic thin films. With regard to the measurement, the basis of anisotropic magnetoresistance and van der Pauw resistivity measurement is explained. There we point out theoretical efforts in order to extend the latter method for an anisotropic medium. We also demonstrate our contribution to determining anisotropic magnetoresistance of ferromagnetic films utilizing extended van der Pauw method at the end of the 3rd chapter.

Although we point out some of our achievements in the 3rd chapter, e.g. where we developed a method for anisotropic magnetoresistance measurement, the results of measurement are presented in chapter 4. We show the mechanism that has been though to be responsible for uniaxial anisotropy induced by tilt deposition is not valid. The only theory that explains both of the biaxial and uniaxial magnetic anisotropy occurrences is the arrangement of Ni and Fe, the so-called *atomic order*. In multilayer films, it is essential to account for the effect of strain which is maximized when there is a sharp interface between layers.

2 Phenomenology of magnetic anisotropy

The purpose of this chapter is to familiarize the reader with the physical basis required to understand the discussions in the following chapters. We will begin with different energy terms in a ferromagnet and define them one by one specially their relation with magnetic anisotropy. The magnetic anisotropy and its different types will be introduced in a more detailed manner. Especial attention has been brought to previous theories explaining the mechanism of uniaxial anisotropy in Py and whenever needed their required background is also explained.

2.1 Energy terms

Ferromagnetic materials can possess a relatively large spontaneous magnetization in the absence of an applied field below the Curie temperature. The total free energy of a ferromagnetic system in thermodynamic equilibrium is given by (Hubert and Schäfer, 2008):

$$E_{\text{tot}} = E_{\text{an}} + E_{\text{ex}} + E_{\lambda} + E_{\text{st}} + E_{\text{Zeeman}} \tag{2.1}$$

where the individual components correspond to the anisotropy, exchange, magnetoelastic, magnetostatic and Zeeman energy, respectively.

Eq. (2.1) indicates the importance of *magnetic anisotropy* which strongly affects the magnetic behavior of ferromagnetic materials. The term magnetic anisotropy means magnetic properties depend on the direction in which they are measured (Cullity and Graham, 1972, p. 197). The measure for anisotropic energy is the energy required for saturation of magnetization in a specific direction of the specimen. Magnetic anisotropy causes the magnetization loops ($M-H$) measured in different directions to vary as schematically shown in figure 2.1. The figure indicates an ideal uniaxial anisotropy, which will be introduced properly in this chapter, with sharp switching parallel to the magnetization direction and linear response perpendicular to that. This general behavior is of considerable scientific interest and practical importance. In particular designing spintronic devices such as magnetic memories and sensors require very well-defined magnetic anisotropy and knowing the exact behavior in each direction.

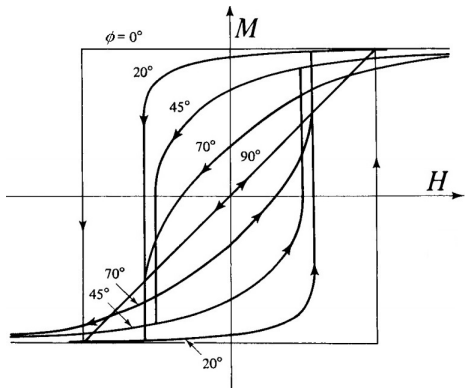

Figure 2.1. Schematic illustration of $M-H$ loops along different directions (Cullity and Graham, 1972, p. 317).

There are several kinds anisotropy: shape, magnetocrystalline, induced, exchange and stress anisotropy (Cullity and Graham, 1972, p. 197). Among these only magnetocrystalline anisotropy is intrinsic to the material. The term *induced* is limited to techniques applied during material preparation such as annealing in a magnetic field.

2.2 Zeeman energy

Zeeman energy is the energy of a magnetic body in an external field H which is given by

$$E_{\text{Zeeman}} = -\mu_0 \int_{\Omega} H \cdot M(r) d^3 r \tag{2.2}$$

where μ_0 is the vacuum permeability, $M(r)$ is the local magnetization vector and $d^3 r$ is an element of volume Ω. Eq (2.2) states the Zeeman energy is minimized when internal magnetization is aligned parallel to the external field.

2.3 Shape anisotropy

A uniformly magnetized body of magnetic material, as shown in figure 2.2(a), will exhibit a self energy due to the sum of the long range dipole-dipole interactions within the sample, this is called the magnetostatic energy (E_{st}). At the surface, the discontinuity in magnetization results in a stray field which can be thought of as originating from a collection of free poles or magnetic charges. Thus, the magnetization at discontinuities, within a magnetic material, are the source of the stray field outside specimen. The demagnetizing field developed inside the specimen acts to oppose the stray field. It is important to note that the magnetic dipole-dipole interaction is very much smaller than the strong exchange interaction which is very short range. However, Landau and Lifshitz showed that the magnetic dipole-dipole interaction is long range and so this

interaction is important for magnetic moments that are separated by large distances (Bogart, 2010). The magnetostatic energy can be reduced by almost a factor of 2 if the crystal splits into two domains magnetized in opposite directions as in figure 2.2(b), because this brings north and south poles closer to one another, thus decreasing the spatial extent of the stray field. If the crystal splits into four domains as in figure 2.2(c), the magnetostatic energy again decreases, to about one-fourth of its original value, and so on. But this division into smaller and smaller domains cannot continue indefinitely, because each wall formed in the crystal has a wall energy per unit area, which adds energy to the system. Eventually an equilibrium domain size will be reached.

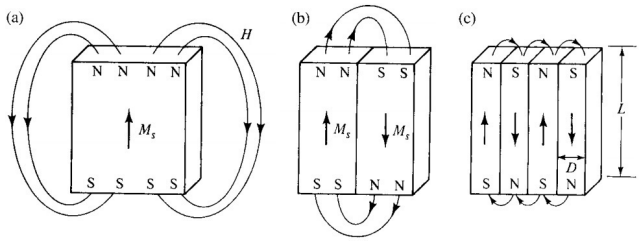

Figure 2.2. Division of a crystal into domains will reduce magnetostatic energy (Cullity and Graham, 1972, p. 293).

The magnetostatic energy associated with the demagnetizing field is given by (Cullity and Graham, 1972, p. 235)

$$E_{\mathrm{st}} = -\frac{1}{2}\mu_0 \int_{\Omega} H_{\mathrm{d}} M(r) d^3 r \tag{2.3}$$

where H_{d} is the demagnetizing field. The accurate distribution of H_{d} in space is barely known and its evaluation is very difficult. Thus, it is common to simplify Eq. (2.3) using $H_{\mathrm{d}} = -N_{\mathrm{d}} M$ as

$$E_{\mathrm{st}} = \frac{1}{2}\mu_0 N_{\mathrm{d}} M^2 \tag{2.4}$$

where N_{d} is the demagnetizing factor and M is the sum of magnetization vectors (M_{s}) in all domains. The value of N_{d} for a sphere or a cube, in a direction parallel to an edge, is 1/3 (SI). Now we can calculate the magnetostatic energy of a single-domain crystal:

$$E_{\mathrm{st}} = \frac{1}{2}\mu_0 N_{\mathrm{d}} M_{\mathrm{s}}^2 \tag{2.5}$$

Although division of crystal decreases E_{st} it also increase the energy by introduction of domain walls and thus it ends up with an equilibrium number of domains. The magnetostatic energy of the multi-domain crystal of figure 2.2(c) is the sum of the magnetostatic and wall energies (Chikazumi, 1997, p. 440):

$$E_{\mathrm{st}} = 0.85\mu_0 M_{\mathrm{s}}^2 D + E_{\mathrm{dw}} \frac{L}{D} \tag{2.6}$$

where D is the thickness of the slab-like domains assuming it is small compared to film thickness L and E_{dw} is the domain wall energy per unit area.

2.4 Magnetocrystalline anisotropy

Generally, the magnetic anisotropy energy term which possesses the crystal symmetry of the material is called magnetocrystalline anisotropy. The magnetocrystalline anisotropy energy acts in such a way that the magnetization tends to be directed along certain definite crystallographic axes, which are termed directions of easy magnetization axis or plane. Conversely, the directions along which it is most difficult to align the magnetization in the crystal are called hard axes. It has been found experimentally that the energy to magnetize a ferromagnetic crystal up to saturation along a hard axis is often considerably higher than the energy required to magnetize the same ferromagnetic crystal to saturation along an easy axis. When an applied field rotates magnetization away from crystal easy direction, there will be energy stored in the crystal which is called *magnetocrystalline anisotropy energy* (E_{ca}).

2.4.1 Physical origin of magnetocrystalline anisotropy

Magnetocrystalline anisotropy is due mainly to *spin-orbit coupling* (interaction). The spin-spin coupling generate exchange energy which is isotropic as stated by Eq. (2.10) independent of the crystal axes. Thus, the resistance of spin against reorientation by an external field is due to its coupling to the orbit in which the latter strongly coupled to the lattice (figure 2.3). It is worth mentioning that it is not possible to determine anisotropic constants from first principal calculation.

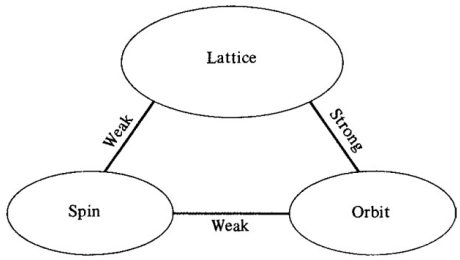

Figure 2.3. Schematic illustration of spin–orbit–lattice interaction (Cullity and Graham, 1972, p. 205)

2.4.2 Cubic anisotropy

Magnetization curves measured at room temperature along each of the principal crystallographic axes of iron and nickel are shown in figure 2.4. Iron and nickel are arranged in a body-centered cubic (bcc) structure and face-centered cubic (fcc) structure, respectively. For iron, as shown in figure 2.4(a), $M-H$ loop measurements show that saturation can be achieved with low fields along the $\langle 100 \rangle$ orientation which is its easy axis. On the other hand, an order of magnitude higher fields are needed to saturate iron in the $\langle 110 \rangle$ orientation. In nickel, figure 2.4(b) shows that the $\langle 111 \rangle$ orientation is the easy magnetization axis.

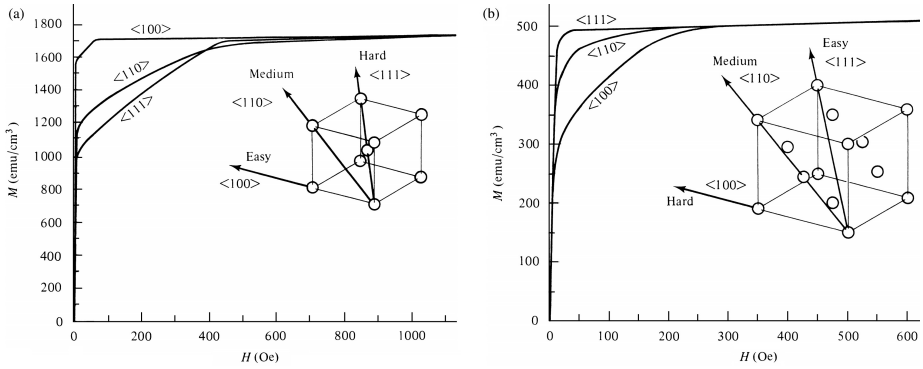

Figure 2.4. Magnetization curves for (a) bcc iron and (b) fcc Ni crystals along selected crystal orientation (Cullity and Graham, 1972, p. 199).

Figure 2.5 schematically shows the behavior of a simple four-domained disk when external field (H) is applied along on of its easy axes. The easy magnetization direction is the direction of spontaneous domain magnetization in the demagnetized state as shown in figure 2.5(a). Thus an increase in magnetization can be easily achieved by domain wall motion without rotation.

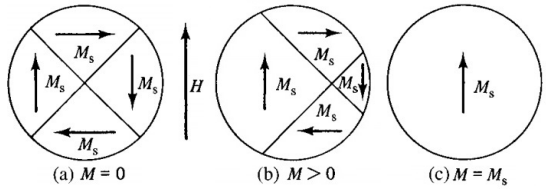

Figure 2.5. Variation of domain structures in a single-crystal disk with H applied in the easy direction. (Cullity and Graham, 1972, p. 200).

Figure 2.6 shows the domains variation with the applied field along the hard axis. In this direction, there might be some domain wall motion but at the end it requires rotation of domains out of the easy direction which requires higher fields. It is worth mentioning that it is not domain that rotates but the net magnetic moment of domain which rotates.

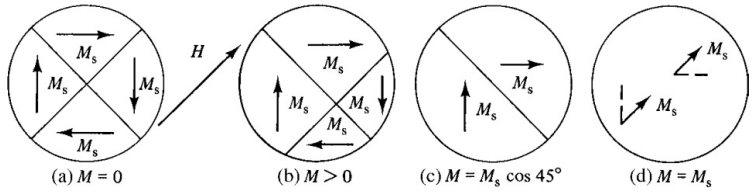

Figure 2.6. Variation of domain structures in a single-crystal disk with H applied in the hard direction. (Cullity and Graham, 1972, p. 201).

E_{ca} is usually expressed in terms of a series of direction cosines of M_{sat} relative to the crystal axes which means projection of M_{sat} in different axes (M_i/M_{sat}).

$$E_{ca} = K_0 + K_1(\alpha_1^2\alpha_2^2 + \alpha_2^2\alpha_3^2 + \alpha_3^2\alpha_1^2) + K_2\alpha_1^2\alpha_2^2\alpha_3^2 + ... \tag{2.7}$$

where K_0,K_1,K_2,... are anisotropic constants specific for a material and α_is are the cosines of angles between M_{sat} and crystal axes.

Since K_0 is independent of angle it is usually ignored and K_2 can be neglected if it become considerably smaller than K_1. Thus, the direction of easy axis is determined by the sign of K_1.

Figure 2.7 schematically illustrates the E_{ca} for Fe and Ni. For iron K_1 and K_2 are 48×10^3 and $\pm5\times10^3$ J/m^3, respectively, at room temperature. Thus, when K_1 is positive then $E_{100} < E_{110} < E_{111}$ and the $\langle 100\rangle$ orientation becomes the easy axis. In the case of Ni K_1 and K_2 are -4.5$\times10^3$ and 2.34$\times10^3$ J/m^3, respectively, and $E_{111} < E_{110} < E_{100}$. Thus E_{ca} is minimum along the the $\langle 111\rangle$ orientation which makes it the easy axis.

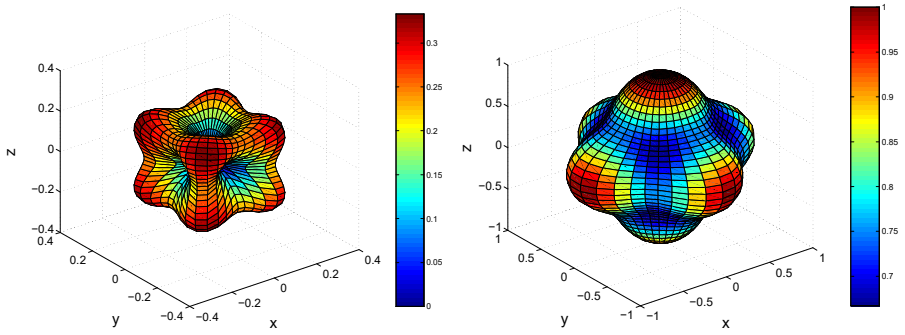

Figure 2.7. Polar plots of magnetocrystalline anisotropy (E_{ca}) for the cubic anisotropy cases (left) $K_1 > 0$ and (right) $K_1 < 0$ with their minimum along the [100] and [111], respectively (d'Aquino, 2004)

In a single crystal film, shape anisotropy forces magnetization axes into the film plane and Eq. (2.7) takes the following simple form:

$$E_{ca} = \frac{1}{4}K_1 \sin^2 2\phi \tag{2.8}$$

here ϕ refers to the angle between the easy axis and M_{sat}.

2.4.3 Uniaxial anisotropy

For uniaxial crystals, such as cobalt, the magnetocrystalline anisotropy energy is given by:

$$E_{ua} = K_{u1}\sin^2\phi + K_{u2}\sin^4\phi + ... \tag{2.9}$$

here K_{u1} and K_{u2} are uniaxial anisotropy constants.

Figure 2.8 schematically shows E_{ua} for a material with easy axis and easy plane with positive and negative K_{u1}, respectively. For Co $K_{u1} = 4.1\times10^5$ J/m^3 and $K_{u2} = 1.0\times10^5$ J/m^3 at room temperature.

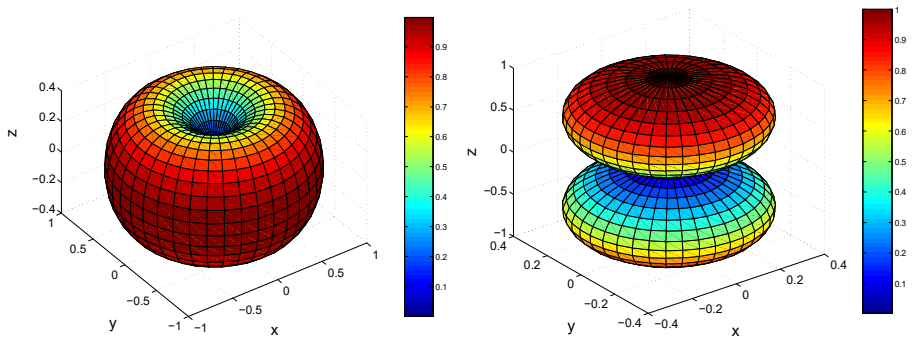

Figure 2.8. Uniaxial anisotropy with (left) easy axis $K_{u1} > 0$ and (right) easy plane $K_{u1} < 0$ (d'Aquino, 2004)

2.4.4 Permalloy

The magnetocrystalline anisotropy constants of alloy systems can vary markedly with chemical composition. For binary nickel-iron alloys, which are of particular relevance here, the magnetocrystalline anisotropy depends sensitively upon the percentage nickel content as shown by Bozorth (1956). The magnetocrystalline anisotropy constant, K_1, is seen to pass through zero for nickel compositions between 75 and 80%. For Py, containing 80% Ni, K_1 is very small and slightly negative, which indicates that the easy axes of magnetization corresponds to the [111] set of directions.

2.4.5 Polycrystalline permalloy

Whilst magnetocrystalline anisotropy plays an important part in the behavior of nearly all ferromagnetic materials, its effects only appear in simple form in single-crystal specimens. For polycrystalline samples with a truly random orientation of crystallite grains the magnetocrystalline anisotropy will average out and the sample will exhibit no net magnetocrystalline anisotropy, although the local magnetization distribution will be influenced by the local magnetocrystalline anisotropy. A truly random distribution of crystallite orientation is, however, very rare and the majority of polycrystalline samples have a preferred orientation, or texture, which can be enhanced by the preparation technique. In this case, the strength of the magnetocrystalline anisotropy depends upon the degree of preferred orientation within the sample.

2.5 Induced Magnetic Anisotropy

Py is a unique candidate to study *induced uniaxial anisotropy* due to its vanishingly small magnetostriction, low magnetocrystalline anisotropy, anisotropy field and coercivity (Yin et al., 2006). The proposed explanations for uniaxial anisotropy include oriented defects and oxides, (Sugita et al., 1967; Fujiwara and Sugita, 1968) directional ordering of Fe/Ni atoms pairs (Chikazumi, 1950), shape anisotropy of an elongated ordered phase

(Kaya, 1953), composition variation between grains (Kench and Schuldt, 1970) and more recently, localized composition non-uniformity (Rodrigues et al., 2018). These can be manipulated during preparation of Py and current experimental techniques facilitates study of each explanation.

2.5.1 Post annealing

A conventional way of inducing uniaxial anisotropy is by post annealing or *in-situ* deposition in an external magnetic field. Bozorth et al. (1934) believed that applying an external magnetic field causes magnetostrictive deformation which during annealing in a field becomes permanent. The uniaxial anisotropy induced by *in-situ* magnetic field during the growth can also be explained by the same interpretation. Figure 2.9 schematically shows the concept of magnetostriction. The upper row of atoms depict the demagnetized state without preferred orientation (weak magnetocrystalline anisotropy) but some net magnetic moment. Applying a saturating field will align spin parallel to the field as shown in the bottom row. As result the value of magnetostriction coefficient (λ) equals to $\Delta L/L$

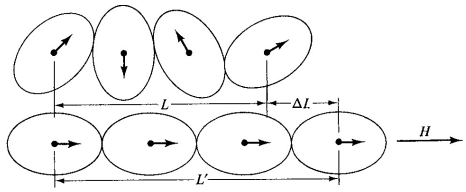

Figure 2.9. Schematic illustration of a material with positive magnetostriction (Cullity and Graham, 1972, p. 257).

The strain depicted in figure 2.9 is huge. Magnetstrictive strain is usually very small and on order of 10^{-5}. This is a direct consequence of spin–orbit coupling i.e. orbit magnetic moment is almost entirely quenched and does not reorient with the applied field. However, at elevated temperatures or during deposition, when the lattice has more degree of freedom, it is possible to align magnetic moments.

It has been shown that both post annealing (Chikazumi, 1956) and growth (Chikazumi, 1961) in the external magnetic field show orientation dependency for the single crystal Py. For instance, annealing and applying *in-situ* magnetic field both result uniaxial anisotropy if the magnetic field is applied along the crystal easy axes i.e. [111] directions. While a magnetic field along the [100] directions, crystal hard axes, is only able to slightly rotate easy axis out of [111] directions. In an effort to understand such a complication, it turned out Py has a negligible magnetostrction i.e. its elastic energy is two order of magnitude smaller than anisotropic energy (Chikazumi, 1964). Thus other effects such as the crystalline anisotropy can easily overcome magnetostriction.

2.5.2 Tilt deposition

Control over magnetization direction can be achieved by depositing under an angle with respect to the substrate normal (Smith, 1959). As shown in figure 2.10, this gives a hard axis and easy axes parallel and perpendicular to the incident plane, respectively. It has been thought that tilt deposition causes self-shadowing which gives some sort of in-plane texture perpendicular to incident plane. Self-shadowing is very well known phenomena in the thin-film community which allows growth of textured films, porous membranes and variety of nanowire arrays (Mahieu et al., 2006). Figure 2.11 schematically shows the onset of the growth and resulting nanowires due to self-shadowing. An in-plane texture due to self-shadowing has not been proved so far even with the current advanced microscopy techniques. Later, it has been shown that self-shadowing causes off-normal texture in the films (Sun et al., 2007; Solovev et al., 2017). This encourages perpendicular (out-of-plane) anisotropy in the film and thus lowers in-plane anisotropy or even leads to in-plane isotropy, i.e. a complete loss of in-plane anisotropy (Phuoc et al., 2013).

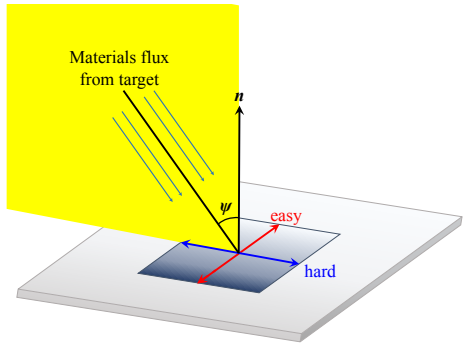

Figure 2.10. Uniaxial anisotropy and direction of magnetic axes determined by the tilt geometry.

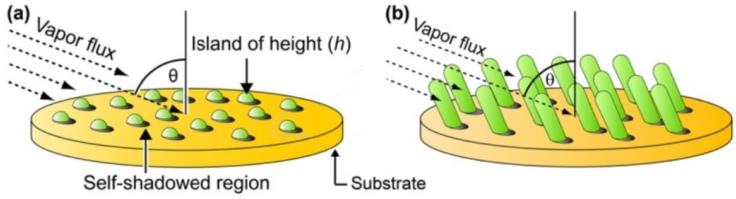

Figure 2.11. Schematic illustration of self-shadowing (Kwon et al., 2015).

2.5.3 Ion irradiation

In a similar way to post-annealing bombardment of specimen with high energy ions can cause rearrangement of atoms in presence of a magnetic field (Woods et al., 2002). It has also been shown that neutron irradiation with or without external magnetic field

will increase the H_c of Py (Schindler and Salkovitz, 1960). This can be explained by directional ordering due to the vacancy assisted diffusion at room temperature. However, after irradiation in the presence of external magnetic field the $M-H$ loop became more square while without magnetic field it was more rounded.

Previously irradiation has been considered as destructive technique (radiation damage) that results in inferior microstructure. However, current state of the art facilities enable control over the process. Néel et al. (1964) have already shown that combination of irradiation and high temperature in presence of an external magnetic field results a long range order ($L1_0$ superlattice for $Ni_{50}Fe_{50}$ system). They obtained a strong uniaxial anisotropy due to that the majority of the volume fraction being ordered in such way that gave an easy axis parallel to the applied field. Recently, irradiation without magnetic field has been utilized for modification of interface in Py/Pt system (Ganguly et al., 2015).

2.5.4 Plastic deformation

An uniaxial anisotropy can be induced in certain alloys simply by plastic deformation at room temperature (cold working). Unlike magnetoelastic effect, that will be discussed in section 2.7, understanding plastic deformation is difficult. The magnitude of K_{u1} (2×10^6 J/m^3) after cold working becomes larger than K_1 for the Ni and Ni-rich NiFe alloys. Depending on the crystal orientation, it can produce an easy axis parallel or perpendicular to the elongated direction depending on the positive or negative K_{u1}, respectively. In a single crystal Py, easy axis becomes parallel to elongated direction while it is associated with introduction of defects and stress. Figure 2.12 shows the result of rolling for polycrystalline NiFe alloy including Py (80% Ni). Polycrystalline Py with [100] preferred orientation (texture) by recrystallization of heavily cold rolled specimen. In this case, the resulting easy axis would have a high angle with respect to the elongated direction and thus, K_{u1} must be negative. In polycrystalline materials, with randomly oriented grains, plastic deformation generates an easy axis parallel to the elongated direction.

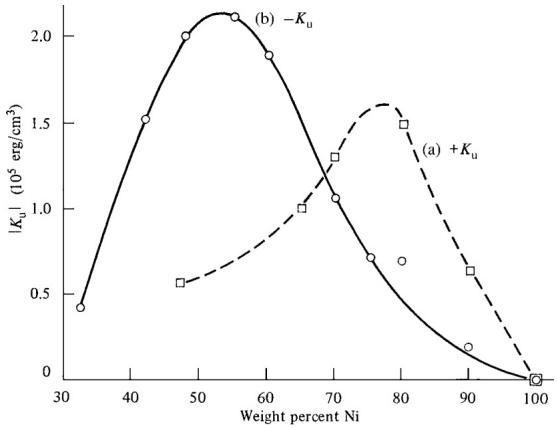

Figure 2.12. Uniaxial anisotropy constant K_{u1} of rolled polycrystalline NiFe alloys. (a) Randomly oriented grains rolled to 33% reduction in thickness. (b) [100]-textured material rolled to 55% reduction (Cullity and Graham, 1972, p. 350).

The origin or uniaxial anisotropy induced by plastic deformation has been explained by Chikazumi (1997) using pair ordering theorem. It is based on slipping (111) planes rather than diffusion. However it cannot explain the direction of the resulting easy axis (Cullity and Graham, 1972, p. 352). It is also not clear why the two curves in figure 2.12 peak at different composition. While pair ordering predicts a maximum at 75% Ni (corresponding to Ni_3Fe). The magnitude of K_{u1} after rolling is some 50 times larger than after annealing in an external magnetic field, which shows that slip can produce a far larger concentration of like-atom pairs.

2.6 Exchange anisotropy

The exchange energy is written as:

$$E_{ex} = A \sum_{i=1}^{3} \nabla \alpha_i(r)^2 \tag{2.10}$$

Where A is the exchange stiffness parameter, and α_i is the direction cosine of the spin at lattice point r with respect to i axis. This equation relates the exchange energy density to the magnitude of the angle between adjacent spins. As mentioned earlier, the exchange energy is very short range and is essentially a nearest neighbor interaction. Eq. (2.10) shows that as the angle between two adjacent spins increases, the associated energy also increases.

2.7 Stress anisotropy

Although the magnetostrictive strain is small in most magnetic materials, the existence of magnetostriction means that an applied mechanical stress can alter the domain structure and create a new source of magnetic anisotropy. Figure 2.13 shows the marked effects of applied stress on the magnetization behavior of polycrystalline nickel (Cullity and Graham, 1972).

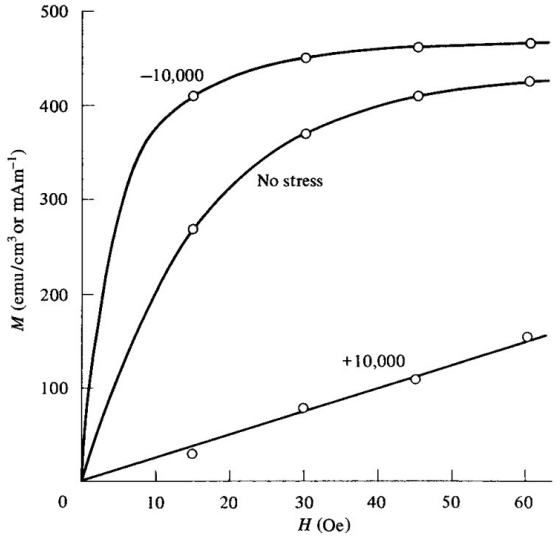

Figure 2.13. Effect of 10000 lb/in^2 (69 MPa) tensile (+) and compressive (−) stress on the $M-H$ behavior of Polycrystalline nickel (Cullity and Graham, 1972, p. 259).

The above mentioned example, shows the effect of stress for the case of negative magnetostriction. In a similar way, materials with positive magnetostriction present increase in magnetization with tensile stress. For Py, with nearly zero magnetostriction, the effect of stress is expected to be negligible (Buckley and McKeehan, 1925). However, it has been shown that Py present giant magnetostriction in ultrathin film form (Song et al., 1994; Kim and Silva, 1996; Choe, 1999). Thus it plays an important role in the Py multilayers which will be described in the chapter 4.

There is a close connection between the magnetostriction of a given material and its magnetic behavior under stress. As a result, the effect of stress on magnetization is sometimes called the *inverse magnetostriction*, but more common term is magnetoelastic effect. The Le Chatelier's principle states if, e.g. a material has positive magnetostriction coefficient (λ), it will elongate when magnetized; applied tensile stress, which tends to elongate it, will therefore increase the magnetization, and applied compressive stress will decrease it. The energy associated with applying a stress into a single crystal can be expressed as (Cullity and Graham, 1972):

$$E_\lambda = -\frac{3}{2}\lambda_{\langle 100\rangle}\sigma(\alpha_1^2\alpha_2^2+\alpha_2^2\alpha_3^2+\alpha_3^2\alpha_1^2)-3\lambda_{\langle 111\rangle}\sigma(\alpha_1\alpha_2\gamma_1\gamma_2+\alpha_2\alpha_3\gamma_2\gamma_2+\alpha_1\alpha_3\gamma_1\gamma_3) \tag{2.11}$$

where the subscript of λ denotes the crystal orientation and the γ_i is the direction cosines of the applied stress σ with respect to the crystal axes. It is worth mentioning that σ here is the elastic stress, where the material is deformed impermanently and can return to its original shape as soon as stress is removed.

In a polycrystal, where magnetostriction can be justified as isotropic, Eq. (2.11) reduce to the simple form of

$$E_\lambda = -\frac{3}{2}\lambda\sigma\cos^2\phi \tag{2.12}$$

The terms of Eq. (2.11) will add to the terms of Eq. (2.7) and in a materials with weak magnetocrystalline anisotropy, which is the case for Py, magnetic anisotropy can be controlled by applied stress.

Figure 2.14 illustrates the variation of a small sample consisting of four domains under applied stress schematically. The application of small tensile stresses to the demagnetized sample, figure 2.14(a), moves domain walls in such a way that decrease the volume of domains that are misaligned with the applied stress. These domains are completely eliminated by some higher value of the stress, as in figure 2.14(c), and E_λ is now at minimum. The domain structure is now identical with that of a uniaxial crystal. Thus, applying a small field along the current easy axis is able to saturate the specimen.

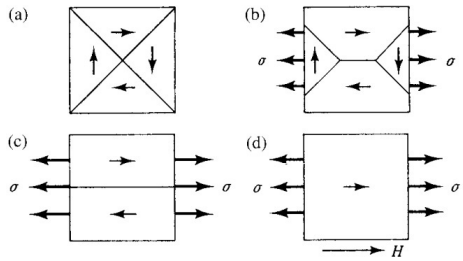

Figure 2.14. Schematic illustration of a material with positive magnetostriction under tensile stress.

2.8 The origin of induced uniaxial anisotropy in permalloy

2.8.1 Magnetostriction

Assuming that uniaxial anisotropy is the product of magnetostriction, rotation of magnetization out of original direction will increase the elastic energy by:

$$E_\lambda = -\frac{1}{2}(\frac{3}{2}\lambda)^2 c\cos^2\phi \tag{2.13}$$

where c is the elastic modulus, and ϕ the angle between domain magnetization and its original direction. Although Eq. (2.13) can give qualitatively correct angle dependence

of uniaxial anisotropy, the numerical value for Py gives $\frac{9}{8}\lambda^2 c = 1.6$ J/m^3 which is two orders of magnitude smaller than experimentally observed anisotropic energy of 1.4×10^2 J/m^3. This indicates that magnetostriction cannot explain the uniaxial anisotropy observed in Py.

2.8.2 Pair ordering

Later theories were based on the pair ordering (Chikazumi, 1950; Kaya, 1953) motivated by discovery of $L1_2$ superlattice (Ni_3Fe) (Dahl, 1936). Later Kaya (1938) studied wide range Ni-Fe alloy and their magnetic properties regarding to Ni_3Fe superlattice. He showed Ni_3Fe superlattice coexists with Ni or Fe-rich phases far from superlattice structure in a wide range of composition. Figure 2.15 shows the Ni_3Fe superlattice is stable within a wider range of composition and temperature compared to the FeNi ($L1_0$) and Fe_3Ni ($L1_2$). In the following Ni_3Fe superlattice will be referred to as ordered and any other fcc lattice who's arrangement deviates from this structure will be called disordered.

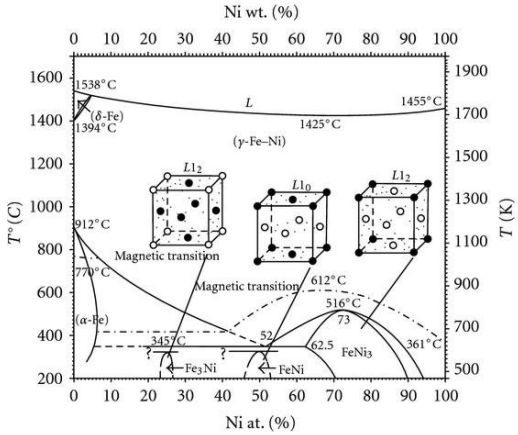

Figure 2.15. The different superlattices that can be found in the Fe–Ni system (Vernyhora et al., 2012).

It is worth mentioning that in an ordered Ni_3Fe phase the entire pair bonds are Ni–Fe while in a disordered state Ni–Ni and Fe–Fe pairs can exist. Based on the fact that lattice parameter of a disordered Py, e.g. prepared by rapid cooling from high temperature, contracts with the progress of ordering during annealing without magnetic field, e.g. during annealing without magnetic field, Chikazumi (1950) assumed Ni–Fe bonds to be smaller than Ni–Ni and Fe–Fe ones. This contraction is on the order of 10^{-4} (3.5550 vs. 3.5556 Å that becomes $\sim 1.69 \times 10^{-4}$ (Lutts and Gielen, 1970)) i.e. 100 times larger than magnetostrictive deformation, thus it anisotropy energy must be larger than elastic energy by factor of 10^2 which is in agreement with the experimental value.

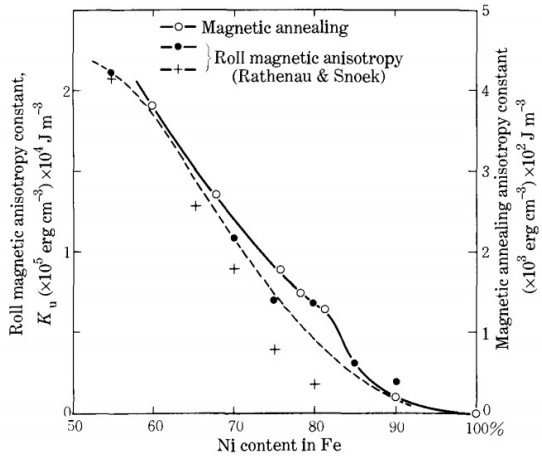

Figure 2.16. Variation of K_{u1} with the composition of Fe–Ni system (Chikazumi and Oomura, 1955).

2.8.3 Shape anisotropy of ordered phase

Another theory proposed by considering a texture of ordered phase by Kaya (1953) assuming that the long-ranged ordered phase might be locally perturbed. By putting change of magnetization (ΔM_s) during the ordering process to be 40 G and volumetric ratio (v) of 50% ordered texture, magnetostatic energy can be obtained by

$$E_{st} = -\frac{1}{2}\Delta N \Delta M_s^2 v(1-v)\cos^2\theta \tag{2.14}$$

where ΔN is the difference in demagnetization factors parallel and perpendicular to long axis and θ is the angle between magnetization and long axis of the particle. Eq. (2.14) gives a value of 1.2×10^2 J/m^3 which is in agreement with experimental value. However, the term $v(1-v)$ predicts a maximum at 0.5 fraction and predict the same energy e.g. for v equal to 0.3 and 0.7.

In order to verify one of these theories Chikazumi and Oomura (1955) studied composition dependency of K_{u1} obtained by cold rolling and and aneling (shown in figure 2.16). The results showed a monotonic change of K_{u1} while these theories predicted dependency to magnetostriction coefficient (Chikazumi, 1950), that changes sign between 75 – 80%, or a peak at 75% which Ni_3Fe formation is most effective (Kaya, 1953). They concluded that any directional order away from cubic symmetry results in uniaxial anisotropy in Py.

2.8.4 Corrected directional order

The term *directional order* was first defined by Chikazumi (1950) as a distribution of atom pairs. Later Slonczewski (1963) systematically described the directional ordering in particular low symmetry cases for the atom pairs. Considering a symmetry lower than cubic, Néel (1959) proposed corrected directional order assuming that the pseudo-dipole

interaction to be different for each pair e.g. Ni–Ni, Fe–Fe and Ni–Fe. He proposed the following relation for anisotropic energy

$$E_{\text{an}} = -\frac{N_{BB} l_0 l_0'}{k_{\text{B}} T}\left(k_1 \sum_{i=1}^{3} \alpha_i^2 \beta_i^2 + k_2 \sum_{i>j} \alpha_i \alpha_j \beta_i \beta_j\right) \tag{2.15}$$

where N_{BB} is number of e.g. Fe–Fe pairs, l_0 is the pseudo-dipole interaction coefficients which can be estimated from composition dependency of magnetostriction constants, l_0' is l_0 at specific temperature of T and k_{B} is the Boltzmann constant. β_i is the direction cosine of the applied field H with respect to the crystal axes (not to be confused with the magnetization direction reflected in α_i). The constants k_1 and k_2 are specific to the crystal structure which calculated for fcc crystal to be $\frac{1}{12}$ and $\frac{4}{12}$, respectively. Effect of concentration (C_{B}) can be considered in (2.15) as $N_{\text{BB}} = \frac{1}{2} z N C_{\text{B}}^2$ with N and z being total number of atoms in a unit volume and number of nearest neighbors in the lattice. Chikazumi (1956) showed the magnitude and direction of induced anisotropy depends on the crystal orientation i.e. it is most efficient along the $\langle 111 \rangle$, less so along the $\langle 110 \rangle$ and least along the $\langle 100 \rangle$ orientation. He compared (2.15) and (2.16) and calculated $k_1 : k_2$ ratio to be $1 : 8.5$ rather than theoretical $1 : 4$, a fact which has not been interpreted so far.

$$E_{\text{an}} = -K_{\text{u1}} \cos^2(\theta - \theta_0) \tag{2.16}$$

where θ_0 is the angle of easy magnetization axis.

The detailed calculation by Néel (1959) could model composition dependency of K_{u1} (cf. figure 2.16) but, strictly speaking, an order of magnitude higher than experimental value.

2.8.5 Atomic order

Chikazumi (1961) showed that orientation dependency is not limited to the post annealing in an external magnetic field but it is also valid using an *in-situ* magnetic field applied during the growth. However, we have recently showed that uniaxial anisotropy can be induced even in $\langle 100 \rangle$ orientation of the single crystal Py on the cost of reducing atomic order (Kateb et al., 2019a). We used tilt deposition with respect to the substrate normal which has been shown that its effect could be stronger than applying an *in-situ* magnetic field in definition of uniaxial anisotropy (Kateb and Ingvarsson, 2017). It is believed that the induced uniaxial anisotropy by the tilt deposition is associated with self-shadowing (Smith, 1959). In order to limit the self-shadowing, we rotated the substrate 360° back and forth with 100–300 ms stop time in between to capture the tilt effect. The polycrystalline films grown with this method presented state of the art surface roughness of 2 Å which indicate that self-shadowing does not exist but also showed very well-defined uniaxial anisotropy (Kateb et al., 2019d). Motivated by the later study we grow single crystal Py with its $\langle 100 \rangle$ orientation parallel to the sputter flux projection during the stop time. We detected cubic anisotropy in an ordered crystal grown by conventional dc magnetron sputtering (dcMS) which provides 1.5 Å/s deposition rate. Apparently, utilizing low deposition rate in growing single crystal is commonplace which encourage ordered single crystal. However, we were able to induce uniaxial anisotropy using increased instantaneous of deposition rate that suppressed adatom

mobility and resulted a disordered single crystal (Kateb et al., 2019a). To this end, we used HiPIMS method (Kateb et al., 2018) which provides low average deposition rate (Gudmundsson et al., 2012) but very high rate during the pulse ($\sim$50 Å/s) (Kateb et al., 2019a).

3 Preparation and measurements

In this chapter we explain thin film deposition and anisotropic magnetoresistance measurement. We briefly describe dc and high power impulse magnetron sputtering which have been utilized in preparation of our films. A special attention has been brought to the latter method and its advantage over former counterpart.

In the second part we describe anisotropic magnetoresistance and its measurement. Before explaining our method, a brief overview of various resistivity measurement is given with special focus on the van der Pauw method. Then we describe how theoretical methods can be utilized in order to extend the later method to anisotropic case. Finally, we demonstrate utilizing this method for anisotropic magnetoresistance which was suggested by experts in the field since 1975 but has not been realized so far. With the help of our method we seek to explain the origin of magnetic anisotropy which will be presented in the next chapter.

3.1 Thin film deposition

In practice, thin film deposition is used in almost every electronic and spintronic devices available today. However, it might sometime precede and/or followed by one or more pattering step(s) to achieve the desired geometry. The quality and properties of a thin film, among the other things, depends on the substrate surface as well as deposition method and conditions. For instance, in the following chapter we will show how deposition on Si/SiO_2 substrates leads to polycrystalline films while an MgO substrate allows growing single crystal film. Thin film deposition methods can be categorized to two classes of physical vapor deposition (PVD) and chemical vapor deposition (CVD). In the latter, it is necessary to provide condition for a chemical reaction on the substrate such as decomposition at elevated temperature. On the other hand, PVD methods are based on transferring target into substrate without chemical reaction e.g. by heating a substance. The only exception is the reactive sputtering where a compound based on target material and reactive gas (mostly nitrogen and oxygen) is deposited. The main purpose of this chapter is to introduce two main sputter deposition techniques used in this work and compare them regarding the preparation of magnetic thin films.

3.1.1 dcMS

Sputtering is referred to a process in which the target atoms, molecules and/or clusters are removed upon ion bombardment and transferred to a vapor as a flux. In direct current magnetron sputtering (dcMS), the ions are generated by igniting a plasma using

a negative dc voltage and the plasma is confined on the target surface using so called magnetron. As it works based on momentum transfer from ions to target atoms, it is easier to deposit refractory metals such as tungsten (W) using dcMS rather than evaporation methods. Regardless of the choice of substrate, parameters that control the film property in dcMS are the substrate temperature, vacuum level prior deposition, Ar pressure during process and applied power/voltage. The substrate temperature can be limited by dewetting of the film or its diffusion into the substrate. The vacuum level is a equipment specific and cannot be varied much. A low pressure does not allow ignition of plasma while very high pressures give a porous and low density film. Finally a low power cannot ignite the plasma and high powers are limited due to the thermal load that may result melting target and destroying equipment. Thus in dcMS one has to stay within allowed target temperature, pressure and power windows. This limits the electron density in dcMS to the $10^{15} - 10^{17}$ m^{-3} range (Seo and Chang, 2004; Sang-Hun Seo and Chang, 2006; Sigurjonsson and Gudmundsson, 2008) and ionization fraction of the sputter flux is below 10 % (Christou and Barber, 2000).

3.1.2 HiPIMS

High power impulse magnetron sputtering (HiPIMS) is an ionized PVD technique that has attracted much interest lately (Helmersson et al., 2006; Gudmundsson et al., 2012). By pulsing the target to a high power density with unipolar voltage pulses, low duty cycle, and low repetition frequency, high electron density is achieved in the plasma (Helmersson et al., 2006; Gudmundsson et al., 2012). This high electron density, peak electron density higher than 10^{19} m^{-3} in the vicinity of target (Gudmundsson et al., 2002; Bohlmark et al., 2005; Meier et al., 2018), leads to a high ionization fraction of the sputtered material (up to 70 % of target atoms (Kouznetsov et al., 1999)). As a result HiPIMS presents denser (Samuelsson et al., 2010; Magnus et al., 2011, 2012), void free (Alami et al., 2005) and smoother coatings (Alami et al., 2005; Magnus et al., 2011; Hajihoseini et al., 2018) compared to dcMS method.

The current and voltage waveform is an important characteristic feature of the HiPIMS process containing useful information on the pulse generator circuit and target materials as well as process condition such as working gas pressure. Figure 3.1 shows the current and voltage waveforms of the HiPIMS discharge recorded during room temperature growth of Py thin films at different working gas pressures. It can be seen that a nearly rectangular voltage pulse of 250 μs length was applied to the cathode target. Beside oscillations at the beginning and after ending the voltage pulse, there are local minima due to the initial current rise in all cases. The oscillations are due to an internal inductance of the power supply which creates a resonance circuit with the parasitic capacitance of cables and the capacitance of the cathode target. These are indications of the type of pulse generator circuit which is necessary to reproduce the result. The interested reader is referred to Hubička et al. (2020) for further information. Since the current onset occurs at different times for different pressure, the value of applied voltage (height in the blue curves) changes to maintain the required average power ($\sim$150 W here).

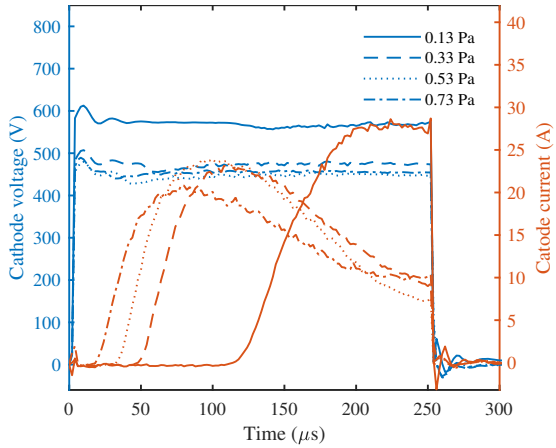

Figure 3.1. The discharge current-voltage waveform at different pressures, for a 75 mm diameter $Ni_{80}Fe_{20}$ target with Ar as working gas. The line style of the legend applies to both discharge voltage and current traces.

The current waveforms can be described by three distinct regions, as previously described by Lundin et al. (2009): (I) plasma initiation and a current maximum, followed by (II) a decay to a minimum and then (III) a steady state regime that remains as long as the discharge voltage level is maintained. The initial peak current is a result of strong gas compression due to the rapid large flux of sputtered atoms coming from the target. Within a few μs collisions of the sputtered atoms with the working gas atoms leads to heating and expansion of the working gas, known as rarefaction. As a result, the working gas atoms are replaced by the sputtered atoms in the vicinity of the cathode target to some extent as the pulse evolves. However, it has been shown that the rarefaction is primarily due to ionization losses in the target vicinity (Huo et al., 2012). The rarefaction causes the discharge current to fall as can be seen for pressures in the range 0.33 – 0.73 Pa.

3.1.3 Importance of ionization fraction

In order to understand effect of ionization fraction as major difference between evaporation, dcMS and HiPIMS, we utilized molecular dynamic simulation (Allen and Tildesley, 1989). To this end we assumed Cu body with its (111) plane exposed as substrate and more than 22000 Cu adatoms were inserted 150 nm above substrate surface. The thermal evaporation, dcMS and the HiPIMS flux were assumed to be fully neutral, 50 % ionized and fully ionized, respectively. The novelty of this work is not limited to ionization fraction but also applying an energy distribution to the incident flux. Further details on the simulation procedure can be found elsewhere (Kateb et al., 2019c).

Figure 3.2 shows the top view of the films deposited by thermal evaporation, dcMS and HiPIMS with identical deposition time and energy distribution. The dark blue here shows the substrate surface and atoms that are 6 nm above the substrate are identified by

red. It can be clearly seen that the thermal evaporated film presents very rough surface compared to the sputtered films. This is due to the fact that during thermal evaporation neutral atoms form clusters before arriving at film/substrate surface. One may think the surface roughness obtained in thermal evaporation here is an artificial effect of relatively high deposition rate or short simulation time compared to time required for surface diffusion. Such island growth has been reported for deposition of Cu on Cu with experimental rate and modeling diffusion process through accelerated dynamic simulation (Hubartt et al., 2013). Thus, the film obtained by thermal evaporation is extremely non-uniform at the atomic level. In the HiPIMS deposition, however, the repulsion between ions does not allow clustering when maximum uniformity of deposition occurs as can be seen in figure 3.2(c). Due to distribution of energy in the flux, neutrals/ions with higher kinetic energy are able to diffuse longer at the surface than low energy adatoms. As a result formation of islands is still possible in the ionized flux case. The secondary mechanism here is energetic impacts of ions into subsurface atoms which causes local amorphization and fills the gaps between islands with atomically flat surface. The energetic ions themselves are the result of strong repulsive force between ions. Further collision of energetic ions cause recrystallization of amorphous regions which maintain smooth surface. We observed both of the above mentioned mechanisms i.e. clustering and energetic collision during dcMS deposition that give an intermediate surface roughness as seen in figure 3.2(b).

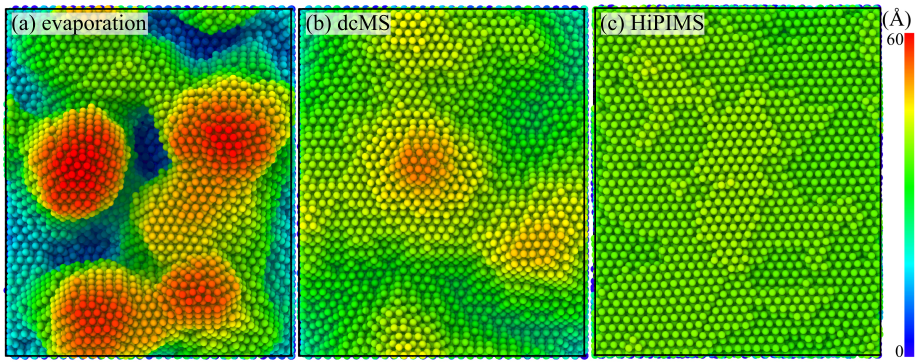

Figure 3.2. The surface topology obtained using (a) thermal evaporation (b) dcMS and (b) HiPIMS deposition with similar deposition time and energy distribution. The deep blue indicates substrate surface and red denotes 6 nm above the substrate surface.

Figure 3.3 shows the sequence of amorphization and crystallization events during HiPIMS deposition. Figure 3.3(a) shows the film before collision and which seems single crystalline aside from some stacking fault areas. In figure 3.3(b) it can be clearly seen that an amorphous region appears in the film deep down to the bottom of the substrate. The amorphization during bombardment has been reported previously. (Dong and Srolovitz, 1998; Houska, 2014) As time passes the amorphous phase disappears as shown in figure 3.3(c) – (d). It is worth noting that after amorphization and recrystallization the film microstructure has remained nearly unchanged.

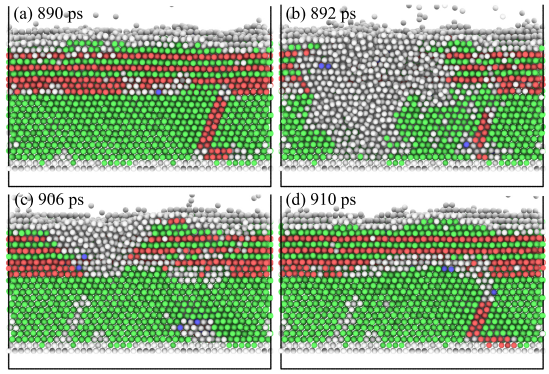

Figure 3.3. The sequence of amorphization and crystallization during HiPIMS deposition due to high energy ion bombardment. (a) Before collision at 890 ps, (b) right after high energy collision at 892 ps, and (c – d) after secondary collisions at 906 – 910 ps. The red, green, blue and white atoms respectively are fcc, hcp, bcc and disordered atoms.

3.1.4 Advantage of HiPIMS for magnetic materials

It is well known that the electrical and magnetic properties of ferromagnetic thin film are influenced by the deposition conditions and method (Collins et al., 1981; Yang and Aboaf, 1989). We have recently shown that a tilt deposition geometry with respect to the substrate normal during dcMS deposition induces strong in-plane uniaxial anisotropy, i.e. a square easy axis with sharp transitions and a linear hard axis without hysteresis (Kateb and Ingvarsson, 2017; Kateb et al., 2019d). These are desirable properties for applications such as magnetic memories and field sensors. However, tilt sputtering at high working gas pressures, which is more appropriate for large industrial applications, has not been studied yet. This is mainly because tilt deposition requires low working gas pressure as it suffers from scattering of the sputtered flux by the working gas at high pressures (Barranco et al., 2016). There is also a competition between in-plane and out-of-plane anisotropy in Py films. It has been shown that for both dcMS and evaporation, increased pressure reduces in-plane uniaxial anisotropy accompanied with losing magnetic softness (Sugita et al., 1967; Fujiwara and Sugita, 1968; Svalov et al., 2010). Regardless of the deposition method, the poor in-plane anisotropy was associated with formation of stripe domains at thicknesses beyond the critical thickness. The critical thickness decreases dramatically with increased pressure of working gas (Sugita et al., 1967; Fujiwara and Sugita, 1968; Svalov et al., 2010), e.g. it is about 250 nm at 0.38 Pa and decreases to 60 nm at 2.4 Pa using dcMS deposition (Svalov et al., 2010). Since, higher working gas pressure during deposition increases surface roughness and encourages void-rich structure in the case of Py (Kools, 1995), a decrease in the critical thickness was attributed to an increase in the surface roughness (Svalov et al., 2010) and increase in density of defects and voids (Sugita et al., 1967; Fujiwara and Sugita, 1968) with increased pressure. An interesting solution to overcome void-rich structure and rough surface is offered by HiPIMS. This is a direct consequence of

ionization fraction as described earlier.

It has been shown that amorphous magnetic films of $Fe_{73.5}CuNb_3Si_{15.3}B_7$ can be grown by HiPIMS and they are claimed to have the same composition as the target over wide range of pressures (Velicu et al., 2012). This is important since dcMS has been found to present 2.3 *at.%* change in iron content of Py by changing the pressure in the 0.38 – 2.4 Pa range (Svalov et al., 2010) which can have significant effect on the magnetic properties, as discussed e.g. by O'Handley (2000, p. 190 & 369).

Another interesting feature of HiPIMS deposition is a high film density which, together with smoother surface determine quality of multilayers. It has been already shown using Monte Carlo simulation that when an ion with a few hundreds of eV energy strikes the surface of a low density film, with less than 80 % of theoretical density, it can penetrate to an average depth of a few nm (Müller, 1986a,b). Thus it is important to maintain density as high as possible to reduce intermixing between layers. This also stops underlayer atoms to diffuse into top layer as schematically shown in figure 3.4.

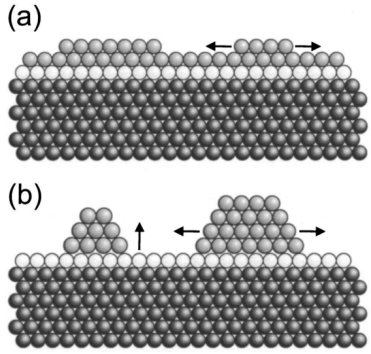

Figure 3.4. Schematic illustration of growth of multilayer using (a) HiPIMS and (b) dcMS. The black, white and gray atoms respectively are substrate, underlayer and top layer atoms. Arrows are indicating probability of diffusion.

Besides HiPIMS present a few more practical advantages when it comes to growth of multilayers. To grow delicate multilayers it is necessary to control deposition rate in which is reduced by reduction of power in a dcMS deposition. We would like to remark that in the growth of multilayers, substrate temperature is limited, commonly below 160 °C, to minimize unwanted diffusion and dewetting. Thus lowering the power in dcMS means lowering adatom energy and increasing the chance of defect formation. Besides, depending on the pressure, using low power might leads to scattering flux and eliminating tilt effect for dictating magnetization axes. In HiPIMS we have at least two more degree of freedom, i.e. the *average deposition rate* can be controlled by both pulse width and repetition frequency while maintaining or even increasing power density. Another important aspect of HiPIMS is presenting high *instantaneous deposition rate* during the pulse, more than 50 times (Kateb et al., 2018). In the following chapter, we utilize this aspect to control atomic order in a single crystal Py. In addition, a high instantaneous deposition rate is accompanied with a smoother and higher density than dcMS deposited film. This means more monolayers of top layer are formed during the

pulse which limits diffusional intermixing. In the next chapter it will be shown how sharp interfaces is achieved in Py multilayers prepared by HiPIMS.

The advantages of HiPIMS over dcMS regarding the magnetic films can be summarized as below:

- High density
- Low surface roughness
- High instantaneous deposition rate during the pulse
- Low average deposition rate
- Maintaining target composition in the film
- Higher adatom energy that maintains advantage of tilt deposition at high pressures

3.2 Anisotropic magnetoresistance

The presence of an external applied field can cause a change in resistivity. In the classical description, this is caused by Hall effect i.e. conduction electrons those are forced into cyclotron orbits about the applied field and do not contribute to the current density (O'Handley, 2000, p. 568). Kohler discovered the fact that the resistivity change is proportional to the applied field:

$$\frac{\delta\rho}{\rho_0} \propto \left(\frac{H}{\rho_0}\right)^2 \tag{3.1}$$

where $\delta\rho$ is the change of resistivity, ρ_0 is the electrical resistivity at zero field. For a ferromagnetic material Eq. (3.1) takes the following form due to *anomalous Hall effect*:

$$\frac{\delta\rho}{\rho_0} \propto a\left(\frac{H}{\rho_0}\right)^2 + b\left(\frac{H}{\rho_0}\right)^2 \tag{3.2}$$

where a and b are proportionality factors an M is internal magnetization. The first term is *ordinary magnetoresistance* and the second is *anisotropic magnetoresistance* which insists on the state of magnetization rather than the applied field.

3.3 Anisotropic magnetoresistance measurement

The result of the AMR measurements can be affected by the measurement technique (McGuire and Potter, 1975). Bozorth (1946) believed sweeping magnetic field perpendicular to the current direction, specially without knowing sample magnetization direction, makes comparison of the AMR results difficult. Figure 3.5 shows a typical AMR measurement obtained by sweeping magnetic field in a Py film. It can be clearly seen that the value of $\delta\rho$, maximum resistivity change measured by applying magnetic

field perpendicular to the current direction, is smaller than $\Delta\rho$ obtained by applying M_{sat} parallel and perpendicular to the current. Besides, measurement with magnetic field applied parallel to the current direction (orange line) gives a different $\delta\rho$ for the same sample. Bozorth (1946) showed that determining AMR by applying M_{sat} parallel and perpendicular to the current direction avoids erratic results in the literature caused by ignoring the initial magnetization state of the specimen. Since then the AMR ratio is given by:

$$\text{AMR} = \frac{\Delta\rho}{\rho_{\text{ave}}} = \frac{\rho_{\parallel} - \rho_{\perp}}{\rho_{\text{ave}}} \tag{3.3}$$

here ρ_{ave} for an fcc materials like Py can be estimated by (McGuire and Potter, 1975):

$$\rho_{\text{ave}} = \frac{1}{3}\rho_{\parallel} + \frac{2}{3}\rho_{\perp} \tag{3.4}$$

where $\rho_{\parallel}$ and $\rho_{\perp}$ are resistivities with magnetization saturation parallel and perpendicular to the current direction, respectively. The reason for utilizing ρ_{ave} that depends on $\rho_{\parallel}$ and $\rho_{\perp}$ is the fact that the state of magnetization and demagnetization in a multidomain sample is not unique. Thus, in contrast with ρ_{ave}, ρ_0 utilized in Eq. (3.1) is not well defined.

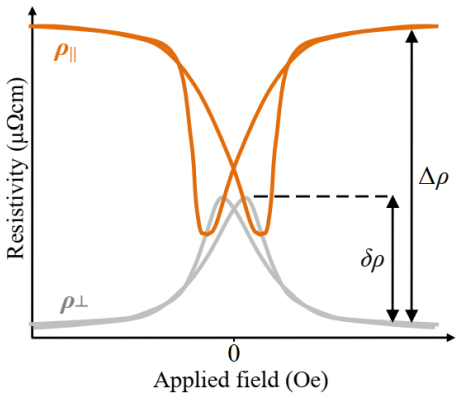

Figure 3.5. Typical AMR measurement of Py film obtained by sweeping magnetic field parallel (orange) and perpendicular (gray) to the current probes.

Assuming the x-axis being the current direction and $\rho_{\parallel}$ being higher than $\rho_{\perp}$ in the saturated magnetic field (cf. figure 3.5), the AMR response can be presented as ρ_x which only depends on the direction of saturated magnetization

$$\rho_x = \rho_{\perp} + \Delta\rho \cos^2 \Phi \tag{3.5}$$

here Φ stands for angle between current (x) and M_{sat} direction. A typical AMR measurement of Py film obtained by rotation of M_{sat} is shown in figure 3.6.

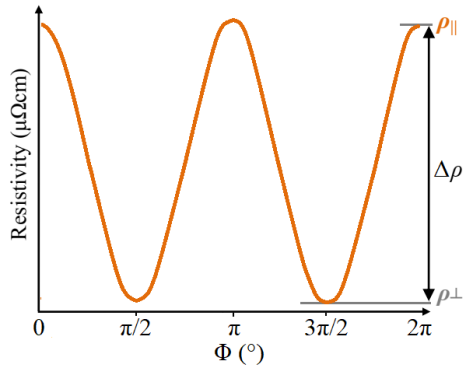

Figure 3.6. Typical AMR measurement of Py film obtained by rotation of M_{sat} and fixed current probes.

3.3.1 Anisotropic resistivity measurement

Resistivity measurements have been long a vital part of solid state electronics characterization offering a wide range of applications from classification of materials to detection of phase transition in advanced superconductors. Various methods have been introduced for the resistivity measurements but not all of them could easily reflect the broken symmetry of materials in the form of anisotropic resistivity tensor (Miccoli et al., 2015). Some of those methods involve cutting out samples (van der Pauw, 1961; Montgomery, 1971) or placing probes on a sample (Wasscher, 1961; Auby and Bernard, 1969) in different orientation. For instance, to determine the principle resistivity axes of an anisotropic film, one can make two Hall-bars along the these axes and simply determine resistivity from Pouillet's law (van der Pauw, 1961; Kateb et al., 2018). Although, the error of the bar size can be improved by proper lithography techniques, an additional source of error arises from aligning the bar along the direction of interest. It is worth mentioning that in principle, two bars cut in unknown directions are sufficient to determine the resistivity tensor of a film. In practice, however, determining off-diagonal elements is very sensitive to misalignment of voltage probes which mostly gives inaccurate results (van der Pauw, 1961). Alternatively, co-linear or square arrangement of four-point-probes is preferred since aligning them parallel to the principle resistivities of the film is easier than making bars. Regarding anisotropic material, it has been shown by two different mathematical approaches that square arrangement provides much higher sensitivity (Wasscher, 1961; Auby and Bernard, 1969). In both of these methods the geometric factor, i.e. proportionality factor of resistivity to voltage-current ratio, has been calculated under assumptions such as infinite and semi-infinite planes (Valdes, 1954; Uhlir, 1955; Swartzendruber, 1964) those are never realized in practice.

3.3.2 van der Pauw measurement

An interesting method was introduced by van der Pauw (vdP) (van der Pauw, 1958a,b) for determining *isotropic* resistivity of uniform and continuous thin films of arbitrary

shape. In the vdP method, four small contacts must be placed on the sample perimeter as illustrated in figure 3.7. The measured resistances should satisfy the vdP equation:

$$\exp\left(-\frac{\pi d}{\rho_{\text{iso}}}R_{\text{AB,CD}}\right)+\exp\left(-\frac{\pi d}{\rho_{\text{iso}}}R_{\text{BC,DA}}\right)=1 \tag{3.6}$$

where ρ_{iso} is the isotropic resistivity and d is the film thickness. The resistance $R_{\text{AB,CD}}$ is measured by forcing current through AB and picking up the voltage at the opposite side between CD and $R_{\text{BC,DA}}$ is similarly defined.

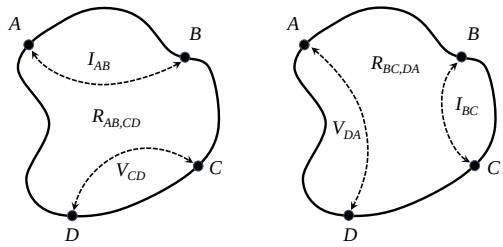

Figure 3.7. Schematic illustration of two sets of measurements in the vdP method.

Eq. (3.6) appears to be independent of sample shape and contact distances. This behavior is directly related to conformal mapping i.e. a sample has been mapped upon a semi-infinite half-plane with contacts along the edge in which the contact distances cancel each other.

In order to solve Eq. (3.6) vdP suggested:

$$\rho_{\text{iso}}=\frac{\pi d}{2\ln 2}(R_{\text{AB,CD}}+R_{\text{BC,DA}})f\left(\frac{R_{\text{AB,CD}}}{R_{\text{BC,DA}}}\right) \tag{3.7}$$

where f is only a function of ratio $R_{\text{AB,CD}}/R_{\text{BC,DA}}$ and satisfies the relation:

$$\frac{R_{\text{AB,CD}}-R_{\text{BC,DA}}}{R_{\text{AB,CD}}+R_{\text{BC,DA}}}=f\operatorname{arccosh}\left[\frac{\exp(\ln 2/\text{f})}{2}\right] \tag{3.8}$$

Wasscher (1969) pointed out that Eq. (3.8) deviate from correct curve by a few percent and developing iterative methods to solve Eq. (3.6) was a popular topic for a few decades.

3.3.3 Price extension to anisotropic medium

It has been shown that the vdP measurement can be extended to the anisotropic case if a planar sample is made perpendicular to one (out of three) of principle resistivity axis. Thus, ρ_{iso} obtained from Eq. (3.6) stands for the geometric mean of in-plane principle resistivities i.e. $\rho_{\text{iso}}=\sqrt{\rho_1\rho_2}$ (Hornstra and van der Pauw, 1959; Price, 1972). It has also been shown that principle resistivities can be determined using vdP method e.g. by making rectangle sample with sample sides parallel to principle resistivities (Hornstra and van der Pauw, 1959; Montgomery, 1971; Price, 1973)

3.3.4 Kleiza extension to anisotropic medium

Kleiza et al. (Kleiza et al., 2007; Ašmontas et al., 2008) theoretically demonstrated two different extension of the vdP method to determine off-diagonal element(s) of the resistivity tensor. These methods are schematically shown in figure 3.8. In this regard, ρ_{iso} of the film is treated as determinant of the resistivity tensor $\rho_{\text{iso}} = \sqrt{\rho_{xx}\rho_{yy} - \rho_{xy}^2}$. This is consistent with the previous notation since off-diagonal elements are essentially tend to zero in measurement parallel to the principle resistivities. Recently, Borup et al. (2015) have shown that the resistivity tensor of a single crystal thermoelectric can be obtained based on the Kleiza et al. (2007) extension. However, the later method requires making a few samples of the form parallelogram with different angles which is difficult and may contribute to the measurement error. The second method proposed by Ašmontas et al. (2008) is based on adding fifth point to the side of rectangular sample. Such geometry allows measurement of voltage drop perpendicular to current probes. For instance, one can force the current through AB and read the voltage over DE. In this case knowing the length ratio of DE/AD is necessary.

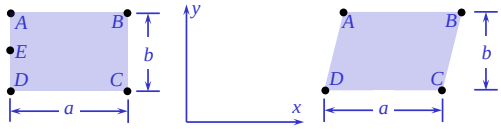

Figure 3.8. Schematic illustration of (left) five points (Ašmontas et al., 2008) and (right) reshaping (Kleiza et al., 2007) methods for determining full resistivity tensor of the film.

3.3.5 Extended van der Pauw method of anisotropic magnetoresistance measurement

The AMR measurement method proposed by Bozorth (1946) can be easily applied to the Hall-bar techniques when the current direction is confined along the bar axis. However in the vdP method or even linear four-point-probe the current is dispersed in different paths. Thus, using the vdP method in AMR measurements it was not realized for very long time despite the suggestion of McGuire and Potter (1975). We have recently shown that knowing the direction of easy and hard axis of the film one can decouple ρ_{iso} obtained in vdP measurement to values along easy (ρ_{easy}) and hard (ρ_{hard}) axis. Thus applying saturation magnetic field along easy and hard axis allows determining AMR along those axis. We have shown that this method gives AMR values in close agreement i.e. consistent with the AMR definition by Bozorth (1946). While two Hall-bars patterned along the easy and hard axis present considerable difference in AMR values. Thus one can measure AMR using vdP only by saturation magnetic field in one direction.

We have recently shown that tilt sputtering of permalloy $Ni_{80}Fe_{20}$ induces strong in-plane uniaxial anisotropy in the resulting film (Kateb and Ingvarsson, 2017; Kateb et al., 2019d). However, Hall-bar methods fails to describe anisotropy of NiFe while Price extension of vdP methods gives consistent result by measurement along principle axis of

the film (Kateb et al., 2019d, 2018). Although the Price method gives diagonal element of resistivity tensor it is limited in the case of off-diagonal elements. Thus Price method is promising for AMR measurements but it suffers from providing information for planar Hall effect (PHE). In the present study we extend our discussion to determine second rank resistivity tensor using extended vdP measurement which enables simultaneous AMR and PHE measurement.

4 Uniaxial anisotropy induced by tilt deposition

In the first part of this chapter we intend to understand the origin of uniaxial anisotropy. To this end, we examine previous mechanism proposed for uniaxial anisotropy induced by tilt deposition. In particular we try to make smooth film that is indication of no self-shadowing to see if self-shadowing is important. As mentioned earlier, self-shadowing has been known to generate off-normal texture. We also grew films with normal texture to examine if off-normal texture is responsible for uniaxial anisotropy. Furthermore, we grew single crystals and demonstrated conditions at which uniaxial anisotropy can be achieved.

In the second part, we are trying to study interface or surface anisotropy in ultra-thin Py in the form multilayers. We demonstrate importance of strain on the uniaxial anisotropy which is more pronounced at a sharp interface and can be suppressed by a diffused interface in a multilayer.

4.1 Polycrystalline permalloy film

4.1.1 Tilt deposition vs *in-situ* magnetic field

We compared hysteresis loops of samples deposited without and with *in-situ* magnetic field in parallel and perpendicular directions to the plane of incidence. As indicated in figure 2.10, tilt deposition induces a hard axis in the incident plane of the atomic flux. Thus applying a magnetic field parallel to the atomic flux projection in the film plane would compete with the tilt effect while a perpendicular field reinforces the tilt induced easy magnetization axis.

It has been shown that competing magnetic field does not change the direction of easy axis dictated by the tilt angle (Kateb and Ingvarsson, 2017). In this regard, we are comparing applying 70 Oe external magnetic field, which is more than twice the saturating field, with a 35° tilt angle with respect to the substrate. Besides, we have been rotating the sample back and forth with 300 ms stop time during growth. Thus, despite of the fact that we have tried to minimize the tilt effect it was more efficient than the *in-situ* magnetic field. It is also worth mentioning that both of assisting and competing field increased the H_c. We studied this further and compared the result of tilt deposition without field and for 20 and 70 Oe assisting field (Kateb et al., 2019d). It is shown that 20 Oe magnetic field gives an intermediate H_c and H_k between that of no field and 70 Oe field. These two simple experiment indicate that the tilt deposition and *in-situ* magnetic field during growth might have different origin and mechanism for

contribution to the magnetic behavior. Thus, it is important to study the origin of the uniaxial anisotropy that is induced by the tilt deposition.

4.1.2 Effect of self-shadowing

Figure 4.1 shows the XRR curves of a series of thin films with various thicknesses. The figure also contains the fitting which is necessary to determine film thickness, density and roughness. To get the best fits an oxide layer and a water layer were included in the fit procedure, which is reasonable since the measurements were done under ambient conditions. The thicknesses of the samples indicate a stable growth rate of precisely 1.2 Å/s. The mass densities of the films show very slight fluctuation around their average of 8.61 g/cm^3. The uncertainty in the fit results decreases at higher thicknesses since there is more film material exposed by X-ray and more fringes to fit. The surface of the films present excellent smoothness, with X-ray results showing about 2 Å surface roughness. For a few samples the roughness was verified by AFM, which gave results in the range 1.9–2.8 Å RMS. Even though there appeared to be a slight difference in the roughness obtained in XRR fit and AFM both methods verify the extreme smoothness of our films. Thus, speaking of self shadowing is irrelevant in these films. This is interesting since all these films presenting very well-defined uniaxial anisotropy.

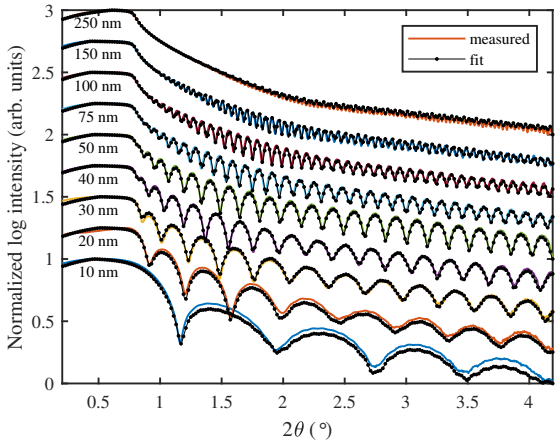

Figure 4.1. The measured and fit XRR curves of different Py films with 10–250 nm thicknesses. The curves have been offset manually in the vertical direction for clarity.

Briefly, polar mapping of important crystal planes is a useful technique to study texture in the materials (Mahieu et al., 2006). Pole figures are measured at constant $\theta - 2\theta$, corresponding to a specific crystal planes separation, and rotation of specimen in film plane (ϕ) and out of plane (ψ). In the case of polycrystalline Py (111) is the major peak with highest intensity. Figure 4.2 shows the (111) pole figures of Py films with thicknesses greater than 50 nm. We do not display pole figures of thinner films as it is very difficult to collect meaningful signal from them in XRD (Rijks et al., 1997). However, we plotted three column i.e. raw data on the left, middle column

after subtracting substrate pattern and right column shows each thickness by next lower thickness. It can be seen that the vortex like pattern between $\psi = 35 - 65^{\circ}$ coming from substrate (p-Si with a smooth 100 nm thermally grown oxide) as it disappeared in the middle column. Looking into middle column, it can be seen that there is strong (111) texture normal to film plane $\psi = 0$. Thus, there is no sign of off-normal texture to be responsible for uniaxial anisotropy.

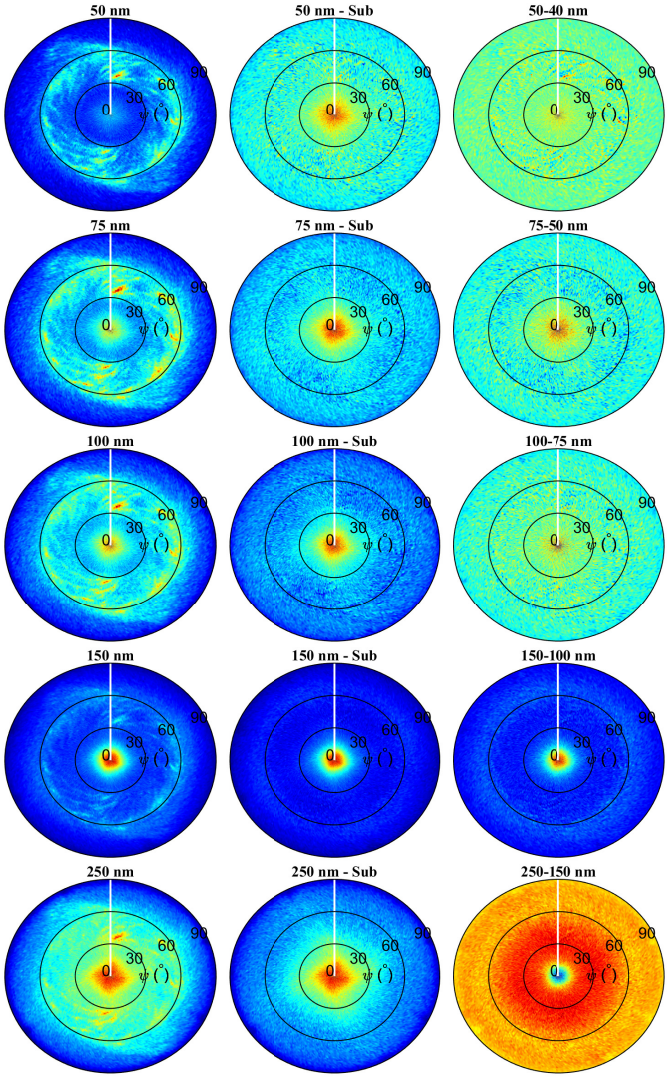

Figure 4.2. Pole figures of the (111) planes of 50–250 nm thick films. Raw data (left) before, (middle) after subtracting the substrate and (right) after subtracting the next thinner film patterns. The white line indicates the direction of the sputtered flux during stop time. Colorbar indicate normalized intensity.

The 3rd column in figure 4.2 illustrates how growth mode changes within a specific thickness. For instance, between 50–75 and 100–150 nm thicknesses (111) texture normal to the film plane becomes dominating. To explain this further we present resistivity measurement using the vdP method. Figure 4.3 shows the resistivity measurement of our film in comparison with previously reported results. It can be seen that resistivity of 75 and 150 nm film deviates from dashed lines which is the best fit with the Fuchs (1938) model. Thus, as the (111) normal texture becomes dominant the resistivity decreases. We found full agreement between our result and that of Solt (1985) deposited under similar growth condition.

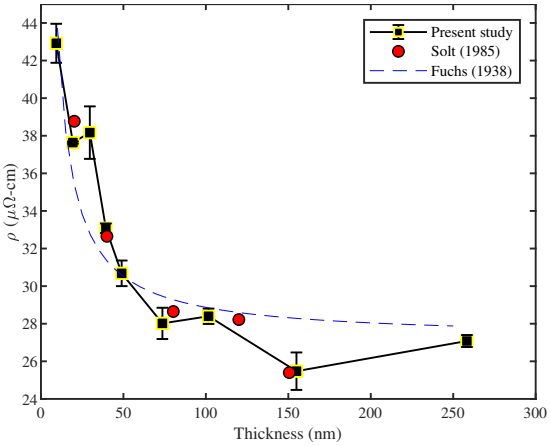

Figure 4.3. Variation of resistivity with the film thickness in present study in comparison with Solt (1985) result. The solid black line in our result is plotted to aid the eye. The dashed line indicate the best fit to Fuchs (1938) model.

4.1.3 Comparison of dcMS and HiPIMS

As mentioned in the introduction chapter, for many applications it is important to have very well-defined magnetic axes. Figure 4.4 shows the average of a few loops obtained by set of MOKE measurements for the films deposited at room temperature. The films deposited at 100 °C present similar results for dcMS and HiPIMS that are not shown here. It is clear that the entire set of films present very well-defined uniaxial anisotropy i.e. a square easy axis with sharp switching and a linear hard axis without opening. It can be seen that dcMS deposited films most of the time present higher saturation fields than their HiPIMS counterparts deposited at the same pressure. This is more evident in the films deposited at higher working gas pressures of 0.53 – 0.73 Pa. Besides, dcMS films start to become harder almost immediately (at 3.3 Pa) while HiPIMS films are remaining soft till 0.53 Pa.

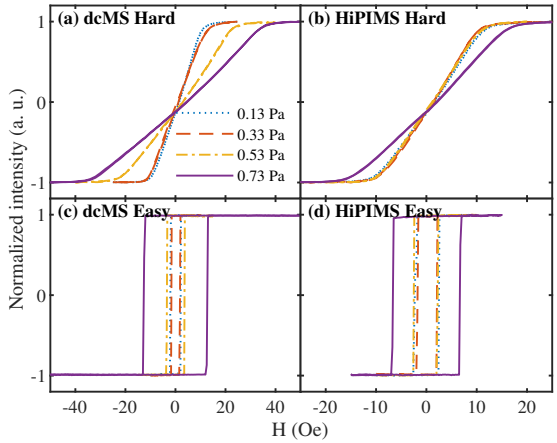

Figure 4.4. The MOKE response of the films deposited by dcMS and HiPIMS at room temperature measured along hard and easy axes of the films.

We extracted H_k and H_c from MOKE loops and figure 4.5 shows their variation with working gas pressure for both dcMS and HiPIMS deposited films. The densities of the films are also shown in the figure inset. It can be clearly seen that H_k increases with increased working gas pressure for dcMS deposited films at room temperature. On the other hand films deposited by HiPIMS at room temperature exhibit nearly constant H_k independent of working gas pressure. Both dcMS and HiPIMS deposited films at 100 °C also present nearly constant H_k. Since higher temperature enables adatom surface diffusion and encourages defect free crystal growth, it can be concluded that H_k reduced at higher film densities. It is worth mentioning that surface roughness increased with increasing working gas pressure in all cases (not shown here).

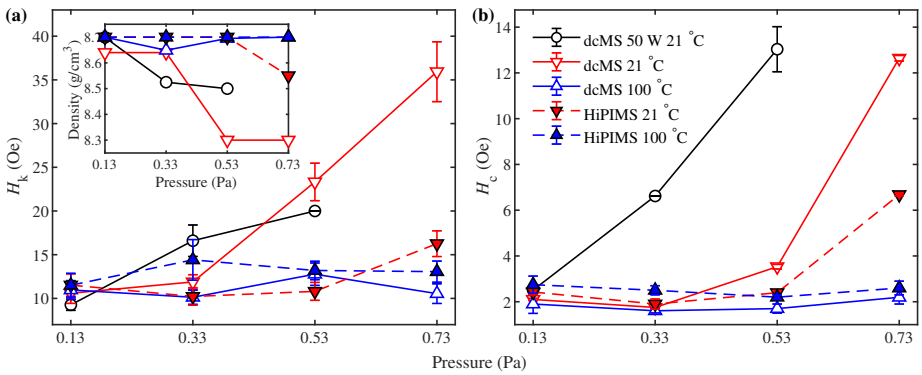

Figure 4.5. The (a) anisotropy field (H_k) and (b) coercivity field (H_c) of the film deposited with the same thickness at different working gas pressures. These values extracted from MOKE measurements along hard and easy axis, respectively. The figure inset shows density variation at different pressures.

The variation of H_c with the working gas pressure is shown in figure 4.5(b). It is clear that there is a threshold pressure for increase in H_c for room temperature grown films. This behavior is similar to density variation with pressure. For 50 W dcMS grown films, pressures higher than 0.13 Pa causes an increase in H_c while for those films grown at 150 W dcMS and HiPIMS the threshold pressure is 0.53 Pa and H_c increases afterwards. Again due to higher density at 100 °C, there is no such threshold for those films. Considering the fact that the surface roughness is increasing with the working gas pressure in all cases, the present result is consistent with Choe (1999). They reported a dramatic increase H_c with surface roughnesses higher than 8 Å due to surface roughness induced pinning of domain walls. We obtained minimum surface roughnesses between 6 – 8 Å at 0.13 Pa up to 12 – 28 Å at 0.73 Pa. Thus, maintaining H_c at 100 °C, here, indicates its dependence on the density rather than surface roughness.

Although we have tried to make a relation between density and magnetic properties, at this point, we are still unaware of the mechanism that is directly related to density. We leave this discussion open till end of this chapter.

4.2 Permalloy single crystal

In the next step towards understanding the mechanism of the uniaxial anisotropy induced by tilt deposition we studied single crystal Py. The single crystals were grown on (001) MgO single crystals at 400 °C by both dcMS and HiPIMS. We skipped any cleaning of the substrates before deposition except baking them at growth temperature for an hour for the purpose of dehydration.

4.2.1 Characterization single crystals

Figure 4.6 illustrates the normal (symmetric $\theta - 2\theta$) XRD pattern of the epitaxial films obtained by dcMS and HiPIMS deposition. In the normal (out-of-plane) XRD, fcc (002) peak is the only detectable Py peak. This indicates that the (002) planes of Py are very well aligned to that of the MgO substrate i.e. Py (001) $\parallel$ MgO (001). Similar results were obtained by in-plane measurement ($\psi = 90°$) along the [100] directions of MgO i.e. normal to substrate edges. Furthermore, in-plane measurements along the $\langle 110 \rangle$ direction of MgO (substrate diagonals) show (220) peaks from both the MgO substrate and the Py film. These indicate a orientation relationship of Py [100] $\parallel$ MgO [100] and Py [110] $\parallel$ MgO [110] i.e. the [100] and [110] directions of Py are fully aligned with those of the MgO substrate. Thus, in spite of the large lattice mismatch (15.84%), high quality single crystal Py ($a_{Py} = 3.548$ Å) film can be established on a MgO ($a_{MgO} = 4.212$ Å) substrate for both deposition techniques. Furthermore, we compared the in-plane peaks along the $\langle 100 \rangle$ and $\langle 010 \rangle$ directions (not shown here) and detected no difference in lattice parameter even with a precise scan i.e. angular resolution 0.0001° and 10 s counting time. This means we observed identical in-plane strain along the [100] directions in both of the films.

In the dcMS case, the Py (002) peak shows a slight shift towards higher angles in the normal XRD scan. This is accompanied by the shift of in-plane peaks towards

smaller angles. Tanaka et al. (2010) believed tensile strain at the film-substrate interface generates slight compression normal to the film plane. However, in the HiPIMS case, both the in-plane *and* out-of-plane peaks are shifted towards smaller angles. This would indicate tensile strain in all tree dimension which is impossible. Thus, we attribute the shift of (002) peak to left and right moving towards and away from the $L1_2$ Ni_3Fe superlattice, respectively. It has been shown that an ordered phase can be detected as a shift of the XRD peaks towards larger angles (Chikazumi, 1950; O'Handley, 2000; Wan et al., 2005) and narrower peaks (Lutts and Gielen, 1970; Wan et al., 2005). In addition, the intensity of the XRD peaks is expected to increase with the higher order (O'Handley, 2000, p. 549). All these conditions can be observed in our dcMS deposited film, indicating that it is more ordered than its HiPIMS counterpart. The more disordered arrangement in the HiPIMS deposition can be attributed to the high deposition rate during each pulse which suppresses adatom mobility.

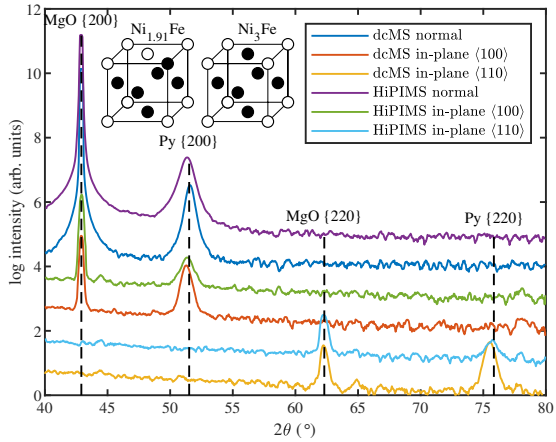

Figure 4.6. The symmetric XRD pattern of the epitaxial films deposited by dcMS and HiPIMS. The vertical dashed lines show the peak position of bulk Py and MgO. The curves are shifted manually for clarity.

Figure 4.7 illustrates pole figures for the main Py planes of our epitaxial films. In the {200} pole figure, there is an intense spot at $\psi = 0$ that verifies that the (002) plane is lying parallel to the substrate i.e. epitaxial relationship of Py(001) ∥ MgO(001) for both dcMS and HiPIMS deposited films. There is also a weak spot with four-fold symmetry at $\psi = 90^\circ$ due to in-plane diffraction of {200} planes parallel to substrate edges in both films. This indicates there are Py {100} planes parallel to the substrate edges i.e. Py[100] ∥ MgO[100]. The {220} pole figures, also depict four-fold symmetry of {220} planes at ψ angle of 45 and 90° as expected from symmetry in a cubic single crystal for both films. In both of the {111} pole figures, there is a four-fold spot at $\phi = 45^\circ$ and $\psi = 54.74^\circ$ which is in agreement with the angle between (002) and {111} planes. The FWHM of the spots are always narrower for the dcMS deposited epitaxial film indicating higher order in this case.

The extra dots that appear in the {111} pole figure of the HiPIMS deposited film

belong to twin boundaries (Chen et al., 2013; Cemin et al., 2017). The existence of twin boundaries in the Py is a signature of high deposition rate which has been observed previously in evaporated films (Baltz, 1963; Yelon et al., 1965) and studied in detail using TEM (Baltz, 1963; Thangaraj et al., 1995; Ross et al., 1996). It can be seen that these dots at 23° also appear in the dcMS deposited film but with very small intensity. This indicates that the fraction of twin boundaries is much lower in the dcMS deposited film than the HiPIMS counterpart. In addition, there are three spots with four-fold symmetry in the {200} pole figure of the HiPIMS deposited film which do not appear in the dcMS counterpart which has been characterized as an auxiliary sign of twin boundaries (Cemin et al., 2017).

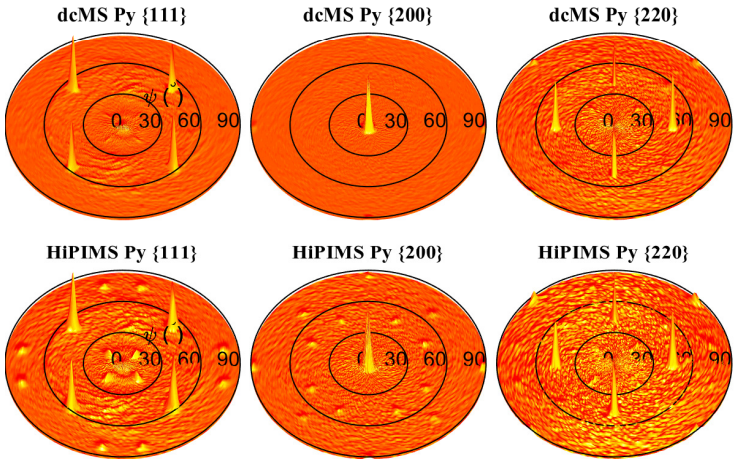

Figure 4.7. The pole figures obtained for Py {111}, {200} and {220} planes of epitaxial films deposited by dcMS and HiPIMS. The height represents normalized log intensity (arb. units).

4.2.2 Inducing uniaxial anisotropy using HiPIMS

Figure 4.8 compares the results of in-plane MOKE measurements along the [100] and [110] directions of both the epitaxial films. Figure 4.8(a-b) indicate a biaxial behavior in the dcMS deposited film consisting of two easy axes along the [110] directions with H_c of ∼2 Oe. This is consistent with the ⟨111⟩ direction being the easy direction of the Py crystal and the magnetization being forced in-plane along the ⟨110⟩ directions due to shape anisotropy (Yelon et al., 1965; Ohtake et al., 2011). Along the [100] directions the MOKE response is relatively hard i.e. open hysteresis with a gradual saturation outside the hysteresis (figure 4.8(a)). This behavior is very similar to what was shown in figure 2.6. Besides, the ⟨100⟩ and ⟨010⟩ directions are not completely equivalent for our dcMS deposited film. The ⟨100⟩ direction presents larger coercivity (∼2 Oe) and saturates at 12 Oe but the ⟨010⟩ direction gives ∼1 Oe coercivity and saturates at 15 – 18 Oe. This difference arises from the fact that ⟨100⟩ is the direction of sputter flux during the 300 ms stop time while reversing the rotation.

So far, our dcMS results are complementary to that of Chikazumi (1956, 1961), i.e. in addition to annealing and *in-situ* magnetic field, it is also hard to achieve uniaxial anisotropy along the [100] directions using tilt deposition. However, as shown in figure 4.8(c-d) the HiPIMS deposited epitaxial film shows well-defined uniaxial anisotropy along the [100] directions. The H_k is 3.5 Oe, i.e. much lower than that of our polycrystalline films (11 – 14.5 Oe) (Kateb et al., 2018). However the H_c of 1.8 Oe here is very close to that of polycrystalline films i.e. 2 – 2.7 Oe.

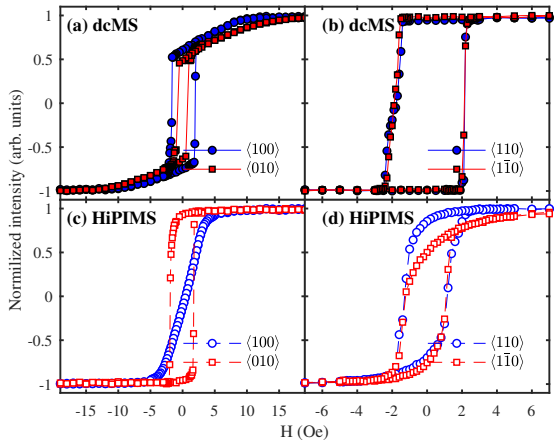

Figure 4.8. The average hysteresis loops of the epitaxial films obtained by MOKE measurements along the [100] and [110] directions of the epitaxial Py films.

4.2.3 Proof of atomic order via AMR measurement

As the resistivity of Py changes in different direction due to its internal magnetization we measured its anisotropic resistivity by rotation of M_{sat} in the film plane. Figure 4.9 shows the AMR response of epitaxial films to the rotation of in-plane M_{sat} (24 Oe). The θ here stands for angle between M_{sat} and the $\langle 100 \rangle$ direction of films and should not to be confused with the Φ in Eq. (3.5), i.e. the angle between current direction and magnetic field. The result of Eq. (3.5) is also plotted for comparison as indicated by the black line. Even though, the dcMS deposited film is thinner than the HiPIMS counterpart, the resistivities in the dcMS case are all lower than the HiPIMS ones. This behavior indicates higher order in the dcMS deposited film. Hausmann et al. (1971) have already showed that the resistivity depends on the order and decreases upon increase in order.

It can be seen that the AMR response of the epitaxial film deposited with HiPIMS conforms better with Eq. (3.5) while dcMS counterpart shows some deviation. The deviation began around the easy axes and continues almost till the hard axis at 90 and 270° ($\langle 010 \rangle$ and $\langle 0\bar{1}0 \rangle$ orientations).

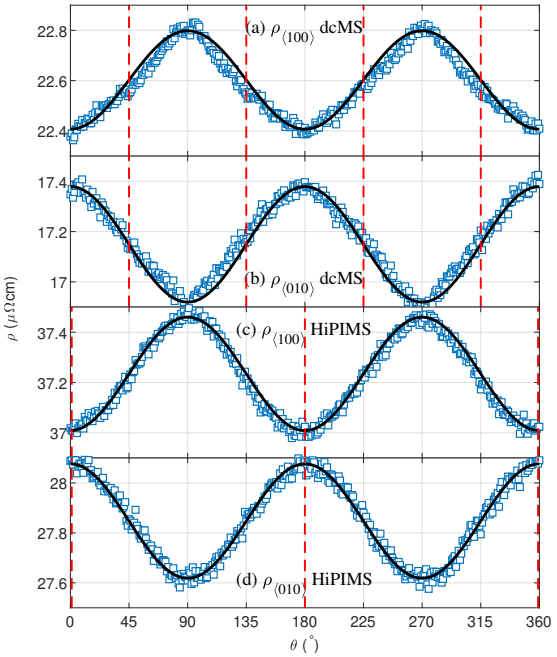

Figure 4.9. The AMR obtained by resistivity measurements along the [100] directions of Py films deposited by (a – b) dcMS and (c – d) HiPIMS during rotation of 24 Oe magnetic field. The θ here stands for angle of in-plane magnetization with the $\langle 100\rangle$ direction. The black lines indicate the result of fitting with Eq. (3.5). The vertical dashed lines indicate the direction of easy axes.

4.3 The origin of uniaxial anisotropy induced by tilt angle

Subsection 4.2.1 and 4.2.3 clearly showed that the difference between uniaxial and biaxial anisotropy of single crystal Py can be attributed to the different level of order. As mentioned earlier, the disordered structure is achieved by high deposition rate of HiPIMS during the pulse (>50 times of dcMS) which prohibit ordering. We believe, regardless of deposition technique, one can induce uniaxial anisotropy by any method if enough disorder is achieved.

Figure 4.10 compares (111) and (002) XRD peaks of a series of single crystal grown with tilt ($\angle$) and normal ($\perp$) deposition geometry. There is a clear shift of the (002) peak for the tilt deposited Py using HiPIMS while the (111) peak position is fixed. This is the only film that present uniaxial anisotropy due to their disordered structure. The rest of films present biaxial anisotropy and thus are ordered. In polycrystalline Py (002) peak gives a very weak intensity compared to strong (111) peak. Besides crystal defects and grain size will contribute to peak broadening. This makes detecting order/disorder via

XRD in the polycrystalline films very difficult. However, resistivity measurement is still a sensitive method to the variation of order which can be applied to the polycrystalline films.

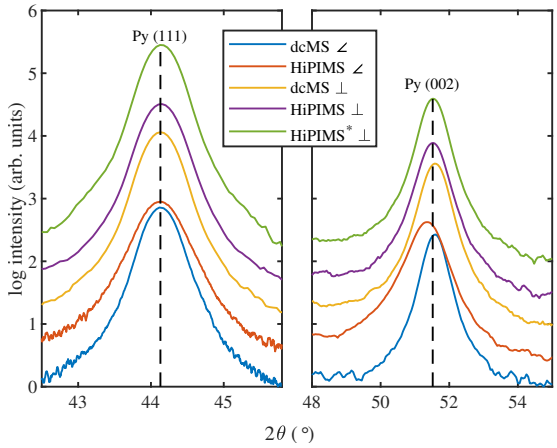

Figure 4.10. Single crystal Py (111) and (002) peaks obtained by dcMS and HiPIMS using tilt (∠) and normal (⊥) geometry. The vertical dashed lines indicate peak position for the bulk. All these sample grown at same power density of 1.91 W/cm^2 except HiPIMS* which is grown at 3 times larger power density.

Table 4.1 compares the results of the AMR measurement of polycrystalline Py films grown with the same thickness using normal deposition within *in-situ* magnetic field and tilt deposition with an identical assisting field. It can be seen that utilizing tilt deposition increases $\rho_{\parallel}$, $\rho_{\perp}$ and ρ_{ave} along both of the hard and easy axes. This is a signature of lower order in the Py film obtained by tilt deposition. In addition AMR value as well as $\Delta\rho$ are reduced by decrease in order.

Table 4.1. Resistivity measurements along hard and easy axes of 40 nm thick polycrystalline film grown by normal deposition within in-situ *magnetic field and tilt deposition with assisting field.*

inducing method	Current direction	$\rho_{\parallel}$	$\rho_{\perp}$	$\Delta\rho$ ($\mu\Omega$-cm)	ρ_{ave}	AMR (%)
field	easy	32.13	31.49	0.64	31.92	2.01
field	hard	31.53	30.97	0.60	31.37	1.90
field+tilt	easy	33.0161	32.4290	0.5871	32.6247	1.80
field+tilt	hard	33.4837	33.0139	0.4698	33.1705	1.42

4.4 Magnetic anisotropy in permalloy multilayers

The physical basis that underlies a preferred magnetic moment orientation in ultrathin magnetic films and multilayers can be quite different from the factors that account for the easy axis alignment along a symmetry direction of a bulk material, and the strength can also be markedly different (Johnson et al., 1996). The prominent presence of symmetry-breaking elements such as planar interfaces and surfaces, which automatically accompany the layered form of these systems, are the basic ingredients for this behaviour. By varying the thicknesses of the individual layers and choosing appropriate materials, it appeared possible to tailor the magnetic anisotropy. The most dramatic manifestation in this respect is the change of the preferential direction of the magnetization from the commonly observed in-plane orientation to the direction perpendicular to the plane. This phenomenon is usually referred to as *perpendicular magnetic anisotropy* and is particularly important for information storage and retrieval applications.

The perpendicular anisotropy is a result of a magnetic anisotropy at the interface which considerably differs from the magnetic anisotropy in the bulk. This type of magnetic anisotropy, a so-called interface or surface anisotropy, was predicted already by Néel (1954) to result from the lowered symmetry at the surface or interface. The first experiments which had revealed such an interface anisotropy were performed by Gradmann and Müller (1968) on ultrathin $Ni_{48}Fe_{52}$ films on Cu (111). In the following we probe anisotropy of Py/Pt multilayers on various effect such as substrate roughness and deposition of Py using dcMS and HiPIMS. We also substitute the Pt spacer with Cu and $Cu_{50}Pt_{50}$ to see effect of various strains on the magnetic anisotropy.

4.4.1 Strain and texture

Figure 4.11 shows the XRD pattern of Py/Pt multilyer deposited on the p-Si (001) with native oxide and 100 nm thermally grown oxide. The vertical dashed lines in black and red indicate (111) peak position for Pt (ICDD 00-001-1190) and Py (ICDD 01-071-8324), respectively, in the bulk state. It can be seen that a single (111) Py/Pt multilayer peak appears between pure Py and Pt peak position. This indicates all Py and Pt layers are under in-plane tensile and compressive strain, respectively. This is expected due to 10% lattice mismatch at interfaces that does not relax unless thickness of individual layer exceed a few nm. There are two satellite peaks indicated by -1 and -2 those distance is proportional to the multilayer period (Λ). It is worth mentioning that extracting period thickness from XRD at high angles might be tricky due to the fact that satellite peaks are caused by diffraction while XRR fringes are the result of interference as discussed by Pálsson et al. (2008). The asymmetry of satellite peaks intensities, e.g. $+1$ *vs.* -1, is a characteristic of strain normal to the film plane (Vartanyants et al., 2000). Here we do not observe clear positive satellite peaks that indicate huge strain normal to the film caused by in-plane epitaxial strains. This strain has been shown to be relaxed by precise annealing that makes satellite peaks more symmetric (den Broeder et al., 1988). The sharp peak at 69.9° is the Si (004) peak. The smaller sharp peak that sometimes appears at 34.6° belongs to Si (002) planes which is a forbidden peak but it some times appears as discussed by Zaumseil (2015). Due to the lack of Py/Pt (002) and (022) peaks, we conclude that these multilayers are holding a strong $\langle 111 \rangle$

texture normal to the substrate surface. It is also worth mentioning that the main (111) peaks in multilayers prepared by HiPIMS are slightly shifted towards smaller angles. We have already shown that for the case of single crystal Py, the (111) peak position does not change with the atomic order (cf. figure 4.10). Thus, we attribute this shift in multilayers prepared by HiPIMS to the different period than dcMS counterparts.

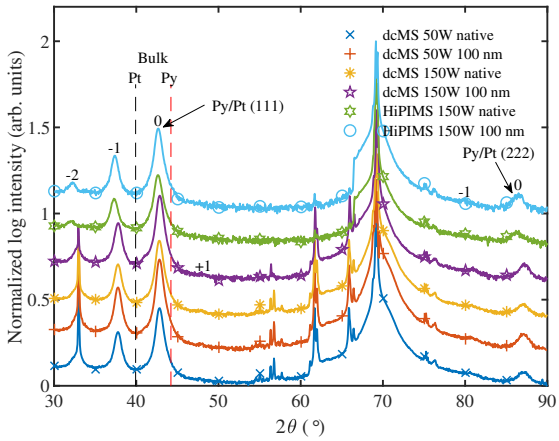

Figure 4.11. XRD patterns of Py/Pt multilayers deposited on p-Si (001) with native oxide and 100 nm thermally grown oxide. The legend indicates method and sputtering power utilized for Py deposition while Pt layers were deposited by dcMS at 20 W. The vertical dashed lines in black and red are indicating (111) peak position for the bulk Pt and Py, respectively.

4.4.2 Interface roughness and mixing

Figure 4.12 shows the XRR result of Py/Pt multilayer deposited by dcMS and HiPIMS on the p-Si (001) with native oxide and 100 nm thermally grown oxide. The values α, β and Λ indicated in the figure are inversely proportional to the total, Ta under-layer and period thicknesses, respectively. The Ta here act as a buffer layer to improve substrate roughness. It can be seen that the β fringes from Ta can be detected only utilizing a smooth substrate (100 nm oxide). While using native oxide, these fringes disappear due to huge roughness at the SiO_2/Ta interface. Using both substrates the period fringes can be detected which essentially means Ta can successfully improved surface roughness enough for growing delicate multilayers. For the HiPIMS case on the 100 nm oxide, the amplitude of α fringes decay much slower with the angle of incidence and they are visible up to $2\theta = 7.3°$. This essentially means HiPIMS gives smoother surface for the whole stack. However, to determine the roughness of the interfaces, the XRR result has to be fitted carefully. Furthermore, the XRR fit allows determining the thickness and density of the multilayers quantitatively. In general fitting XRR result of a multilayer is challenging compared to a system with a few layers. In practice, reducing computation cost includes assuming the periods are identical in thickness, roughness and density and constant period thickness. In our fitting we neglected the latter as the period thickness

might change due to the strain and interface mixing.

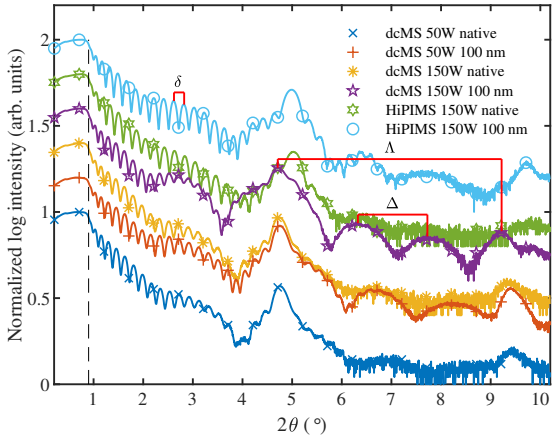

Figure 4.12. Comparison of Py/Pt multilayer deposited on p-Si (001) with native oxide and 100 nm thermally grown oxide. The legend indicates sputtering method and power utilized for Py while Pt layers deposited by dcMS at 20 W. The vertical dashed lines in black critical angle θ_c. δ, Δ and Λ are proportional to the total thickness, Ta under-layer thickness and repetition thickness, respectively.

Before discussing the result of fitting it is worth to briefly discuss its advantages for our purpose. It has been shown that XRR technique is a reliable method to study multilayers i.e. thickness and discontinuity of each layer as well as interface roughness (den Broeder et al., 1988; Chason and Mayer, 1997; Moreau-Luchaire, 2016; Azzawi et al., 2016). It is worth noting that the resolution of the XRR method including fitting process has been found to be ± 0.9 Å for the films with close mass density (Tiilikainen et al., 2007). While a huge difference in the density of Pt (21.45 g/cm^3) and Py (8.72 g/cm^3) multiples the resolution of measured thickness and roughness (Chason and Mayer, 1997; Tiilikainen et al., 2007). We would like to remark that the resolution of the interface roughness obtained by XRR is also dependent on the beam width. It has been shown that interface roughness obtained by XRR and high-resolution Rutherford backscattering spectroscopy (HRBS) are in good agreement for the beam width larger than 3.5 mm (Fujii et al., 2014). We used 7 mm beam width in our measurement to make sure we are probing large enough area for interface roughness. For the fist time, we use the mass density of each layer to determine the interface mixing. In accordance with the XRD results, Pt and Py are compressed and elongated in-plane, respectively. Thus for a pure Pt layer it is expected that its density becomes higher than 21.45 g/cm^3 while mixing with Py gives a density lower than this value. Using the same principle, we expect a density lower than 8.72 g/cm^3 for a pure Py layer and thus diffusion of Pt into it can be detected as increased density.

Table 4.2. Values of layers thickness (t), density (ρ) and surface roughness (R) obtained by fitting the XRR measurement results.

Growth method	Power (W)	substrate type	P (Pa)	t_{Py} (Å)	t_{Pt}	ρ_{Py} (g/cm^3)	ρ_{Pt}	R_{Py} (Å)	R_{Pt}
dcMS	50	Native	0.4	16.64	2.22	9.56	23.53	5.25	6.49
dcMS	50	100 nm	0.4	16.1	2.72	9.27	23.19	2.96	4.73
dcMS	50	100 nm	0.25	16.31	2.86	9.52	23.54	3.77	6.08
dcMS	150	Native	0.4	16.79	2.11	9.53	23.54	5.11	6.45
dcMS	150	100 nm	0.4	14.81	4	8.72	20.69	3.43	6.34
dcMS	150	100 nm	0.25	15.07	4	8.72	21.31	3.6	6.06
HiPIMS	150	Native	0.4	13.63	4.16	8.98	19.26	5.02	6.65
HiPIMS	150	100 nm	0.4	13.63	4.16	8.98	19.26	5.02	6.65
HiPIMS	150	100 nm	0.25	13.94	4	8.68	23.54	3.9	5.09

4.4.3 Magnetic behavior

Figure 4.13 shows the MOKE response of Py/Pt multilayers deposited on different substrate i.e. p-Si (001) with native oxide and a smooth 100 nm thermally grown oxide. Ohtani et al. (2013) reported that both (111) textured polycrystalline and (111) epitaxial Py present almost isotropic magnetization in the film plane. It has been shown that inducing uniaxial anisotropy using post-annealing in a magnetic filed (Chikazumi, 1956) or applying *in-situ* magnetic field during growth (Chikazumi, 1961) is easiest along the ⟨111⟩ and harder along the ⟨110⟩ and much harder along the ⟨100⟩ orientation. We have recently shown that the uniaxial anisotropy can be achieved even along the ⟨100⟩ orientation on the cost of lowering atomic order in the Py (Kateb et al., 2019d). It is worth mentioning that the low atomic order means low symmetry of Fe and Ni arrangement within crystal structure and not an amorphous or a polycrystalline microstructure. In tilt deposition geometry, the latter can be achieved using relatively high deposition rate or low substrate temperature those suppress adatom mobility and consequently high order. The MOKE results here indicate uniaxial anisotropy which is in agreement with our atomic order explanation since these multilayers were grown at room temperature (21 °C) (Kateb et al., 2019b).

For the 50 W dcMS shown in 4.13(a), the substrate with native oxide gives an open hard axis and a perfectly square easy axis while utilizing a smooth 100 nm oxide substrate, enhances the hard axis and presents perfectly linear hard axis. In the 150 W dcMS, as shown in figure 4.13(b), both substrates result in very well-defined hard and easy axes. Utilizing a smooth (100 nm) substrate in this case enhances H_k but it also gives a small hysteresis in the middle of the hard axis. The latter can be separated from the hard axis loop as a change of the slope around ±4 Oe. Such behavior is expected in the multilayers with even number of magnetic layers (Parkin et al., 1991) as reported for Co/Ru (Parkin et al., 1990), Fe/Cr (Parkin et al., 1991), Co/Nb, Co/Mo and Co/Ta (Parkin, 1991) due to the antiferromagnetic exchange coupling. It has been already shown that antiferromagnetic exchange coupling is reduced upon intermixing between magnetic and spacer layer (Azzawi et al., 2017). Thus we expect sharper interface for

the multilayer deposited by 150 W dcMS.

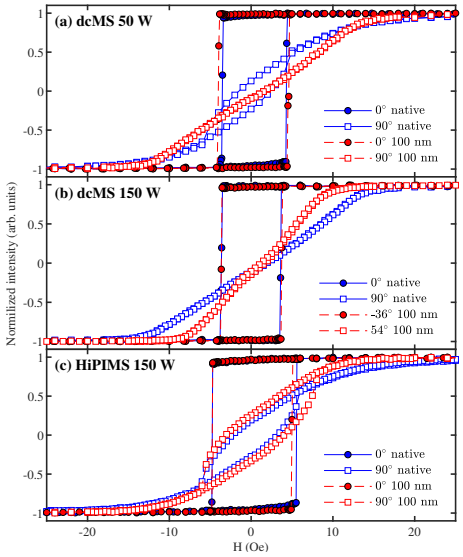

Figure 4.13. The MOKE response of Py/Pt multilayer deposited on the p-Si (001) with native oxide and 100 nm thermally grown oxide. The legend indicates sputtering method and power utilized for Py deposition while the Pt layers were deposited by dcMS at 20 W.

Figure 4.13(c) shows the HiPIMS case which gives an open hard axis and square easy axis regardless of the substrate smoothness. The coercivity in this case is slightly higher than values observed for both of the dcMS counterparts. It has been shown that alloying Py with Pt can cause increase in both coercivity and anisotropy field (Chen et al., 1991). This is not the case here since we already showed that fitting XRR results indicate minimum alloying for multilayers prepared by HiPIMS compared to their counterparts on the same substrate. Thus, high epitaxial strain due to sharp interfaces is responsible for increased coercivity and opening in the hard axis. This strain is relaxed in the dcMS counterparts mainly by e.g. diffusion of Pt with larger atomic radius into stretched Py or *vice versa*. The opening in the hard axis can be attributed to the perpendicular anisotropy as predicted by Hirayama et al. (2017) for Py thicknesses below 2 nm.

4.4.4 The interplay between intermixing and magnetic property

Furthermore we studied the effect of strain by substituting Pt with Cu and $Cu_{50}Pt_{50}$ at. %. Cu has a lattice constant of 3.61 Å close to that of Py (3.54 Å) while Pt has much larger lattice constant of 3.92 Å. Figure 4.14 shows the MOKE response of Py/(Cu, CuPt and Pt) multilayers deposited on substrate with 100 nm oxide. The entire samples were grown using HiPIMS to be identical from viewpoint of intermixing at interfaces. It can be seen that for the Py/Cu very soft but also vey well-defined uniaxial anisotropy is

obtained. However, as the lattice constant increases the increase in strain at the interface results in higher coercivity and open hard axis. This is clear evidence of importance of strain in the ultrathin Py.

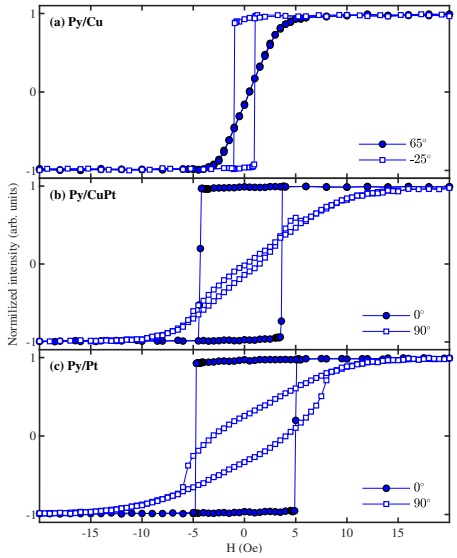

Figure 4.14. The MOKE response of Py/(Cu, CuPt and Pt) multilayer deposited at 0.25/0.4 Pa on p-Si (001) substrate with a smooth 100 nm thermally grown oxide. In all cases Py layers has been deposited by HiPIMS while spacer layers were deposited by dcMS.

5 Summary and conclusion

It has been shown that the mechanism of uniaxial anisotropy induced by tilt deposition can be explained by atomic order rather than self-shadowing and off-normal texture. In particular we grew films exhibiting 2 Å surface roughness with $\langle 111 \rangle$ texture normal to the film plane which present very well-defined uniaxial anisotropy. Furthermore, it is shown that using tilt deposition geometry, uniaxial anisotropy can be achieved along the $\langle 100 \rangle$ orientation of single crystal Py. In order to do so, one has to utilize HiPIMS (with high instantaneous deposition rate during the pulse) or low temperature dcMS to induce disorder in the film. However, using dcMS at e.g. room temperature may not leads to desired crystal quality. Previously, it has been shown that post-annealing and *in-situ* magnetic field failed to induce uniaxial anisotropy along the [100] directions. In the former, annealing does not provide enough diffusion to lead to a disorder. In the latter, higher order is achieved probably due to the fact that very low deposition rate is used to grow single crystal Py. In both cases, however, uniaxial anisotropy was obtained easier along the [111] orientations. We conclude that in an ordered Py, magnetocrystalline effect is much stronger than magnetostrction due to the magnetic field. Thus, magnetic field is only efficient when it is applied along the [111] directions i.e. the magnetocrystalline anisotropy axes. However, it cannot reorient the easy axis towards [100] orientations due to relatively strong spin–orbit coupling. To overcome this we suggest breaking the symmetry of ordered Py.

Using XRD, we have detected single (111) multilayer peak in Py/Pt multilayers instead of separate peaks for Py and Pt. Besides, the satellite peaks were asymmetric. These indicate that the Py/Pt is fully strained and strongly textured. When we succeed to make a multilayer with minimum interface mixing, using HiPIMS, the magnetic properties are drastically changed. This include increased H_c along the easy axis and an opening in the hard axis loop. We attributed this change to the stress created at the interface due to lattice mismatch between Py and Pt. This stress is maximizes at a sharp interface and relaxes by inter-diffusion.

6 Summary of papers

Paper I

Thickness-dependent magnetic and magnetoresistance properties of permalloy prepared by field assisted tilt sputtering

M. Kateb and S. Ingvarsson 2017
2017 IEEE Sensors Applications Symposium (SAS) 1–5

This full text paper was peer-reviewed at the direction of IEEE Instrumentation and Measurement Society prior to the acceptance and publication.

Thickness-dependent Magnetic and Magnetoresistance Properties of Permalloy Prepared by Field Assisted Tilt Sputtering

Movaffaq Kateb and Snorri Ingvarsson*
Science Institute
University of Iceland
IS-107 Reykjavik, Iceland
Emails: mkk4@hi.is, *sthi@hi.is

***Abstract*—This paper presents magnetic and anisotropic magnetoresistance (AMR) results of permalloy $Ni_{80}Fe_{20}$ films of different thickness (10-250 nm). The films were grown by sputter deposition at an angle, with *in-situ* magnetic field assisting the definition of uniaxial anisotropy. The results show that there is negligible change in anisotropy field (H_k) and resistivity with thickness down to 50 nm. However, for thinner films (<50 nm) H_k and resistivity increase rapidly with decrease in film thickness. The coercivity (H_c) of our films was found to be independent of the thickness, in all cases below 1.5 Oe. The AMR increases with the film thickness and saturates at higher thicknesses.**

I. Introduction

Anisotropic magnetoresistance (AMR) is observed as a variation in resistance by changing the relative alignment of current and magnetization directions. This effect is found in ferromagnets and utilized in practical applications such as magnetic field sensors and digital recording in the form of thin films [1]. Recently, it was shown that AMR sensors demonstrate ultra sensitive detection of small magnetic fields down to the 1 nT range [2]. However further improvement of the current sensors is challenged by the relatively low AMR ratio and "high" H_k of permalloy films at low thicknesses. From an engineering point of view it is of interest to have smaller thickness, low H_k, and large AMR simultaneously. However, the general trend is quite the opposite, as device thickness scales down, H_k increases and AMR drops rapidly.

The above mentioned properties are highly dependent on the sample preparation method [1] e.g. magnetization during growth. The control over magnetization direction can be achieved either by applying *in-situ* magnetic field during growth or by depositing under an angle with respect to the substrate [3]. The origin of induced anisotropy by applying magnetic field is not fully understood; but, the tilt angle has been found to be associate with self-shadowing [3]. To our knowledge there is no solid evidence for contribution of crystallographic origin, such as defect alignment or elongated crystallites to the magnetization in permalloy.

In the present study, we used both *in-situ* magnetic field and tilt deposition in the film preparation. We investigated which of the effects is the more dominant in our case, and how to grow films with low magnetic anisotropy. We grew films with a series of thicknesses hoping to optimize anisotropy and AMR for sensor application.

II. Method

The permalloy films were grown on the 100 nm thick thermally grown oxide on (100) p-Si without any buffer or seed layer. We would like to remark that we grew permalloy films both on tilt deposited Ta and AlZr seed layers. In both cases this resulted in increased H_k in comparison with permalloy without a seed layer, which is in agreement with previous results [4][5]. UHV magnetron sputtering with the base pressure $< 5 \times 10^{-9}$ mbar and process pressure (Ar-gas) of 1.3×10^{-3} mbar at 150 W power which resulted in 1.2 Å/s deposition rate. To hold the induced anisotropy of tilt angle and have uniform thickness, the sample holder was rotated back and forth by 360° at $\sim$12.8 rpm with 200 ms stop during reversal as is schematically shown in figure 1. This results in the hard axis lying in the plane of incidence while the easy axis is in the perpendicular direction as indicated by blue and red arrows in the figure 1. Thus, the presence of *in-situ* field of $\sim$70 Oe parallel to easy axis translated to assisting tilt angle (shown in the figure 1) while placing the magnets along the other edges of the sample has the applied field competing with the tilt in defining the sample's easy axis.

To ensure thickness uniformity, we lithographically defined a few lines from side to side and corner to corner of the samples, resulting in steps whose height we measured by AFM. Further material characterization was done using Panalytical high resolution XRD. We measure magnetic hysteresis loops with our home made magneto optical Kerr effect (MOKE) setup, with high sensitivity to in-plane rotation. The H_c was read directly from easy axis loop and the anisotropy field H_k was obtained by extrapolating low field behavior to the saturation level in hard axis magnetisation traces. The latter is a conventional method for extraction H_k with a linear hard axis trace with no opening. The resistance measurements were done at room temperature by the Van der Pauw (vdP) [6] method, and applying the Price [7] extension for anisotropic media. The vdP measurements were repeated for magnetoresistance

978-1-5090-3202-0/17/$31.00 ©2017 IEEE

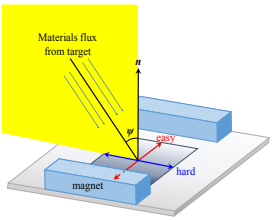

Fig. 1. Schematic illustration of deposition geometry and tilt angle induced hard and easy axis

at ∼23 Oe in-plane saturation fields parallel and perpendicular to the easy axis direction.

III. Result and discussion

A. Tilt vs applied field during deposition

Figure 2 presents a comparison of hysteresis loops obtained from samples grown without field and with field in parallel and perpendicular directions to tilt angle. It can be seen that tilt without field present the lowest H_c and a hard axis magnetisation trace with a slight opening at low fields. By applying magnetic field that competes with the deposition angle the opening in the hard axis trace is enhanced, without visible change in H_k (shown figure 2B). However, the H_c increases and the easy axis magnetisation loop is slightly rounded as indicated by black arrow in figure 2A. On the other hand, the assisting field gives intermediate H_c with a very well defined sharp magnetisation transition as shown in figure 2A, which is of prime importance to retain digital information in magnetic recording or magnetic memories. In addition, it exhibits a linear hard axis trace without hysteresis (see figure 2B), which is desirable from the perspective of the field sensors. The figure 2A shows assisting field presents a slightly higher H_k. Thus, the assisting field configuration is preferred for further studies. It is worth noting that tilt angle wins over the *in-situ* applied field even if it the sample rotates during deposition and stops for only very short time while reversing rotation direction.

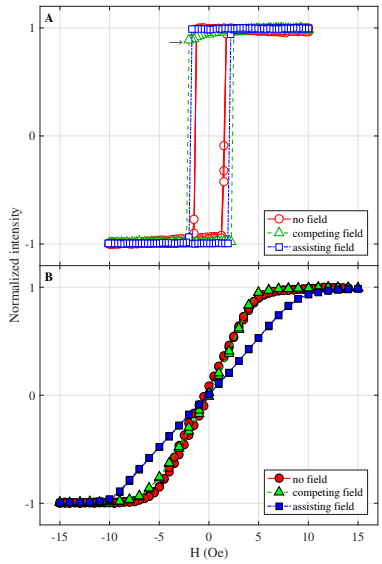

Fig. 2. MOKE hysteresis loops for (A) easy and (B) hard axis of 30 nm films grown without field and with field assisting and competing tilt angle. The samples were grown with the exact same thickness and condition described in method but at 5.3×10^{-3} mbar.

B. Microstructure

The thickness, density and roughness of the films were obtained by fitting x-ray reflectivity (XRR) curves (not shown here). The thicknesses of the samples indicate a stable growth rate of precisely 1.2 Å/s. The densities of the films shows very slight deviation from the average of 8.62 g/cm^3. The deviation becomes smaller and converges at higher thicknesses since there is more materials to be exposed by x-ray and more fringes to fit. The surface of the films present excellent smoothness, with x-ray results showing about ∼2 Å roughness. For a few samples the roughnesses was verified by AFM, which gave results in the range 1.9-2.8 Å. Thus, there is slight difference in the roughness obtained in XRR fit and AFM. Controling roughness is very important with respect to magnetic and transport properties of thin films. For instance, a 30 nm permalloy film grown at 5.3×10^{-3} mbar presents higher roughness and H_k of ∼10 Oe (assisting field in figure 2) compared to film of the same thickness grown at 1.3×10^{-3} mbar with H_k of 4 Oe (see figure 4).

Figure 3 shows the grazing incidence x-ray diffraction (GIXRD) pattern of the films which is a common technique in thin film characterization. For the 10 nm thick sample the only detectable peak is (111) at 44.2 ° while thicker films also present (200) and (220) peaks at 58.2 and 75 °, respectively [8]. The increase in the (111) peak height with thickness indicates an enhancement in crystallinity. A more quantitative value of crystallinity is the grain size. It is worth noting that GIXRD pattern gives the grain size estimation parallel to the substrate (in-plane). The estimated grain size from the Scherrer formula is shown by red circles in the figure inset. At higher

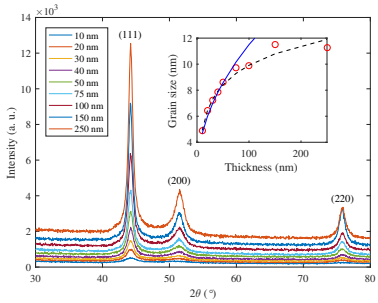

Fig. 3. GIXRD pattern of NiFe with different thicknesses. The inset shows estimated grain size (red circles) from Scherer formula compared with square-root (solid blue) and natural logarithm (dashed black) dependency to thickness.

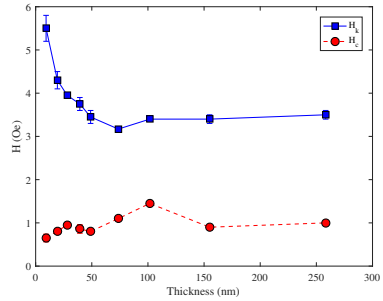

Fig. 4. Variation of H_k and H_c with the film thickness

thicknesses, the grain size deviates from the typical square root dependency as shown by the blue line. Transmission electron microscope imaging has revealed that grain boundary pinning by voids limits normal grain growth in sputtered permalloy films [9]. The dashed line shows natural logarithm which presents the best mathematical fit for the permalloy films.

It is worth noting that our 150 nm thick sample presents the largest estimated grain size. In addition the (220) peak of this sample is higher than the rest of the films considering the background intensity. There is no specific behaviour for (200) peaks and its height grows linearly with the film thickness. This indicates competition between $\langle 111 \rangle$ and $\langle 200 \rangle$ texture normal to substrate which is characteristic of tilt sputtering [10].

C. Magnetic properties

Figure 4 shows how both H_k and H_c depend on thickness in our films. The H_k shows a very sharp increase with decrease in thickness below 50 nm, while it seems to be saturated at around ∼3.4 Oe for thicknesses higher than 50 nm. On the other hand H_c show no thickness dependence except for two apparent maxima at 30 and 100 nm, respectively. The relation of H_c with thickness and grain size is still unclear. However, the plot can be associated with change in domain walls structure i.e. a transition from Néel to Bloch walls and consequently the coercive force exerted from domain walls might change. The similar trend for H_c has been reported previously [11]. It is worth noting that the H_c of all of our films here stand below 1.4 Oe which is lower than 2.5 Oe obtained in our previous study for permalloy sandwiched between Ta [12].

D. Magnetroresistance

1) Resistivity: The Van der Pauw, vdP, method is a very useful technique to probe resistivity of uniform, continuous thin films of arbitrary shape [6]. We choose to work with square samples, with electrical contacts at each of the four corners labeled A, B, C, and D. The "isotropic resistivity" value, ρ_{iso} is obtained by the vdP formula:

$$\exp\left(-\frac{\pi t}{\rho_{iso}} R_{AB,CD}\right) + \exp\left(-\frac{\pi t}{\rho_{iso}} R_{BC,DA}\right) = 1 \quad (1)$$

where t is the film thickness. R is resistance e.g. by applying current to BC and picking up the voltage on parallel side of DA or *vice versa*. It has been shown that $\rho_{iso} = \sqrt{\rho_x \rho_y}$ is the geometric mean of principle resistivities i.e. along easy (ρ_x) and hard (ρ_y) axes in our case [6], [7].

The ρ_x and ρ_y can be obtained from Price's [7] extension to the vdP method for anisotropic samples, as below:

$$\sqrt{\frac{\rho_x}{\rho_y}} = -\frac{b}{\pi a} \ln\left(\tanh\left[\frac{\pi t R_{BC,DA}}{16 \rho_{iso}}\right]\right) \quad (2)$$

where b and a are the sides of a rectangular sample and $R_{BC,DA}$ is resistance along the b sides as described above. Eq. 2 yields the ratio of easy and hard axis resistivity. The individual values of principle resistivities can subsequently be obtained by:

$$\rho_x = \rho_{iso} \sqrt{\frac{\rho_x}{\rho_y}} \quad (3)$$

$$\rho_y = \rho_{iso} \left(\sqrt{\frac{\rho_x}{\rho_y}}\right)^{-1} . \quad (4)$$

The ρ_{ave} for fcc materials like permalloy is described by [1]:

$$\rho_{ave} = \frac{1}{3}\rho_{\parallel} + \frac{2}{3}\rho_{\perp} \quad (5)$$

where $\rho_{\parallel}$ and $\rho_{\perp}$, respectively, are resistivities with magnetization parallel and perpendicular to the current direction. Thus, either ρ_x or ρ_y can be translated to $\rho_{\parallel}$ and $\rho_{\perp}$ by applying proper external magnetic field.

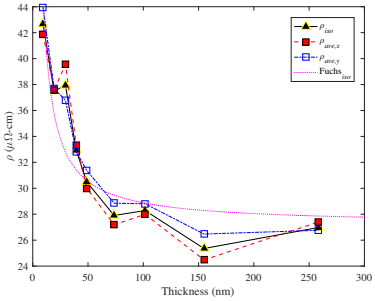

Fig. 5. Variation of the ρ_{iso} with the film thickness. The ρ_{ave} along hard and easy axis and Fuchs model plotted for comparison.

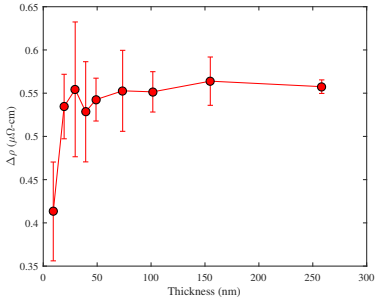

Fig. 6. The change in $\Delta\rho$ with the film thickness

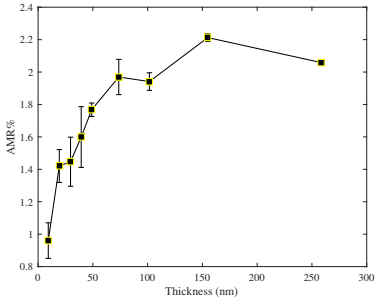

Fig. 7. Variation of AMR% with the film thickness

Figure 5 shows variation of different resistivities with the film thickness. It can be seen that for all data points ρ_{iso} stand between ρ_{ave} and there is clear increase with decrease in thickness for them. Fitting ρ_{iso} data points by the Fuchs-Sondheimer model [13] gives a bulk resistivity of 27 $\mu\Omega$ cm which is somewhat higher than e.g. the bulk value of 14 $\mu\Omega$ cm published by McGuire and Potter [1]. This difference might be due to the assumptions of the Fuchs-Sondheimer model which only considers surface/interface scattering, that unrealistic for polycrystalline films such as ours [14]. A later model by Mayadas and Shatzkes (not shown here) took grain boundaries into consideration, but is only applicable to annealed films [15]. To our knowledge there is lack of a comprehensive model to describe thickness dependence of as prepared films grown at room temperature that have grain size much smaller than their thickness. This is even true for very thin films since contribution of surface and grain boundaries is the same.

2) AMR: The AMR ratio is given by [1]

$$AMR = \frac{\Delta\rho}{\rho_{ave}} = \frac{\rho_{\perp} - \rho_{\parallel}}{\rho_{ave}} \tag{6}$$

Figure 6 presents the change in $\Delta\rho$ with the film thickness. It can be seen that the data points agree, within error, at 0.55 $\mu\Omega$ cm, except for the thinnest film. It must seem likely that this is a start of a real drop in $\Delta\rho$, as the AMR drops steadily as well as seen in Fig. 7. The result of McGuire and Potter [1] fit in the present range. They concluded $\Delta\rho$ is independent of thickness. However, Williams *et al.* [16] reported very strong increase in $\Delta\rho$ with film thickness which is in disagreement with the present result. Funaki *et al.* [17] reported an increase in $\Delta\rho$ with a maxima at ∼75 nm followed by slight decrease at 100 nm for their as grown sample. Thus there are conflicting results on the thickness dependence of $\Delta\rho$.

Figure 7 presents AMR in percent as function of film thickness. The AMR increases with film thickness and levels off around 2.1%. This in agreement with the results of Funaki *et al.* [17] and McGuire and Potter [1]. However the AMR result of Williams *et al.* [16] show linear increase without saturation which is due to the behaviour of their $\Delta\rho$ as discussed above.

The present results of $\Delta\rho$ and AMR are in good agreement with Funaki *et al.* [17] and McGuire and Potter [1] who prepared films by sputtering at room temperature on SiO_2/Si. However, Williams *et al.* [16] used glass as a substrate and grew their samples at 300 °C by thermal evaporation. It appears that the saturation behaviour in $\Delta\rho$ and AMR is very sensitive to sample preparation conditions. We would like to remark that high $\Delta\rho$ and AMR at high thickness is not the aim of current study.

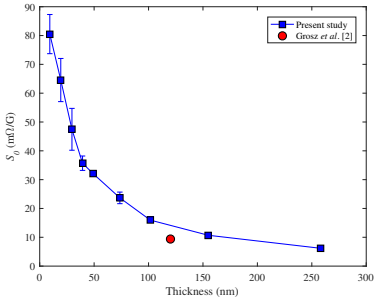

Fig. 8. Variation of S_0 with the film thickness. The red circle indicated claculated value from [2]

3) Sensitivity: The sensitivity of sensor (S_0) independent of applied parameters can be expressed as [2], [18]:

$$S_0 = \frac{\Delta\rho}{tH_k} \tag{7}$$

Figure 8 presents the calculated value of S_0 for different thicknesses. The error bar plotted considering uncertainties in H_k and $\Delta\rho$. It can be seen that the S_0 increase rapidly with decrease in film thickness. The plot also shows the S_0 calculated for a nT resolution sensor [2] by red circle. We would like to remark that there are several parameters like applied current, and frequency that contribute to sensor resolution in addition to S_0.

IV. Conclusion

In conclusion, variation of microstructure, magnetic and AMR with the thickness of permalloy films was studied. The films were grown at room temperature with a small in-situ magnetic field applied to assist easy axis definition induced by deposition under an angle. It is found that this results in excellent uniaxial anisotropy i.e. linear hard axis without hysteresis and very sharp magnetization transition along the easy axis. Our films present strong (111) texture and the grain size increases with the film thickness. The resistance of the films decreases rapidly with the film thickness till 75 nm and decrease slightly afterwards. The H_k increase rapidly with decrease in thickness below 50 nm; but the change is negligible for thicker films. It is shown that H_c is independent of the film thickness and probably depends on the domain wall structure. The AMR results show an increase and then saturation behaviour with the film thickness which strongly depend on the saturation trend obtained in $\Delta\rho$ while the later seems to be affected by preparation method.

Acknowledgment

This work was supported by The Icelandic Research Fund Grant No. 120002023.

References

[1] T. McGuire and R. Potter, "Anisotropic magnetoresistance in ferromagnetic 3d alloys," *IEEE Transactions on Magnetics*, vol. 11, no. 4, pp. 1018–1038, 1975.

[2] A. Grosz, V. Mor, E. Paperno, S. Amrusi, I. Faivinov, M. Schultz, and L. Klein, "Planar hall effect sensors with subnanotesla resolution," *IEEE Magnetics Letters*, vol. 4, pp. 6 500 104–6 500 104, 2013.

[3] D. O. Smith, "Anisotropy in permalloy films," *Journal of Applied Physics*, vol. 30, no. 4, pp. S264–S265, 1959. [Online]. Available: http://scitation.aip.org/content/aip/journal/jap/30/4/10.1063/1.2185921

[4] R. D. McMichael, C. G. Lee, J. E. Bonevich, P. J. Chen, W. Miller, and W. F. Egelhoff, "Strong anisotropy in thin magnetic films deposited on obliquely sputtered Ta underlayers," *Journal of Applied Physics*, vol. 88, no. 9, pp. 5296–5299, 2000. [Online]. Available: http://scitation.aip.org/content/aip/journal/jap/88/9/10.1063/1.1323436

[5] X. Li, X. Sun, J. Wang, and Q. Liu, "Magnetic properties of permalloy films with different thicknesses deposited onto obliquely sputtered Cu underlayers," *Journal of Magnetism and Magnetic Materials*, vol. 377, pp. 142–146, 2015.

[6] L. Van der Pauw, "A method of measuring specific resistivity and hall effect of discs of arbitrary shape," *Philips Research Reports*, vol. 13, no. 1, pp. 1–9, 1958.

[7] W. Price, "Electric potential and current distribution in a rectangular sample of anisotropic material with application to the measurement of the principal resistivities by an extension of van der Pauw's method," *Solid-State Electronics*, vol. 16, no. 7, pp. 753–762, 1973.

[8] A. Dzhumaliev, Y. V. Nikulin, and Y. A. Filimonov, "Deposition of NiFe (200) and NiFe (111) textured films onto Si/SiO_2 substrates by DC magnetron sputtering," *Physics of the Solid State*, vol. 58, no. 5, pp. 1053–1057, 2016.

[9] D. G. Neerinck, A. E. M. De Veirman, M. H. J. Slangen, T. G. S. M. Rijks, and J. C. S. Kools, "Grain size and strain in thin sputter-deposited $Ni_{0.8}Fe_{0.2}$ and Cu films," *Thin Solid Films*, vol. 280, no. 1, pp. 136–141, 1996. [Online]. Available: http://www.sciencedirect.com/science/article/pii/0040609095082441

[10] S. Mahieu, P. Ghekiere, D. Depla, and R. De Gryse, "Biaxial alignment in sputter deposited thin films," *Thin Solid Films*, vol. 515, no. 4, pp. 1229–1249, 2006.

[11] T. Miyazaki, T. Ajima, and F. Sato, "Dependence of magnetoresistance on thickness and substrate temperature for 82Ni-Fe alloy film," *Journal of magnetism and magnetic materials*, vol. 81, no. 1-2, pp. 86–90, 1989.

[12] S. Ingvarsson, G. Xiao, S. Parkin, and W. Gallagher, "Thickness-dependent magnetic properties of $Ni_{81}Fe_{19}$, $Co_{90}Fe_{10}$ and $Ni_{65}Fe_{15}Co_{20}$ thin films," *Journal of magnetism and magnetic materials*, vol. 251, no. 2, pp. 202–206, 2002.

[13] K. Fuchs, "The conductivity of thin metallic films according to the electron theory of metals," in *Mathematical Proceedings of the Cambridge Philosophical Society*, vol. 34. Cambridge Univ Press, 1938, Conference Proceedings, pp. 100–108.

[14] A. F. Mayadas, J. F. Janak, and A. Gangulee, "Resistivity of permalloy thin films," *Journal of Applied Physics*, vol. 45, no. 6, pp. 2780–2781, 1974. [Online]. Available: http://scitation.aip.org/content/aip/journal/jap/45/6/10.1063/1.1663668

[15] A. Mayadas and M. Shatzkes, "Electrical-resistivity model for polycrystalline films: the case of arbitrary reflection at external surfaces," *Physical review B*, vol. 1, no. 4, p. 1382, 1970.

[16] F. C. Williams Jr and E. Mitchell, "A study of resistance and magnetoresistance in nickel-iron thin films," *Japanese Journal of Applied Physics*, vol. 7, no. 7, p. 739, 1968.

[17] H. Funaki, S. Okamoto, O. Kitakami, and Y. Shimada, "Improvement in magnetoresistance of very thin permalloy films by post-annealing," *Japanese journal of applied physics*, vol. 33, no. 9B, p. L1304, 1994.

[18] L. W. Ejsing, "Planar hall sensor for influenza immunoassay," Ph.D. dissertation, MIC-Department of Micro and Nanotechnology, Technical University of Denmark, 2006.

Paper II

Comparison of magnetic and structural properties of permalloy $Ni_{80}Fe_{20}$ grown by dc and high power impulse magnetron sputtering

M. Kateb, H. Hajihoseini, J. T. Gudmundsson and S. Ingvarsson 2017
Journal of Physics D: Applied Physics 51 (28) 2018, 285005 (8pp)

IOP Publishing Journal of Physics D: Applied Physics
J. Phys. D: Appl. Phys. **51** (2018) 285005 (8pp) https://doi.org/10.1088/1361-6463/aaca11

Comparison of magnetic and structural properties of permalloy $Ni_{80}Fe_{20}$ grown by dc and high power impulse magnetron sputtering

Movaffaq Kateb[1], Hamidreza Hajihoseini[1,2], Jon Tomas Gudmundsson[1,2] and Snorri Ingvarsson[1]

[1] Science Institute, University of Iceland, Dunhaga 3, IS-107 Reykjavik, Iceland
[2] Department of Space and Plasma Physics, School of Electrical Engineering and Computer Science, KTH–Royal Institute of Technology, SE-100 44, Stockholm, Sweden

E-mail: sthi@hi.is

Received 10 April 2018, revised 23 May 2018
Accepted for publication 4 June 2018
Published 25 June 2018

Abstract

We study the microstructure and magnetic properties of $Ni_{80}Fe_{20}$ thin films grown by high power impulse magnetron sputtering (HiPIMS), and compare with films grown by dc magnetron sputtering (dcMS). The films were grown under a tilt angle of 35° to identical thickness of 37 nm using both techniques, at different pressure (0.13–0.73 Pa) and substrate temperature (room temperature and 100 °C). All of our films display effective in-plane uniaxial anisotropy with square easy axis and linear hard axis magnetization traces. X-ray diffraction reveals that there is very little change in grain size within the pressure and temperature ranges explored. However, variations in film density, obtained by x-ray reflectivity measurements, with pressure have a significant effect on magnetic properties such as anisotropy field (H_k) and coercivity (H_c). Depositions where adatom energy is high produce dense films, while low adatom energy results in void-rich films with higher H_k and H_c. The latter applies to our dcMS deposited films at room temperature and high pressure. However, the HiPIMS deposition method gives higher adatom energy than the dcMS and results in dense films with low H_k and H_c. The surface roughness is found to increase with increased pressure, in all cases, however it showed negligible contribution to the increase in H_k and H_c.

Keywords: permalloy $Ni_{80}Fe_{20}$, HiPIMS, magnetic, uniaxial anisotropy, microstructure, pressure, substrate temperature

(Some figures may appear in colour only in the online journal)

1. Introduction

Permalloy $Ni_{80}Fe_{20}$, referred to as Py hereafter, is a very well known ferromagnetic material and has over the years been used extensively in various industrial applications. In its thin film form it presents a (surprisingly) low in-plane easy-axis-like anisotropy caused by competing contributions from Ni and Fe. A further benefit is its vanishing magnetostriciton. It has been employed in many applications, such as anisotropic magnetoresistance (AMR) and planar Hall effect (PHE) field sensors [1], magnetic recording heads [2–5] and magnetoresistive random access memory (MRAM) [6, 7]. Thin permalloy films have been deposited by thermal evaporation [8, 9], electroplating [10–12], electron beam deposition [13], rf diode sputtering [14–16], dc magnetron sputtering (dcMS) [16–18] and rf magnetron sputtering [19]. It is well known that the electrical and magnetic properties are influenced by the deposition conditions and method [14, 15]. We have recently shown that a tilt deposition geometry with respect to the substrate normal using dcMS induces strong in-plane uniaxial anisotropy, i.e.

a square easy axis with sharp transitions and a linear hard axis without hysteresis [20, 21]. Those are desirable properties for both magnetic memories and field sensors. However, tilt sputtering at high pressures, which is more appropriate for large industrial applications, has not been studied yet. This is mainly because tilt deposition requires low pressure as it suffers from scattering of the sputtered flux by the working gas at high pressures [22]. There is also a competition between in-plane and out-of-plane anisotropy in Py films. It has been shown that for both dcMS and evaporation, increased pressure reduces in-plane uniaxial anisotropy accompanied with losing magnetic softness [9, 18, 23]. Regardless of the deposition method, the poor in-plane anisotropy was associated with formation of stripe domains at thicknesses beyond the critical thickness. The critical thickness decreases dramatically with increased pressure [9, 18, 23], e.g. it is about 250 nm at 0.38 Pa and decreases to 60 nm at 2.4 Pa using dcMS deposition [18]. Since, higher pressure increases surface roughness and encourages void-rich structure in the case of Py [24], a decrease in the critical thickness was attributed to an increase in the surface roughness [18] and increase in defects and voids [9, 23] with increased pressure.

An interesting solution to overcome void-rich structure and rough surface is offered by high power impulse magnetron sputtering (HiPIMS) which is an ionized physical vapor deposition technique that has attracted much interest lately [25, 26]. By pulsing the target to a high power density with unipolar voltage pulses, low duty cycle, and low repetition frequency, high electron density is achieved in the plasma [25, 26]. This high electron density leads to a high ionization fraction of the sputtered material. As a result HiPIMS presents denser [27–29], void free [30] and smoother coatings [28, 30, 31] compared to conventional sputtering methods. It has been shown that amorphous magnetic films of $Fe_{73.5}CuNb_3Si_{15.3}B_7$ can be grown by HiPIMS and they are claimed to have the same composition as the target over wide range of pressures [32]. This is important since dcMS has been found to present 2.3 *at*.% change in iron content of Py by changing the pressure in the 0.38–2.4 Pa range [18] which can have significant effect on the magnetic properties, as discussed e.g. by O'Handley (see [33], pages 190 and 369). It has also been shown that the coercivity (H_c) of the films grown by HiPIMS increases with increased pressure in the 1.33–8.00 Pa range [34]. However, in later studies [32, 34] the same authors compared magnetic softness of various films grown at different pressures but with *different thickness*. They also did not explore the variation of surface roughness and film density at different pressures and their effect on the magnetic properties. Thus the effect of pressure change on the microstructure as well as magnetic properties of films grown by HiPIMS are not well understood, and in particular the role of film density and surface roughness.

Here, we study the properties of Py films grown by HiPIMS at different pressures while maintaining the same thickness and compare with dcMS grown films under similar conditions. The main focus is on studying deposition at increased pressure and finding under which conditions we are able to maintain high quality magnetic films, with well defined square hysteresis loops and low coercivity and anisotropy field using dcMS and HiPIMS deposition, respectively.

2. Experimental apparatus and method

The substrates were square $10 \times 10\,\text{mm}^2$ p-Si(0 0 1) with a native oxide of about 2.4 nm thickness. The Py thin films were grown in a custom built UHV magnetron sputtering chamber with a base pressure less than 5×10^{-7} Pa. The deposition was done with argon of 99.999 % purity as the working gas using a $Ni_{80}Fe_{20}$ at.% target with 75 mm diameter. The substrate was kept at room temperature (21 ± 0.1 °C) and 100 °C during growth, respectively.

In order to ensure as uniform film thickness as possible, we rotate the sample 360° in one direction and then stop (due to electrical wiring to the sample holder) and then rotate it back by 360° in the reverse direction. The rotation is at ∼12.8 rpm with 300 ms stop time at the turning points. The deposition is done under an angle of 35° with respect to the substrate, the stop-and-turn position plays an important role in defining magnetization axis direction [20]. In short, tilt angle induces hard magnetization axis along the plane of incidence and easy magnetization axis perpendicular to that. We have already shown that the tilt deposition can have a stronger effect on magnetization direction than the applied magnetic field during growth. Further details on sample growth and a schematic of our deposition geometry can be found elsewhere [20].

The dcMS depositions were performed at four specific pressures in the range of 0.13–0.73 Pa at 150 W dc power (MDX 500 power supply from advanced energy). For HiPIMS deposition, the power was supplied by a SPIK1000A pulse unit (Melec GmbH) operating in the unipolar negative mode at constant voltage, which in turn was charged by a dc power supply (ADL GS30). The discharge current and voltage were monitored using a combined current transformer and a voltage divider unit (Melec GmbH). The pulse length was 250 μs and the pulse repetition frequency was 100 Hz. At all pressures, the average power during HiPIMS deposition was maintained around 153 W, to be comparable with dcMS grown films at 150 W. The HiPIMS deposition parameters were recorded by a LabVIEW program communicating with our setup through high speed data acquisition (National Instruments).

X-ray diffractometry (XRD) was carried out using a X'pert PRO PANalitical diffractometer (Cu K_α line, wavelength 0.154 06 nm) mounted with a hybrid monochromator/mirror on the incident side and a 0.27° collimator on the diffracted side. A line focus was used with a beam width of approximately 1 mm. Grazing incidence (GI)XRD scans were carried out with the incident beam at $\theta = 1°$. The film thickness, density and surface roughness was determined by low-angle x-ray reflectivity (XRR) measurements with an angular resolution of 0.005°. The film thickness, density and roughness were obtained by fitting the XRR data using the commercial X'pert reflectivity program, that is based on the Parrat formalism [35] for reflectivity.

Magnetic hysteresis was characterized using a home-made high sensitivity magneto-optical Kerr effect (MOKE) looper.

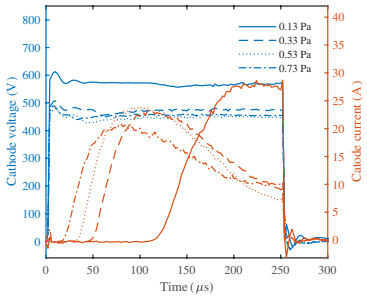

Figure 1. The discharge current–voltage waveform at different pressures, for a 75 mm diameter $Ni_{80}Fe_{20}$ target with Ar as working gas. The line style of the legend applies to both discharge voltage and current traces.

The coercivity is read directly from the easy axis loops. The anisotropy field is obtained by extrapolating the linear low field trace along the hard axis direction to the saturation magnetization level, a method commonly used when dealing with effective easy axis anisotropy.

3. Results and discussion

We deposited Py thin films using HiPIMS and dcMS. We discuss the discharge characteristics of HiPIMS in section 3.1, the films' microstructure in section 3.2 and characterize their magnetic properties in section 3.3.

3.1. Discharge current and voltage waveforms

Figure 1 shows the current and voltage waveforms of the HiPIMS discharge recorded during room temperature growth at different pressures. It can be seen that a nearly rectangular voltage pulse of 250 μs length was applied to the cathode target. Beside oscillations at the beginning and after ending the voltage pulse, there are local minima due to the initial current rise in all cases. The oscillations are due to an internal inductance of the power supply which creates a resonance circuit with the parasitic capacitance of cables and the capacitance of the cathode target. Since the current onset occurs at different times for different pressure, the value of applied voltage (height in the blue curves) changes to maintain the required average power (∼153 W here). Table 1 summarizes cathode voltages used in our depositions which indicate that HiPIMS voltage pulses are well above dcMS discharge voltages.

The current waveforms can be described by three distinct regions, as previously described by Lundin *et al* [36] (I) plasma initiation and a current maximum, followed by (II) a decay to a minimum and then (III) a steady state regime that remains as long as the discharge voltage level is maintained. The initial peak current is a result of strong gas compression

Table 1. Summary of cathode voltage during our depositions at different pressures and applied power. Voltage values are in V.

Method and average power (W)	Pressure (Pa)			
	1.3	3.3	5.3	7.3
HiPIMS 150	583	489	460	459
dcMS 150	406	322	300	295
dcMS 50	370	306	288	—

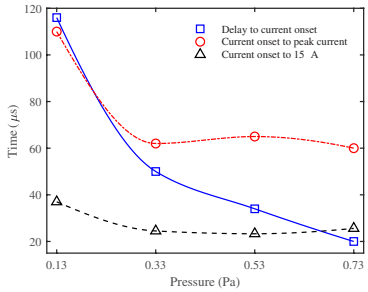

Figure 2. The variation of delay time to current onset and time for current to rise from onset to peak current and 15 A versus Ar pressure.

due to the rapid large flux of sputtered atoms coming from the target. Within a few μs collisions of the sputtered atoms with the working gas atoms leads to heating and expansion of the working gas, known as rarefaction. As a result, the working gas atoms are replaced by the sputtered atoms in the vicinity of the cathode target to some extent as the pulse evolves. However, it has been shown that the rarefaction is primarily due to ionization losses in the target vicinity [37]. The rarefaction causes the discharge current to fall as can be seen for pressures in the range 0.33–0.73 Pa. In this regard, the 0.13 Pa case is different than for higher pressures in all three stages. This is due to a long delay on the current initiation which results in appearance of only the first stage of the discharge current during the voltage pulse. At higher pressures, the second stage is also observable, while the pulse length is not long enough to see the third stage of the current evolution. Figure 2 shows variation of the delay time and time between current initiation to peak current and 15 A as a function of Ar pressure. The current initiation delay time changes linearly in the 0.33–0.73 Pa range and increases dramatically at lower pressures. Previously we have reported the increased delay time with decreasing Ar pressure when sputtering a tantalum target [38] and for a vanadium target in Ar/N_2 mixture [31]. Due to its stochastic nature, the delay time can be explained statistically as described by Yushkov and Anders [39]. In a simplified way, the probability of ionization depends on availability of precursor, mainly represented by the pressure of the working gas and ratio of applied voltage to voltage required for ionization of the gas and sputtered

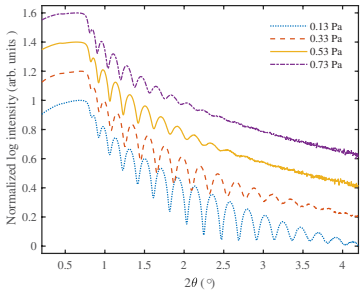

Figure 3. The XRR curves for the film grown with dcMS at room temperature and at various pressures up to nearly the same thickness. The figures are offset vertically for illustration purposes.

atoms. Thus, Yushkov and Anders [39] model the inverse of delay time to be proportional to the cathode voltage. They also proposed a linear variation of delay time with inverse of pressure at constant cathode voltage. However, here we preferred to maintain constant power by increasing the cathode voltage as pressure decreases. Thus there is a competition between cathode voltage increment and pressure decrement to shorten and lengthen the delay time, respectively. Since the delay became longer as the pressure decreased, it can be concluded that in the present study the pressure has a dominant effect over cathode voltage on the length of delay time.

The time required to reach the peak current after current initiation is 115 μs at 0.13 Pa while for higher pressures it stands nearly constant at about 75 μs. Since the peak currents are not equal at different pressures, we also calculate rise time of 0 to 15 A at each pressure. The graph shows the rate of current rise is 0.41 A μs^{-1} at 0.13 Pa and it increases to 0.61 A μs^{-1} by increasing the pressure to 0.33 Pa. At higher pressures the current rise rate remains almost unchanged.

3.2. Microstructure

3.2.1. X-ray reflectivity. Figure 3 shows the x-ray reflectivity curves of the films grown with dcMS at room temperature as an example. The figure clearly shows a change in x-ray reflectivity with pressure. At higher pressures, the amplitude of the oscillations decays faster with incident angle, which represents greater surface roughness of the film [40]. This behavior is reproduced similarly for the rest of the pressure series grown at different conditions but are not shown here. In order to obtain the most precise estimates of thickness, density and surface roughness of the films, the reflectivity curves have to be fitted carefully. To this end we take into account formation of an oxide layer and adsorbed moisture on its surface which is reasonable since the measurements were performed in ambient atmosphere (*ex situ*).

The results of the fitting are shown in figure 4 for both of the deposition methods and both substrate temperatures. All the

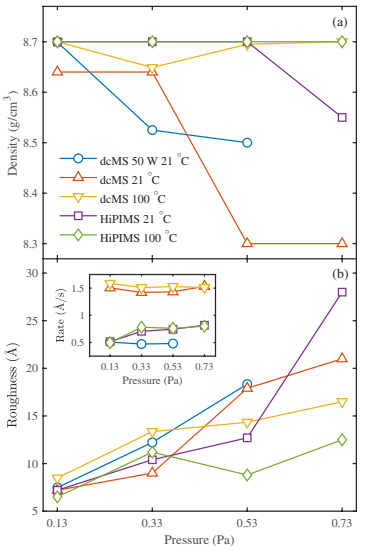

Figure 4. The (a) film density and (b) surface roughness of the films obtained by fitting to XRR curves for the film grown at different pressure with nearly the same thickness. The figure inset shows deposition rate.

films were grown to the same thickness of 37 nm and the deposition rate is shown in the figure inset. We note that HiPIMS deposition has significantly lower deposition rate than dcMS deposition. As shown in figure 4(a), the density of the films grown by dcMS at room temperature shows an abrupt drop in the pressure range between 0.33–0.53 Pa. In contrast, utilizing HiPIMS at room temperature can maintain high density for most of the cases explored. The only exception occurs at 0.73 Pa which density shows deviation from the almost constant high density attained in other HiPIMS deposited samples. One may think that since the average deposition rate of HiPIMS is significantly lower than for dcMS (see figure 4(b) inset) it may result in higher densities. Thus another series was grown by dcMS at 50 W power which gives deposition rate of 0.5 Å s equal to the average deposition rate of HiPIMS at 0.13 Pa. This lower deposition rate at 50 W dcMS improves the density at 0.13 Pa, compared to the 150 W counterpart, but the film density drops as the pressure is increased. Thus the low deposition rate is not solely responsible for the high film density obtained by HiPIMS at room temperature. For both dcMS and HiPIMS growth, increased substrate temperature seems to efficiently maintain the film density at a value very close to the bulk density of 8.72 g cm^{-3} (see [33], page 548). This can

be explained by the fact that at higher pressures the mean free path is reduced and an adatom experiences more collisions and loses more kinetic energy before arriving at the surface. However, raising the substrate temperature to increase the adatom mobility at the surface maintains high density of the film during growth at higher pressures.

The surface roughnesses of the films grown at different conditions are shown in figure 4(b). It is worth noting that the different growth conditions have the minimum effect at the lowest pressure, 0.13 Pa, while the values are more scattered at higher pressures. In general, the trend in surface roughness is an increase with increasing pressure. Our results show precisely such a trend. Also it should be noted that films grown at 100 °C with both deposition methods show less roughness than their lower temperature counterparts grown at higher pressures. Again, this is in agreement with the statement that the more opportunity an adatom has to seek a desirable site on the surface the smoother and denser the resulting film.

For the dcMS grown films, the deposition rate is nearly independent of the pressure variation but with slightly higher values at 100 °C. However, the HiPIMS growth at 0.13 Pa presents considerably lower average deposition rate at both room temperature and 100 °C. This is due to longer delay time at 0.13 Pa which is evident from the trends shown in figures 1 and 2. We would like to remark that the average deposition rate of HiPIMS can be somewhat misleading i.e. by accounting for 100 Hz pulses of 250 μs length and neglecting the delay time, the effective deposition time is below 25 ms per second which gives an effective value of $\sim$40 times the average deposition rate.

We would like to remark that utilizing a weaker magnet in the magnetron might change the behavior of the deposition rate in both dcMS and HiPIMS. For instance, we have noticed that reducing the magnet's field strength to half the value and doubling the target thickness would result in less confinement of plasma with a linear reduction of deposition rate with pressure increment (not shown here). The linear decrease in deposition rate with increased pressure in the 1.33–8 Pa range was reported using HiPIMS [34]. But the main focus of the current study is on the effect of pressure and substrate temperature thus we preferred a constant deposition rate to reduce the number of contributing parameters. The above mentioned effect of the magnetic field strength on HiPIMS deposition was demonstrated earlier and the interested reader is referred to our earlier work on VN deposition [31] for further information.

3.2.2. X-ray diffraction. Figure 5 shows two sets of GIXRD patterns, namely different films grown at fixed pressure of 0.13 Pa with dcMS and HiPIMS at varying temperature and for films grown by HiPIMS at 100 °C at different pressures. Results for other films are not shown here since they show very little difference. The figure insets depict the variation in the (1 1 1) peak intensity and estimated grain size from the Scherrer equation [41], which has been proven to give quantitatively correct values for Py films [42], with pressure for all of the films. The three main peaks are evident in all cases those are located at 44.217, 51.518 and 75.845° corresponding to (1 1 1), (2 0 0) and (2 2 0) planes, respectively [43]. The dominant peak is (1 1 1) in all cases. The (1 1 1) texture provides perpendicular anisotropy to the Py films as for fcc alloy structures the ⟨1 1 1⟩ direction is the easy magnetization axis (see [33], page 224). This becomes important for films somewhat thicker than ours and plays an important role in stripe domain formation. It has been shown for films grown by normal deposition geometry, that an increase in the pressure reduces the peak height and this is most pronounced for the (1 1 1) peak [18]. Only our dcMS grown films at room temperature are in agreement with those results. In contrast, maximum (1 1 1) peak intensity is obtained at 0.33 Pa for dcMS grown films at 100 °C, and at 0.73 Pa for the films grown by HiPIMS at both room temperature and 100 °C. The (2 0 0) peak intensity shows a slight increase while (2 2 0) peak intensity presents a decrease with increasing pressure for all the films (not shown here).

A more quantitative understanding of the film crystallinity is represented by the grain size. The estimated grain size from the (1 1 1) peaks shows negligible variation with pressure. It is also worth noting that dcMS growth results in smaller grain size at room temperature than HiPIMS while it gives larger grain size at 100 °C. Thus increasing the substrate temperature has a more pronounced effect on the grain growth during dcMS deposition.

3.3. Magnetic properties

3.3.1. Anisotropy and coercive fields. Figure 6 shows the variation of the anisotropy field H_k and coercivity H_c with pressure for both dcMS and HiPIMS grown films. The results are extracted from hysteresis loops measured along easy and hard axis of the film using MOKE. It can be clearly seen that H_k increases with increased pressure for films grown by dcMS at room temperature. All our other films have either a nearly constant H_k (dcMS and HiPIMS at 100 °C) or a delayed and slower growth as function of pressure as in the case of the HiPIMS grown film at room temperature. Both increased substrate temperature and the higher ion energy involved in HiPIMS deposition contribute to more adatom surface diffusion, encouraging defect-free crystal growth that helps to maintain the low anisotropy field H_k.

It has been shown previously, that associated with void formation there is an increase in the anisotropy field H_k in Py [9, 23]. Our quantitative results are in good agreement with their interpretation. The density results shown in the inset in figure 6(a) show that the density remains high for the films that exhibit low H_k but drops in the cases where there is an increase in H_k. Presumably the lower density is associated with more defective crystal growth and void formation. Considering the fact that surface roughness increases with pressure in all cases (see figure 4(b)), our results are inconsistent with the results of Choe and Steinback [44] who found a linear reduction in H_k with increased surface roughness. A reason for this difference might be the film thickness i.e. their films were 15 nm thick which makes them more sensitive to the surface properties compared to 37 nm films here which are more influenced by 'bulk-like' properties. Thus, knowing that the grain size is nearly constant for each pressure series (as shown in figure 5

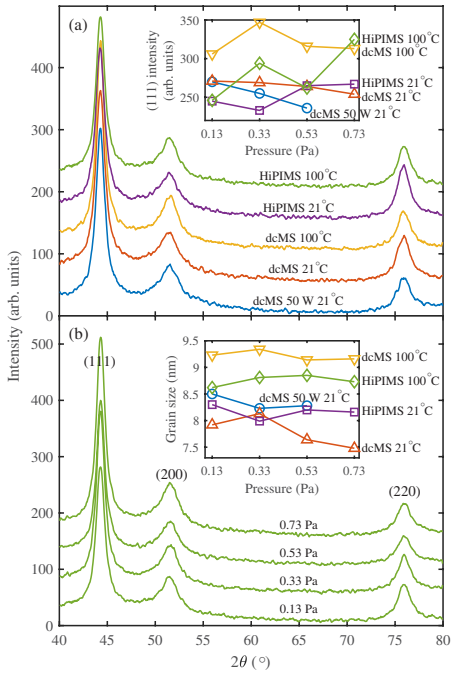

Figure 5. The GIXRD patterns of (a) different films grown at 0.13 Pa (b) films grown at different pressures using HiPIMS at 100 °C. The figure insets shows (1 1 1) peak intensity and grain size estimated from the (1 1 1) peaks using the Scherrer equation.

inset) the variation of H_k here is associated with the density of the films. The high film density is maintained in 0.13 Pa films deposited using HiPIMS and also dcMS at 100 °C while the H_k is low.

The variation of H_c with pressure is shown in figure 6(b). It is clear that at a certain threshold pressure there is a density reduction accompanied by an increase in H_c for films grown at room temperature. For the dcMS deposited films this threshold pressure is at 0.13 and 0.53 Pa, respectively for 50 and 150 W power, while for the room temperature HiPIMS sample it is at 0.73 Pa. Again due to higher film density for growth at 100 °C, the low H_c is maintained at high pressures. Based on surface roughness Choe and Steinback [44] reported two regions: (I) below 8 Å surface roughness where H_c slightly increases with surface roughness and (II) surface roughnesses higher than 8 Å where H_c increases dramatically with surface roughness, due to surface roughness induced pinning of domain walls during magnetization reversal. This is not the case in our results. For instance HiPIMS grown film at 21 °C and 0.73 Pa present highest roughness of the all films while it presents an intermediate H_c compared to the dcMS counterpart. In the present results, the pinning is attributed to voids and defects appearing in films with low mass density.

3.3.2. Magnetization traces. In addition to desirable values of H_k and H_c, for many applications it is also important to have well defined magnetic axes. Figure 7 shows the average of a few loops obtained by MOKE measurements for room temperature grown films. Similar results were obtained for films grown at 100 °C, that are not shown here. The dotted lines belong to dcMS grown films which always present higher saturation fields than their HiPIMS counterparts grown

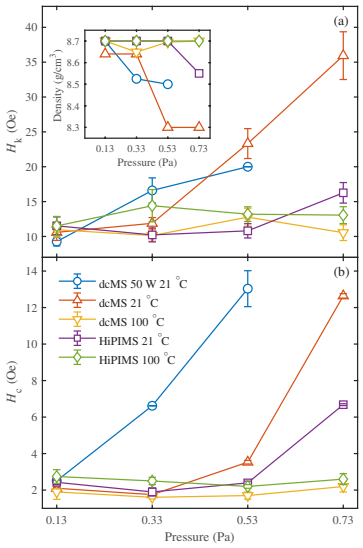

Figure 6. The (a) anisotropy field H_k and (b) coercivity H_c of the films grown to the same thickness at different pressures. These values are extracted from MOKE measurements along hard and easy axis, respectively. The figure inset shows density variation at different pressures.

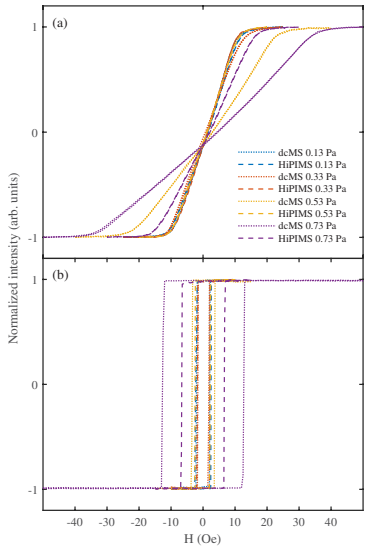

Figure 7. The MOKE response of the films grown by dcMS and HiPIMS at room temperature measured along (a) hard and (b) easy axis of the films.

at the same pressure, shown by dashed lines. This is more evident at higher pressures of 0.53 and 0.73 Pa shown in yellow and purple, respectively.

It can be seen that in both methods, deposition under an angle provides a linear non-hysteretic hard axis and a square easy axis with sharp transitions. However, it has been shown previously that dcMS deposition normal to substrate at high pressure with *in situ* magnetic field, gives open hard axis and rounded easy axis traces [18]. We have shown previously that at low pressures (0.13 Pa) the effect of deposition under an angle on the direction of the magnetization axis can be stronger than the effect of an *in situ* magnetic field during growth [20, 21]. The present results show that uniaxial anisotropy induced by tilt deposition maintains the shape of loops at different pressures. Although we have detected an increase in both H_k and H_c in some of the samples grown at room temperature (see figure 6) there is no indication of out-of-plane magnetization or poorly defined uniaxial anisotropy in those samples.

4. Conclusions

We have demonstrated the deposition of $Ni_{80}Fe_{20}$ thin films using high power impulse magnetron sputtering, HiPIMS. For comparison we also deposited films using dc magnetron sputtering under the same conditions, i.e. to the same thickness, at the same pressure, substrate temperature, tilt angle and with power identical to the HiPIMS average power. We compared the results of structural characterization (x-ray) and magnetic properties. The results indicate that the higher the adatom energy, as it meets with the sample substrate/film, the denser the film, accompanied with low coercive and anisotropy fields. All conditions kept the same, the HiPIMS deposition method gives a higher adatom energy than dcMS. Increased adatom energy can also be achieved by raising the deposition temperature or lowering the pressure. In accordance with this our results show a drop in film density for samples deposited at room temperature (our lowest deposition temperature) with increasing pressure, accompanied by a rise in both coercive and anisotropy fields.

Acknowledgments

This work was partially supported by the University of Iceland Research Funds for Doctoral students, the Icelandic Research Fund Grant Nos. 130029 and 120002023, and the Swedish Government Agency for Innovation Systems (VINNOVA) contract no. 2014-04876.

ORCID iDs

Movaffaq Kateb https://orcid.org/0000-0002-2518-3988
Hamidreza Hajihoseini https://orcid.org/0000-0002-2494-6584
Jon Tomas Gudmundsson https://orcid.org/0000-0002-8153-3209
Snorri Ingvarsson https://orcid.org/0000-0001-8397-8917

References

[1] McGuire T and Potter R 1975 *IEEE Trans. Magn.* **11** 1018
[2] Andricacos P C and Robertson N 1998 *IBM J. Res. Dev.* **42** 671
[3] Craus C B, Onoue T, Ramstöck K, Geerts W G M A, Siekman M H, Abelmann L and Lodder J C 2005 *J. Phys. D: Appl. Phys.* **38** 363
[4] Cooper E I, Bonhote C, Heidmann J, Hsu Y, Kern P, Lam J W, Ramasubramanian M, Robertson N, Romankiw L T and Xu H 2005 *IBM J. Res. Dev.* **49** 103
[5] Yokoshima T 2010 *Electrochemical Nanotechnologies* ed T Osaka *et al* (New York: Springer) pp 67–85
[6] Åkerman J 2005 *Science* **308** 508
[7] Wang J, Zhang X, Lu X, Zhang J, Yan Y, Ling H, Wu J, Zhou Y and Xu Y 2017 *Appl. Phys. Lett.* **111** 072401
[8] Umezaki H, Nishida H, Tsumita N, Koyama N, Nozawa H and Sugita Y 1982 *IEEE Trans. Magn.* **18** 753
[9] Sugita Y, Fujiwara H and Sato T 1967 *Appl. Phys. Lett.* **10** 229
[10] Shimokawa T, Yanai T, Takahashi K, Nakano M, Suzuki K and Fukunaga H 2012 *IEEE Trans. Magn.* **48** 2907
[11] Theis M, Ediger S, Schmitt M T, Hoffmann J E and Saumer M 2013 *Phys. Status Solidi* a **210** 853
[12] Yanai T, Eguchi K, Koda K, Kaji J, Aramaki H, Takashima K, Nakano M and Fukunaga H 2018 *AIP Adv.* **8** 056123
[13] Watanabe G, Koizumi S, Yamada T, Takemura Y and Shirakashi J 2005 *J. Vac. Sci. Technol.* B **23** 2390
[14] Collins A J, Prior C J and Hicks R C J 1981 *Thin Solid Films* **86** 165
[15] Yang M M and Aboaf J A 1989 *J. Appl. Phys.* **66** 3734
[16] Pötzlberger H W 1984 *IEEE Trans. Magn.* **20** 851
[17] Rijks T G S M, Lenczowski S K J, Coehoorn R and de Jonge W J M 1997 *Phys. Rev.* B **56** 362
[18] Svalov A, Aseguinolaza I, Garcia-Arribas A, Orue I, Barandiaran J, Alonso J, Fernández-Gubieda M and Kurlyandskaya G 2010 *IEEE Trans. Magn.* **46** 333
[19] Chaug Y-S and Williamson D L 1990 *J. Vac. Sci. Technol.* A **9** 505
[20] Kateb M and Ingvarsson S 2017 *IEEE Sensors Applications Symp.* (Glassboro, NJ: IEEE) pp 13–5
[21] Kateb M, Jacobsen E and Ingvarsson S 2018 *J. Phys. D: Appl. Phys.* submitted
[22] Barranco A, Borras A, Gonzalez-Elipe A R and Palmero A 2016 *Prog. Mater. Sci.* **76** 59
[23] Fujiwara H and Sugita Y 1968 *IEEE Trans. Magn.* **4** 22
[24] Kools J 1995 *J. Appl. Phys.* **77** 2993
[25] Helmersson U, Lattemann M, Bohlmark J, Ehiasarian A P and Gudmundsson J T 2006 *Thin Solid Films* **513** 1
[26] Gudmundsson J T, Brenning N, Lundin D and Helmersson U 2012 *J. Vac. Sci. Technol.* A **30** 030801
[27] Samuelsson M, Lundin D, Jensen J, Raadu M A, Gudmundsson J T and Helmersson U 2010 *Surf. Coat. Technol.* **205** 591
[28] Magnus F, Ingason A S, Sveinsson O B, Olafsson S and Gudmundsson J T 2011 *Thin Solid Films* **520** 1621
[29] Magnus F, Ingason A S, Olafsson S and Gudmundsson J T 2012 *IEEE Electron Device Lett.* **33** 1045
[30] Alami J, Persson P O Å, Music D, Gudmundsson J T, Bohlmark J and Helmersson U 2005 *J. Vac. Sci. Technol.* A **23** 278
[31] Hajihoseini H and Gudmundsson J T 2017 *J. Phys. D: Appl. Phys.* **50** 505302
[32] Velicu I-L, Neagu M, Chiriac H, Tiron V and Dobromir M 2012 *IEEE Trans. Magn.* **48** 1336
[33] O'Handley R C 2000 *Modern Magnetic Materials: Principles and Applications* (New York: Wiley)
[34] Velicu I-L, Kowalczyk M, Neagu M, Tirona V, Chiriac H and Ferenc J 2013 *Mater. Sci. Eng.* B **178** 1329
[35] Parratt L G 1954 *Phys. Rev.* **95** 359
[36] Lundin D, Brenning N, Jadernas D, Larsson P, Wallin E, Lattemann M, Raadu M A and Helmersson U 2009 *Plasma Sources Sci. Technol.* **18** 045008
[37] Huo C, Raadu M A, Lundin D, Gudmundsson J T, Anders A and Brenning N 2012 *Plasma Sources Sci. Technol.* **21** 045004
[38] Gudmundsson J T, Alami J and Helmersson U 2002 *Surf. Coat. Technol.* **161** 249
[39] Yushkov G Y and Anders A 2010 *IEEE Trans. Plasma Sci.* **38** 3028
[40] Li W, Yan X, Aberle A G and Venkataraj S 2015 *Japan. J. Appl. Phys.* **54** 08KC14
[41] Langford J I and Wilson A 1978 *J. Appl. Crystallogr.* **11** 102
[42] Neerinck D G, De Veirman A E M, Slangen M H J, Rijks T G S M and Kools J C S 1996 *Thin Solid Films* **280** 136
[43] Dzhumaliev A, Nikulin Y V and Filimonov Y A 2016 *Phys. Solid State* **58** 1053
[44] Choe G and Steinback M 1999 *J. Appl. Phys.* **85** 5777

Paper III

Application of an extended van der Pauw method to anisotropic magnetoresistance measurements of ferromagnetic films

M. Kateb, E. Jacobsen and S. Ingvarsson 2019

Journal of Physics D: Applied Physics 52 (7) 2019, 075002 (12pp)

IOP Publishing Journal of Physics D: Applied Physics
J. Phys. D: Appl. Phys. **52** (2019) 075002 (12pp) https://doi.org/10.1088/1361-6463/aaf4c9

Application of an extended van der Pauw method to anisotropic magnetoresistance measurements of ferromagnetic films

Movaffaq Kateb, Egill Jacobsen and Snorri Ingvarsson[1]

Science Institute, University of Iceland, Dunhagi 3, IS-107, Reykjavik, Iceland

E-mail: mkk4@hi.is, egilljac@gmail.com and sthi@hi.is

Received 21 February 2018, revised 20 November 2018
Accepted for publication 29 November 2018
Published 14 December 2018

Abstract

We demonstrate anisotropic resistivity measurements using the extended van der Pauw (vdP) method in ferromagnetic $Ni_{80}Fe_{20}$ (Py) films. We apply it to measure anisotropic magnetoresistance (AMR) and compare the results of the vdP method with the more conventional Hall-bar method along the hard and easy axis of the film and show that the vdP method gives more reliable AMR result. For instance the AMR result along the hard and easy axis of the film are in close agreement. Further, we applied the vdP method to study AMR in a series of Py films with thicknesses ranging between 10–250 nm. The films were grown by sputtering deposition at an angle with respect to the substrate normal and with an *in situ* magnetic field, both conditions assisting in the definition of in-plane uniaxial anisotropy. The microstructure of Py films was characterized using x-ray reflectivity, diffraction and polar mapping of (1 1 1) planes. We detected no off-normal texture and negligible surface roughness, which indicates that self-shadowing is not dominating in our growth. Yet the films have well defined uniaxial anisotropy. Abrupt changes in the average resistivity versus film thickness were observed, which cannot be explained by the models accounting for the thickness and grain size but strongly correlate with the changes in (1 1 1) texture in the films. We compared our results with the literature and show that independent of growth method, substrate and deposition temperature, the AMR value presents a saturation behavior with thickness at about 100 nm.

Keywords: anisotropic magnetoresistance, van der Pauw, tilt deposition, thickness, texture

(Some figures may appear in colour only in the online journal)

1. Introduction

Anisotropic magnetoresistance (AMR) is defined as the variation of resistance upon changing the relative alignment of electric current and magnetization [1]. Results of AMR measurements can be affected by the measurement technique as well as the sample preparation method [1]. For instance, Chikazumi [2] measured AMR by sweeping the magnetic field while performing resistance measurement along the $Ni_{78.5}Fe_{21.5}$ bars. He showed that different bars magnetized in different directions present different AMR results. Bozorth [3] has shown that determining AMR by applying saturating fields parallel and perpendicular to current direction avoids erratic results in the early literature caused by ignoring the initial magnetization state of the specimen.

It was suggested already by McGuire and Potter [1] that use of van der Pauw (vdP) method might improve the precision in determining AMR properties of thin films. The vdP method is a simple and flexible technique to probe resistivity of uniform, continuous thin films of arbitrary shape [4, 5]. However, the original vdP formalism is limited to specimens with isotropic resistivity (ρ_{iso}). It has been shown that the vdP

[1] Author to whom any correspondence should be addressed.

method can be extended to determine anisotropic resistivity [6] and that ρ_{iso} measured by the original technique is the geometric mean of resistivities along the principle axes of the film i.e. $\rho_{iso} = \sqrt{\rho_1 \rho_2}$ [5, 6].

AMR results also depend on the thin film deposition technique, and in particular on the resulting microstructure and magnetization [1]. Control over magnetization direction can be achieved by applying *in situ* magnetic field during growth or by depositing under an angle with respect to the substrate normal [7]. The origin of magnetic field induced anisotropy in permalloy $Ni_{80}Fe_{20}$ (Py), in which the effect of magnetostriction is negligible, was mainly attributed to directional ordering of Fe/Ni atom pairs [2, 8]. The tilt angle, however, has been thought to induce anisotropy due to self-shadowing effect [7]. Since then, it has been shown that self-shadowing leads to off-normal fibrous texture in Py [9, 10]. This encourages perpendicular (out-of-plane) anisotropy in the film and thus lowers in-plane anisotropy or even leads to in-plane isotropy, i.e. a complete loss of in-plane anisotropy [11]. However, it is still unclear how tilt deposition contributes to the in-plane uniaxial anisotropy.

There are a limited number of studies on the simultaneous utilization of *in situ* magnetic field and tilt deposition [9, 12–14]. Sun *et al* [9] reported a deterioration of uniaxial anisotropy and loss of magnetic softness in CoZrO films by increase in tilt angle (0–55°) in the presence of an *in situ* field of 400 Oe which assisted the easy axis induced by the tilt angle. Phuoc *et al* [12] showed that in the presence of a 200 Oe assisting magnetic field, the anisotropy field of Py/IrMn bilayer increases with increase in tilt angle, which is more pronounced for angles larger than 35°. Oliveira *et al* [13] studied 150 Oe competing field, i.e. a field perpendicular to the easy axis defined by the tilt angle, in the Cu/IrMn/Py/Cu system. They showed that the magnetic axis can be rotated ∼10–30° with respect to original easy axis induced by the tilt angle depending on the tilt angle. More recently, we studied deposition of Py under a 35° tilt angle with three different field configurations: zero field, assisting and competing *in situ* saturation field of 70 Oe [14]. In our study we showed that tilt angle always determines the easy axis, even if the applied field competes with the easy axis induced by the tilt angle. It was also shown that a combination of tilt angle and assisting field results in very well defined uniaxial anisotropy in the Py i.e. square easy axis with sharp switching and linear hard axis without hysteresis.

In this work, we use the extended vdP method for AMR measurements in Py films and compare it with the more conventional method of defining Hall-bar patterns in the films. We use the method to study a series of different thickness Py films, prepared by tilt deposition with an assisting *in situ* magnetic field, to make sure they present well defined uniaxial anisotropy. We do careful x-ray measurments in studying the microstructure, e.g. texture, of our films and compare our results with the literature. We find that there is a change in microstructure as the films increase in thickness, and that this is reflected in the resistivity measurements.

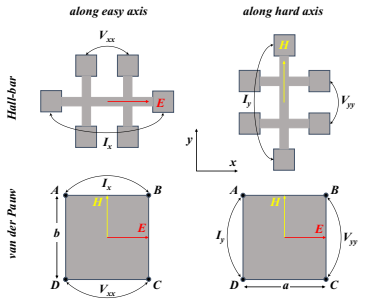

Figure 1. Schematic illustration of resistance measurements along hard (H) and easy (E) axis for both hall-bar and vdP methods.

2. Experimental method

2.1. Magnetoresistance measurements

We compared the magnetoresistance obtained by vdP and by lithographically patterned Hall-bars. To this end, clean (0 0 1) p–Si was dehydrated at 140 °C for 5 min on a hotplate and then exposed to HMDS vapor for 5 min to become more hydrophilic. Then 1–2 ml maN-1410 photoresist (Micro resist tech. GmbH) was dispensed and spin coated at 4000 rpm for 300 s (pre-spin at 500 rpm for 15 s) and soft baked at 100 °C for 90 s. This gives 1 μm thick resist on a 4" wafer. After 6 s exposure (DUV-1000 AB-M Inc. mask aligner) at 25 mW cm^{-2} the pattern was developed in maD-533/S (Micro resist tech. GmbH) for 30 s and rinsed with DI water and dried with N_2. Square (15 × 15 mm^2) and Hall-bar (0.4 × 1.6 mm^2) patterns were grown simultaneously and prepared with a lift-off in Acetone. The growth process included a 4 nm thick Cr underlayer, for adhesion, and a 40 nm thick Py film. During deposition, an *in situ* magnetic field of 70 Oe was applied to induce uniaxial anisotropy in the desired direction, without the aid of the tilt angle. The Hall-bars were made large enough that the in-plane shape anisotropy of the Hall-bar structure would not affect the magnetization direction induced during growth. Then the AMR was measured as shown schematically in figure 1 by driving current through the Hall-bar and measuring voltage at the side contacts.

In the vdP method, four small contacts must be placed on the sample perimeter. We choose to work with square samples, with electrical contacts at each of the four corners labeled A, B, C, and D as illustrated in figure 1. While the resistivity in magnetic materials is clearly anisotropic, the original vdP method assumes the film is isotropic. The corresponding isotropic resistivity value, ρ_{iso} is obtained by:

$$\exp\left(-\frac{\pi d}{\rho_{iso}} R_{AB,CD}\right) + \exp\left(-\frac{\pi d}{\rho_{iso}} R_{AD,CB}\right) = 1 \quad (1)$$

where d is the film thickness and e.g. $R_{AB,CD}$ is the resistance obtained by applying current to AB and picking up the voltage at the opposite side between CD or vice versa. It has been shown that $\rho_{iso} = \sqrt{\rho_x \rho_y}$ is the geometric mean of principle resistivities in anisotropic thin films [5, 6] i.e. along the easy (ρ_x) and the hard (ρ_y) axes in our case. The ratio of principle resistivities can be obtained from Price's [6] extension to the vdP method for anisotropic samples, as below:

$$\sqrt{\frac{\rho_x}{\rho_y}} = -\frac{b}{\pi a} \ln\left(\tanh\left[\frac{\pi d R_{AD,CB}}{16\rho_{iso}}\right]\right) \tag{2}$$

where b and a are the side lengths of a rectangular sample and $R_{AD,BC}$ is resistance along the b sides as described above. Equation (2) yields the ratio of easy and hard axis resistivity. The individual values of principle resistivities can subsequently be obtained by:

$$\rho_x = \rho_{iso}\sqrt{\frac{\rho_x}{\rho_y}} \tag{3}$$

$$\rho_y = \rho_{iso}\left(\sqrt{\frac{\rho_x}{\rho_y}}\right)^{-1}. \tag{4}$$

Our magnetoresistance measurements were done at in-plane saturation field of ∼23 Oe parallel and perpendicular to the current direction, respectively. The strength of the field is enough to saturate the magnetization as it is 10 times the coercive field H_c and 5 times of H_k in our thinnest films. All measurements were performed at room temperature. Since high current densities may perturb local magnetization [15] and/or produce heating, care was taken to use low current densities in resistivity measurements. Thus we swept between ± 10 mA for measuring vdP and Hall-bar resistivities (the I–V curves were perfectly linear within this range). The AMR ratio is given by [1]:

$$\mathrm{AMR} = \frac{\Delta\rho}{\rho_{ave}} = \frac{\rho_{\parallel} - \rho_{\perp}}{\rho_{ave}} \tag{5}$$

where ρ_{ave} for FCC materials like Py defined as [1]:

$$\rho_{ave} = \frac{1}{3}\rho_{\parallel} + \frac{2}{3}\rho_{\perp} \tag{6}$$

where $\rho_{\parallel}$ and $\rho_{\perp}$, respectively, are resistivities with magnetization saturation parallel and perpendicular to the current direction. Thus, each of the ρ_x and ρ_y can be translated to $\rho_{\parallel}$ and $\rho_{\perp}$ by applying proper external magnetic field. To this end three vdP measurement was performed i.e. without applied field (B_0), with saturation field along the easy (B_{easy}) and hard (B_{hard}) axes, respectively. This yields values for ρ_{iso} at B_0, B_{easy} and B_{hard} that can be translated to ρ_{easy} and ρ_{hard} using equations (3) and (4). Now, for example, AMR along easy axis is determined by considering $\rho_{\parallel}$ to be ρ_{easy} at B_{easy} and $\rho_{\perp}$ equal to ρ_{easy} at B_{hard}. In a similar manner one can define AMR along the hard axis by using $\rho_{\parallel} = \rho_{hard}$ at B_{hard}, and $\rho_{\perp} = \rho_{hard}$ at B_{easy}.

The definition of AMR does not contain any reference to sample geometry or its crystalline or other anisotropies, only the angle between magnetization and current direction.

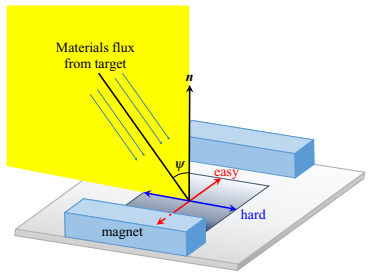

Figure 2. Schematic illustration of deposition geometry and tilt angle induced hard and easy axis in the film.

Assuming the x'-axis being some general current direction, one can determine $\rho_{x'}$:

$$\rho_{x'} = \rho_{\parallel} + \Delta\rho\cos^2\theta \tag{7}$$

here θ stands for angle between current (x') and saturated magnetization direction. It is worth noting that equation (7) states the resistivity is only dependent on θ and not on the zero field easy and hard axis directions.

2.2. Thickness series grown by field assisted tilt sputtering

Our deposition configuration for studying the effect of different thickness is shown schematically in figure 2. Regardless of growth method, e.g. evaporation [7], DC or RF magnetron sputtering [16] or even presence/absence of applied field [14], tilt deposition has been found to determine the magnetic easy axis in Py.

Our series of samples with different thickness was grown on (0 0 1) p–Si with a 100 nm thick layer of thermally grown oxide. No underlayer was used since we have found that tilt deposited underlayer increases anisotropy field in our films, as has been reported by others [9, 16, 17]. Our depositions were carried out in a UHV ($<5 \times 10^{-9}$ mbar base pressure) magnetron sputter system at a pressure of 1.3×10^{-3} mbar and 150 W which results in 1.20 Å s^{-1} deposition rate. The deposition angle was 35° with respect to the substrate normal, with a target to substrate distance of 20 cm. During deposition, a magnetic field of 70 Oe was applied using a pair of permanent magnets attached to the sample holder. The entire sample holder rotated around the substrate normal n 360° back and forth at ∼12.8 rpm. The process of stopping and reversing takes 200 ms. The rotation is necessary in order to obtain uniform film thickness, while the stop time before reversal is what determines the magnetization axis along with the tilt angle. Thickness uniformity over large area was examined simply by lifting-off pre-patterned lines (from side to side and along diagonals of our 20×20 mm^2 substrates) followed by step height measurement using atomic force microscopy (AFM).

Table 1. Resistivity measurements using vdP and Hall-bar methods along hard and easy axes (according to figure 1) in $\mu\Omega$cm. The $\parallel$ and $\perp$ in the superscript are denoting $\rho_{\parallel}$ and $\rho_{\perp}$ in each direction.

Method	Current direction	$\rho_{\text{current}-\text{direction}}(B)$			$\rho_{\parallel} - \rho_{\perp}$	ρ_{ave}	AMR (%)
		B_0	B_{easy}	B_{hard}			
Hall-bar	Easy	33.6911	$33.4460^{\parallel}$	$33.0269^{\perp}$	0.41902	33.1666	1.2634
Hall-bar	Hard	35.8481	$35.7178^{\perp}$	$36.3524^{\parallel}$	0.6346	35.9293	1.7672
vdP	Easy	32.0508	$32.1325^{\parallel}$	$31.4900^{\perp}$	0.6425	31.9183	2.0130
vdP	Hard	30.9832	$30.9697^{\perp}$	$31.5251^{\parallel}$	0.5963	31.3673	1.9010

X-ray diffraction (XRD) was carried out using a X'pert PRO PANalitical diffractometer (Cu K_{α} line, wavelength 0.154 06 nm) mounted with a hybrid monochromator/mirror on the incident side and a 0.27° collimator on the diffracted side. A line focus was used with a beam width of approximately 1 mm. Grazing incidence (GI) XRD scans were carried out with the incident beam at $\theta = 1°$ with 0.05°. The film thickness, density and surface roughness was determined by low-angle x-ray reflectivity (XRR) measurements with 0.005° angular resolution. XRR measurements were fitted using a commercial X'pert reflectivity program based on Parrat formalism [18]. Further, pole scans were done which enable detecting the texture evolution in tilt sputtered films [19]. Briefly, a pole scan is done for a specific d-spacing, i.e. a fixed $\theta - 2\theta$ peak while the specimen is rotated in-plane (ϕ) at different out-of-plane (ψ) angles. Normally, a single pole scan is not enough to fully determine the orientation distribution within a specimen. However, since our films are polycrystalline the main focus of the present study is on the pole figure for (1 1 1) planes. We measured the (1 1 1) pole figures by setting $\theta - 2\theta$ to the corresponding peak obtained in the normal XRD. We also repeated such measurement for the bare substrate and found that the raw pole figures of the films were affected by the substrate pattern. Thus we subtracted the substrate pattern from raw pole figures assuming they are collected at identical conditions. To emphasize the changes in $\langle 1\,1\,1 \rangle$ texture with the film thickness we subtracted the pole figure of each film by the film with the next lower thickness, e.g. we subtracted the pole figure of 40 nm from 50 nm, 50 nm from 75 nm and so on. Thus we might be able to detect texture evolution more clearly.

To obtain hysteresis loops, we used a high sensitivity magneto optical Kerr effect (MOKE) looper. The detail on the MOKE setup can be found in [20, section 3.2.1]. We used a constant field step of 0.2 Oe along the easy axis and 1 Oe along the hard axis of the film in the range ± 60 Oe, with dwell time of 300 ms. Coercive field (H_c) was read directly from the loop widths along the easy axis and anisotropy field was obtained by extrapolating the hard axis MH curve at low field to high field values and determining the field for which the material saturates. It is worth mentioning that the latter is a common method in the case when there are well defined easy and hard directions at right angles.

For the thickness series all resistivity and AMR measurements were done using vdP method.

3. Results and discussions

3.1. Magnetoresistance measurements

We compared the result of vdP with the Hall-bar method for identical test samples of Py, deposited simultaneously and with the sputter at normal incidence. Table 1 summarizes the result of resistivity measurements by both methods at different magnetization i.e. B_0, B_{easy} and B_{hard}. The table also contains primary magnetoresistance values of $\Delta\rho$, ρ_{ave} and AMR. The results show that the vdP method always presents lower resistivity values than the Hall-bar method. The difference in ρ_{ave} along the hard and easy axis is 7.7% employing the Hall-bar method. This is noticeable error since the ρ_{ave} is measured at saturated magnetization and must be independent of the zero field magnetization state of the specimen [3]. While, the ρ_{ave} difference in the vdP method presents a more reasonable 1.7% difference which is in better agreement with the definition of ρ_{ave}. Finally, the AMR values determined by the vdP method show an absolute difference of 0.11% along the easy and hard directions, while conventional Hall-bar method result in 0.5% absolute difference in AMR.

It is worth noting that the Hall-bar method provides a very simple route for direct measurement of magnetoresistance, i.e. simply by recording resistance values when sweeping applied field parallel and perpendicular to the bar. The vdP method however, demands that one switches contacts during measurement and requires more, albeit rather simple, data processing. Besides ρ_{iso} obtained by original vdP equation does not show any change at B_0, B_{hard} and B_{easy} and had to be extended for AMR measurement. Having verified the extended vdP method for measuring AMR we apply it to tilt deposited samples of different thickness.

3.2. Thickness series grown by field assisted tilt sputtering

3.2.1. Growth calibration. In general, thickness uniformity is a major problem in tilt deposition. However, rotation of the substrate in our geometry (see figure 2) resolves this issue as confirmed by AFM measurement to be less than 3 Å in a 18×18 mm^2 area for a 30 nm thick film. While for the film grown with identical conditions but without rotation, a 6 nm difference in thickness was determined.

Figure 3 shows the effects of rotation on the H_k and H_c of the samples grown without field and with field either assisting or competing with the tilt angle. The samples without rotation

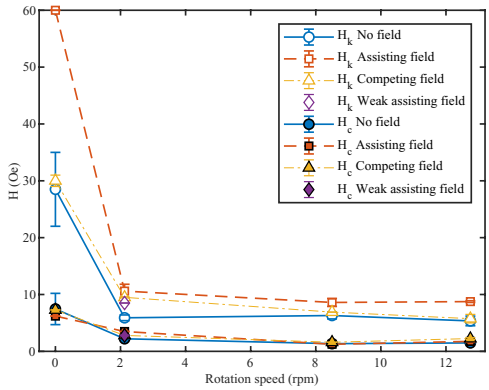

Figure 3. Effects of rotation speed on the H_k (hollow symbols) and H_c (filled symbols) of films deposited at a 35° angle with respect to the substrate normal without field and with field assisting and competing tilt angle.

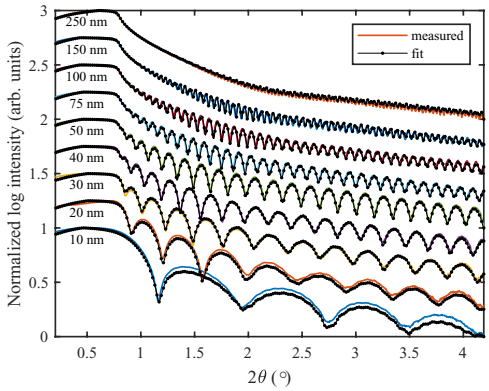

Figure 4. The measured and fit XRR curves of different Py films with 10–250 nm thicknesses. The curves shifted manually for clarity. Our films were deposited at a 35° angle with respect to the substrate normal with assisting *in situ* magnetic field of 70 Oe at ∼12.8 rpm rotation speed.

present very high values of both H_k and H_c which might be due to thickness non-uniformity. However, low rotation speed of ∼2.1 rpm causes a sharp drop in all cases and results seem unchanged at higher speeds. It is worth noting the H_k obtained in the assisting field configuration is always higher than the competing and no-field counterparts. Further we also tried applying a much weaker assisting field of 20 Oe which gives intermediate H_k and H_c between those of assisting field and no-field as shown by diamond markers in the figure. Thus, the stronger *in situ* field gives higher H_k in our case.

3.2.2. X-ray reflectivity (XRR). The thickness, density and roughness of the films were obtained by fitting the XRR curves shown in figure 4. The results of fitting summarized in table 2. It can be seen that the fits agree almost perfectly with the data. To get the best fits both PyO and water layers

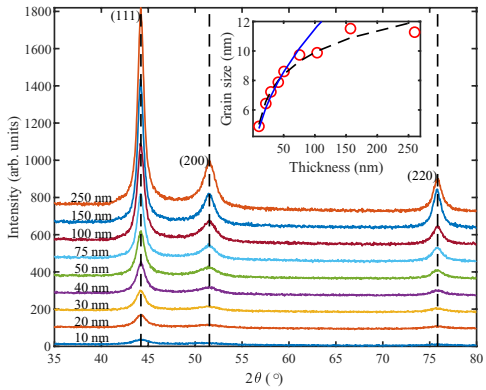

Figure 5. GIXRD pattern of Py with different thicknesses. The vertical dashed lines are indicating the bulk peak positions. The inset shows the estimated grain size (red circles) from the Scherrer formula compared with square-root (solid blue) and natural logarithm (dashed black) dependency on thickness. Our films were deposited at a 35° angle with respect to the substrate normal with assisting *in situ* magnetic field of 70 Oe at ∼12.8 rpm rotation speed.

were included in the fit procedure, which is reasonable since the measurements were done in air atmosphere. The thicknesses of the samples indicate a stable growth rate of precisely 1.2 Å s^{-1}. The densities of the films show very slight fluctuation about their average of 8.61 g cm^{-3}. The uncertainty in the fit results decreases at higher thicknesses since there is more film material exposed by x-ray and more fringes to fit. The surface of the films present excellent smoothness, with x-ray results showing about 2 Å roughness. For a few samples the roughness was verified by AFM, which gave results in the range 1.9–2.8 Å RMS. Even though there appeared to be a slight difference in the roughness obtained in XRR fit and AFM both method verifying extreme smoothness of our films. Since self-shadowing is associated with appearance of noticeable surface roughness, a negligible surface roughness obtained here indicates that self-shadowing is not dominating in our growth. Thus its contribution to the obtained uniaxial anisotropy is highly doubtful.

3.2.3. Microstructure. Figure 5 shows the GIXRD pattern of the films which is a common technique in characterization of polycrystalline thin films. For the 10 nm thick sample the only detectable peak is (1 1 1) at 44.22° while all our thicker films also present (2 0 0) and (2 2 0) peaks at 51.75 and 76.02°, respectively. The strong (1 1 1) peak followed by intermediate (2 0 0) and weak (2 2 0) is sometimes referred to as a characteristic of sputtered Py [21]. The increase in the (1 1 1) peak height with thickness indicates an enhancement in crystallinity which can be quantified using the Scherrer formula. The estimated grain size from the (1 1 1) peak is shown by red circles in the figure inset. Typically the grain size of FCC elements grows as the square root of the film thickness [22]. In our case, however, at thicknesses above 50 nm the grain size deviates from a square root behavior (indicated by the solid blue line). This has also been observed by Neerinck *et al* [22], investigated by transmission electron microscope (TEM) imaging, finding that grain boundary pinning by voids limits normal grain growth in sputtered Py films. They also showed that estimated grain size, by the Scherrer formula from GIXRD pattern, is in agreement with the grain size observed by TEM. The dashed line shows natural logarithm which is plotted to aid the eye. We emphasize that our 150 nm thick sample presents the largest estimated grain size. In addition, the (2 2 0) peak of this sample is higher than the rest of the films with respect to the background intensity. This indicate a variation of growth mode at different thickness.

We emphasize that the incident angle is fixed in GIXRD, at 1° in our case, and thus the normal vector of detected planes rotates during measurement. (The only detection angle where it is normal to the substrate would be at $2\theta = 2°$). This means that the (1 1 1), (2 0 0) and (2 2 0) peaks are obtained at different angles with respect to the substrate. This should be kept in mind when comparing them.

Figure 6 shows the (1 1 1) pole figures of Py films with thicknesses higher than 50 nm. It has been shown that determining the texture of polycrystalline Py with thickness below 35 nm is rather difficult [23]. The left column shows the original pole figures which has a vortex like pattern between $\psi = 35$–$65°$. It originates from the substrate, due to the interaction depth of the x-ray (∼2 μm) compared to small thickness of the films. In an attempt to remove the substrate pattern we subtracted a pure substrate pole figure from the films' pole figures, assuming the pole figures of the films are obtained under reasonably identical conditions as the substrate.

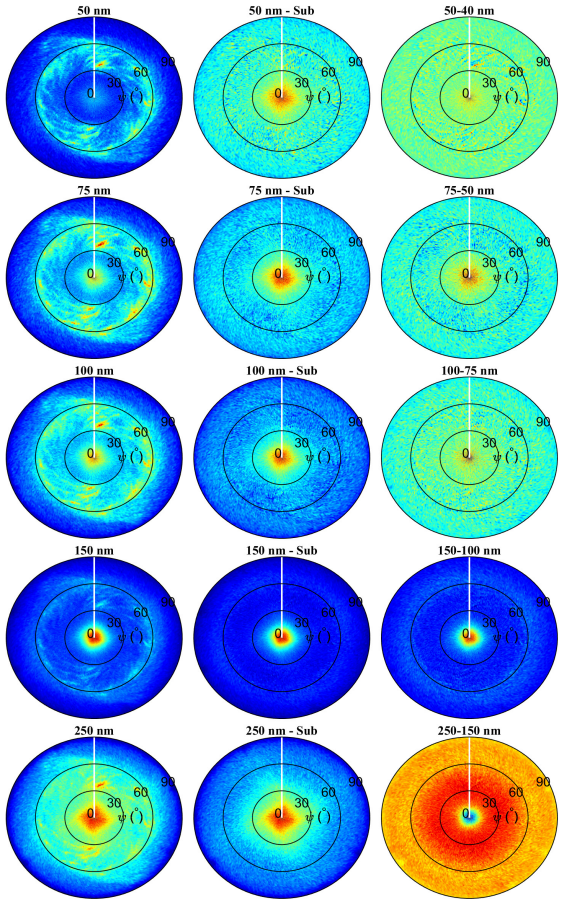

Figure 6. Normalized intensity pole figures of the (1 1 1) peak for 50–250 nm samples: unmodified pole figure (left), after subtracting the pure substrate pattern (middle), and after subtracting pole figure from the next thinner film (right). The white line along the north indicates the direction of the sputtered flux during 200 ms stop-and-turn. Our films were deposited at a 35° angle with respect to substrate normal with an assisting *in situ* magnetic field of 70 Oe at ∼12.8 rpm rotation speed.

The pole figures after subtracting the substrate pattern become more identical to each other as shown in the middle column of figure 6. All these pole figures show an intense spot in the center indicating ⟨1 1 1⟩ is preferred growth direction normal to the substrate ($\psi = 0$) without any tilted texture. The ⟨1 1 1⟩ fiber texture normal to the substrate has been detected previously in Py using TEM [24]. It has also been shown that the rotation of the sample during growth encourages texture

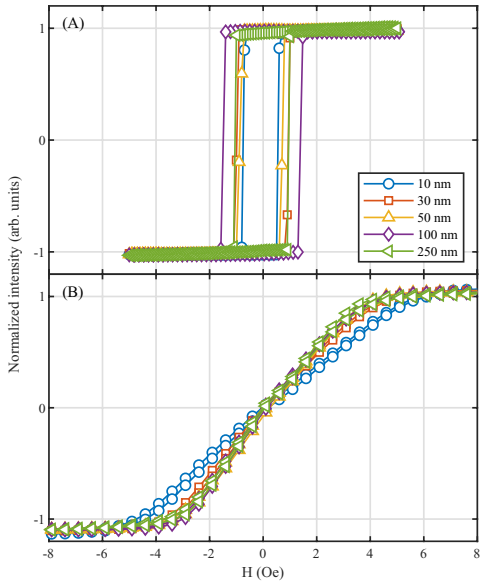

Figure 7. MOKE hysteresis loops along the (A) easy axis and (B) hard axis of the films with various thicknesses. Our films were deposited at a 35° angle with respect to the substrate normal with assisting *in situ* magnetic field of 70 Oe at ∼12.8 rpm rotation speed.

normal to the substrate [15], rather than a tilted texture. Again this indicates the self-shadowing is not dominant here and its contribution to the obtained uniaxial anisotropy is doubted. It can be seen that the sharpness of the ⟨1 1 1⟩ spot is increasing from '50 nm–Sub' to '150 nm–Sub'. The full width at half maximum (FWHM) is ∼12° for '150 nm–Sub'. However, for '250 nm–Sub' the (1 1 1) spot is considerably broader with a FWHM of ∼40°. This indicates the contribution of a different mechanism to growth between thickness of 150 and 250 nm. To investigate this further we subtracted each pattern by one step lower in thickness, e.g. 250–150 nm. This enables understanding the dominant growth mechanism or transitions assuming identical growth conditions for samples. This *incremental subtraction* is shown in the right column of figure 6. The 50–40 nm and 100–75 nm show a scatter pattern similar to ones obtained for our polycrystalline Py target material (not shown here), but with slightly higher intensity at the center. However, the 75–50 nm pattern shows a weaker scatter pattern and a very intense ⟨1 1 1⟩ spot at the center. This variation indicates a competition between the ⟨1 1 1⟩ perpendicular texture and equiaxed grain growth. In the 150–100 nm the pattern consist of an intense ⟨1 1 1⟩ spot at the center indicating the ⟨1 1 1⟩ fiber texture becoming completely dominant. There is also a faint ring at ∼70° which belongs to ⟨1 1 $\bar{1}$⟩ and is consistent with the ⟨1 1 1⟩ being perpendicular to the substrate. The 250–150 nm presents a more intense ring between 10–50° compared to the spot at the center. This might be due to knock-on deformation [19].

3.2.4. Magnetic properties. Figure 7 shows the hysteresis loops along the both easy and hard axis of the film induced by field assisted tilt deposition. It can be seen that for a wide range of thicknesses this method gives very well defined uniaxial anisotropy i.e. square easy axis with sharp switching and linear hard axis without hysteresis. The H_c shows no systematic change with thickness or grain size of the film. However, the 100 nm thick film presents a maximum H_c of 1.4 Oe. Miyazaki *et al* [25] reported such a maximum and explained it by the change in domain wall structure. For the case of Py it changes from Néel to crosstie and then to Bloch walls at about 50–60 and 90–100 nm, respectively [26, 27]. Along the hard axis, maximum H_k of 5.4 Oe was obtained for 10 nm thik film. As the film thickness increases, H_k drops and gives constant value of ∼3.4 Oe for thicknesses higher than 50 nm.

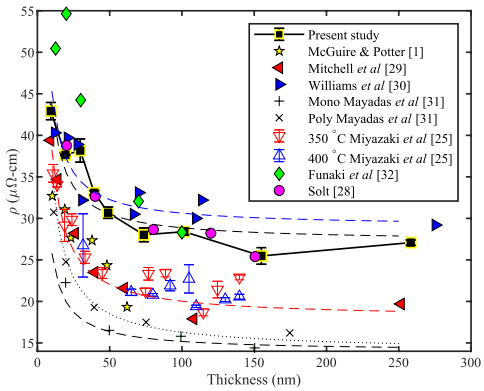

Figure 8. Variation resistivity with thickness in present study in comparison with previous results. The solid black line in our result is plotted to aid the eye. The dashed lines indicate fitting to Fuchs model to our result and to that of Mitchel *et al* [29], Williams *et al* [30] and single crystal films of Mayadas *et al* [31] while the dotted line indicates fitting Mayadas–Shatzkes models to the annealed polycrystalline films of Mayadas *et al* [31]. Our films were deposited at a 35° angle with respect to the substrate normal with assisting *in situ* magnetic field of 70 Oe at ∼12.8 rpm rotation speed.

Table 2. The film thickness, density and surface roughness obtained by fitting of the XRR results.

Sample	10	20	30	40	50	75	100	150	250
Thickness (nm)	10.49	21.47	29.63	41.41	50.59	75.49	103.62	157.07	259.78
Density (g cm^{-3})	8.41	8.65	8.65	8.58	8.63	8.63	8.63	8.63	8.65
Roughness (Å)	2	1.25	2	2.01	2	2.02	2	1.11	2

Table 3. Sample preparation condition in previous studies where T, H and t denote temperature, applied field and anneal time, respectively.

	Growth				Anneal				
	Rate (Å s^{-1})	Substrate	T (°C)	H (Oe)	T (°C)	H (Oe)	t (h)	ρ_0 ($\mu\Omega$ cm)	Reference
Evaporation	16	Glass	300	20	—	—	—	18	[29]
	1000	Glass	300	1200	—	—	—	28	[30]
	2.3	MgO	300	60	—	—	—	14	[31]
	2.3	MgO	25	60	300	—	2	14	[31]
	10	Glass	350–400	25	—	—	—	18	[25]
Sputter	5	Glass	25	0	150–450	500	1	27	[32]
	—	—	—	—	400	—	1	14.5	[1]
	1.16	SiO_2–Si	25	400	250	400	3	24	[28]

3.2.5. Magnetoresistance. Figure 8 shows the dependency of ρ_{ave} on the film thicknesses in comparison with other studies in the literature. These results are collected using different methods in a long time span and are obtained from samples with different preparation as summarized in table 3. It can be seen that we used a similar method, deposition rate (1.20 Å) and substrate to Solt [28]. As a result the resistivity values obtained in both experiments are in close agreement. It is worth mentioning that the samples in [28] were annealed for a few hours at 250°, which according to Miyazaki *et al* [25] has negligible effect on the microstructure. A similar trend and close agreement can be found in the resistivities of Mitchell *et al* [29] and Miyazaki *et al* [25]. Both used evaporation with nearly identical substrate temperature and deposition rate.

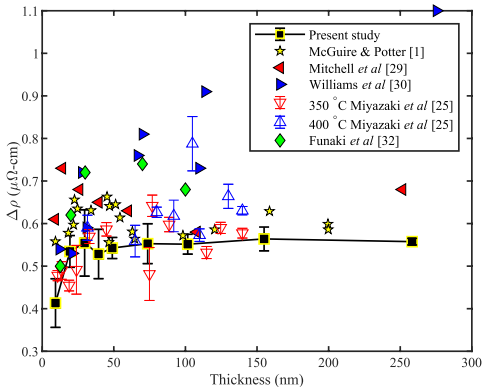

Figure 9. The change in $\Delta\rho$ with the film thickness in comparison with previous results. The solid black line in our result is plotted to aid the eye. Our films were deposited at a 35° angle with respect to the substrate normal with assisting *in situ* magnetic field of 70 Oe at ~12.8 rpm rotation speed.

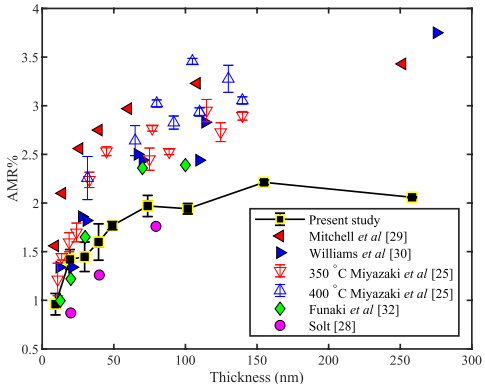

Figure 10. Variation of AMR% with the film thickness in comparison with previous results. The solid black line in our result is plotted to aid the eye. Our films were deposited at a 35° angle with respect to the substrate normal with assisting *in situ* magnetic field of 70 Oe at ~12.8 rpm rotation speed.

Furthermore an approximation of Fuchs' theory [33] (equation (8)) plotted in the figure with dashed lines.

$$\rho = \rho_0 \left(1 + \frac{3}{8}\frac{\lambda_0}{d}\right) \tag{8}$$

where ρ_0 and λ_0 are the bulk resistivity and mean free path of electrons, respectively. Mayadas *et al* [31] pointed out $\rho_0\lambda_0$ should be constant, e.g. equal to 31.5×10^{-6} $\mu\Omega$ cm^2 for Py, thus independent variation of parameters is restricted. The best fits for our films give ρ_0 of 27 $\mu\Omega$ cm considerably higher than the bulk value of 14.5 $\mu\Omega$ cm reported by Bozorth [34]. While results of single crystal films by Mayadas *et al* [31] present a reasonable value of 14 $\mu\Omega$ cm for the bulk. This difference indicates that the simple surface

scattering assumption in the Fuchs' model is not satisfied in polycrystalline films.

For polycrystalline films, Mayadas and Shatzkes [35] developed the following model to take into account grain boundary scattering:

$$\frac{\rho_0}{\rho} = 3\left[\frac{1}{3} - \frac{\alpha}{2} + \alpha^2 - \alpha^3 \ln\left(1 + \frac{1}{\alpha}\right)\right] \quad (9)$$

$$\alpha = \frac{\lambda_0}{d}\frac{\Re}{1-\Re} \quad (10)$$

where $\Re$ is the coefficient of grain boundary reflection.

The Mayadas–Shatzkes model is also plotted in figure 8 using a dotted line, which perfectly fits ρ values of polycrystalline films reported by Mayadas *et al* [31]. However, they annealed their samples in a way that the grain size is equal to or bigger than the film thickness. They also mentioned the as deposited polycrystalline film cannot be fitted with this model since λ_0 might change drastically with the thickness. This issue is also limiting for ultra-thin films when contribution of surface and grain boundary scattering to excess resistivity is the same [31].

It can be seen in figure 8 there are some abrupt changes in the all data sets (e.g. 30, 70 and 150 nm in our result and 40 nm for McGuire and Potter) which cannot be explained by surface and grain boundary scattering. We found strong correlation between growth of $\langle 1\,1\,1\rangle$ texture and deviation of ρ_{iso} from Fuchs' model. For instance 75–50 and 150–100 nm in which growth of $\langle 1\,1\,1\rangle$ texture is dominant (see figure 6 right column) present more deviation from Fuchs' model and lower resistivity.

Figure 9 shows the change in $\Delta\rho$ versus film thickness in comparison with previous studies. Mitchell *et al* [29] and McGuire and Potter [1] claimed that $\Delta\rho$ is independent of the film thickness. While Miyazaki *et al* [25] concluded that there was a slight increase in $\Delta\rho$ with the film thickness and Williams *et al* [30] showed a strong increase in $\Delta\rho$ with the film thickness. On the other hand Funaki *et al* [32] reported a maximum $\Delta\rho$ around 50 nm for as prepared Py which drops afterwards. However our result shows the $\Delta\rho$ increase with thickness to a maximum at 30 nm and becomes constant afterward. The sharp increase in $\Delta\rho$ between 10–30 nm seems to apear in the all data sets including Mitchell *et al* [29] and McGuire and Potter [1]. This corresponds to the range of thicknesses when there is competition between different grains with different orientations in the case of an amorphous substrates such as SiO_2 [19]. While for thicker films the dominating orientations are determined by the growth conditions and the result of different studies become more scattered.

The AMR change with the thickness is shown in figure 10 which also contains previous results for comparison. McGuire and Potter [1] believed since $\Delta\rho$ is independent of the film thickness the AMR ratio only depends on ρ_{ave}. Thus, a saturation behaviour with the film thickness is expected for AMR as ρ_{ave} saturates around the bulk value at higher thicknesses. While Williams *et al* [30] reported an increasing trend with increase in thickness which is due to their increased $\Delta\rho$. The rest of the data sets, however, show a saturation in AMR as their $\Delta\rho$ does not grow continuously with the thickness. It is also clear that data sets with lower ρ_{ave} present higher AMR here which also indicates the importance of ρ_{ave}. Thus, for the increased AMR ratio both high $\Delta\rho$ and low ρ_{ave} is required.

4. Conclusions

In conclusion, it is shown that the extended vdP method is a sensitive way to obtain anisotropic resistivity in thin ferromagnetic films. This includes AMR measurements which require magnetization saturation parallel and perpendicular to the current direction. In comparison with the conventional way of using Hall-bars, the vdP method presents more consistency along the hard and easy axis of the film. Thus the AMR value measured by the extended vdP method is independent of the initial magnetization direction in the film. Also variation of microstructure and AMR with the thickness of Py films was studied. It is shown that the resistivity of the films obtained by the vdP method strongly correlates with the film thickness, grain size and texture. The AMR ratio increases at first with the film thickness and then saturates just below 100 nm thickness, as both $\Delta\rho$ and ρ_{ave} independently saturate, their ratio thus remaining fixed. The $\Delta\rho$ and ρ_{ave} seems to be affected by microstructure obtained in the preparation method.

Acknowledgments

This work was supported by the Icelandic Research Fund Grant No. 120002023.

ORCID iDs

Movaffaq Kateb https://orcid.org/0000-0002-2518-3988
Snorri Ingvarsson https://orcid.org/0000-0001-8397-8917

References

[1] McGuire T and Potter R 1975 *IEEE Trans. Magn.* **11** 1018–38
[2] Chikazumi S 1950 *J. Phys. Soc. Japan* **5** 333–8
[3] Bozorth R M 1946 *Phys. Rev.* **70** 923
[4] Van der Pauw L 1958 *Philips Tech. Rev.* **20** 220–4
[5] Van der Pauw L 1958 *Philips Res. Rep.* **13** 1–9
[6] Price W 1973 *Solid-State Electron.* **16** 753–62
[7] Smith D O 1959 *J. Appl. Phys.* **30** S264–5
[8] Cullity B D and Graham C D 2011 *Introduction to Magnetic Materials* (New York: Wiley) (https://doi.org/10.1002/9780470386323)
[9] Sun Y, Sullivan C R, Li W, Kopp D, Johnson F and Taylor S T 2007 *IEEE Trans. Magn.* **43** 4060–3
[10] Solovev P, Izotov A and Belyaev B 2017 *J. Magn. Magn. Mater.* **429** 45–51
[11] Zou P, Yu W and Bain J A 2002 *IEEE Trans. Magn.* **38** 3501–20
[12] Phuoc N N, Tee Soh W, Chai G and Ong C 2013 *J. Appl. Phys.* **113** 073902

[13] Oliveira A B D, Rodriguez-Suarez R, Michea S, Vega H, Azevedo A, Rezende S M, Aliaga C and Denardin J 2014 *J. Appl. Phys.* **116** 033910
[14] Kateb M and Ingvarsson S 2017 Thickness-dependent magnetic and magnetoresistance properties of permalloy prepared by field assisted tilt sputtering *IEEE Sensors Applications Symp.* pp 1–5
[15] Li Z and Zhang S 2004 *Phys. Rev.* B **70** 024417
[16] Li X, Sun X, Wang J and Liu Q 2015 *J. Magn. Magn. Mater.* **377** 142–6
[17] McMichael R D, Lee C G, Bonevich J E, Chen P J, Miller W and Egelhoff W F 2000 *J. Appl. Phys.* **88** 5296–9
[18] Parratt L G 1954 *Phys. Rev.* **95** 359–69
[19] Mahieu S, Ghekiere P, Depla D and De Gryse R 2006 *Thin Solid Films* **515** 1229–49
[20] Jacobsen E I 2016 High frequency magnetic field sensors *Master's Thesis* Science Institute, University of Iceland (http://hdl.handle.net/1946/24952)
[21] Dzhumaliev A, Nikulin Y V and Filimonov Y A 2016 *Phys. Solid State* **58** 1053–7
[22] Neerinck D G, De Veirman A E M, Slangen M H J, Rijks T G S M and Kools J C S 1996 *Thin Solid Films* **280** 136–41
[23] Rijks T G, Lenczowski S, Coehoorn R and De Jonge W 1997 *Phys. Rev.* B **56** 362
[24] Katada H, Shimatsu T, Watanabe H, Watanabe I, Muraoka H, Nakamura Y and Sugita Y 2002 *IEEE Trans. Magn.* **38** 2664–6
[25] Miyazaki T, Ajima T and Sato F 1989 *J. Magn. Magn. Mater.* **81** 86–90
[26] Ahn K Y 1966 *J. Appl. Phys.* **37** 1481–2
[27] Freedman J 1969 *IEEE Trans. Magn.* **5** 752–64
[28] Solt K 1985 *Thin Solid Films* **125** 251–6
[29] Mitchell E, Haukaas H, Bale H and Streeper J 1964 *J. Appl. Phys.* **35** 2604–8
[30] Williams F C Jr and Mitchell E 1968 *Japan. J. Appl. Phys.* **7** 739
[31] Mayadas A F, Janak J F and Gangulee A 1974 *J. Appl. Phys.* **45** 2780–1
[32] Funaki H, Okamoto S, Kitakami O and Shimada Y 1994 *Japan. J. Appl. Phys.* **33** L1304
[33] Fuchs K 1938 *Mathematical Proceedings of the Cambridge Philosophical Society* vol 34 (Cambridge: Cambridge University Press) pp 100–8
[34] Bozorth R M 1951 *Ferromagnetism* (New York: Van Nostrand) p 870
[35] Mayadas A and Shatzkes M 1970 *Phys. Rev.* B **1** 1382

Paper IV

Effect of atomic ordering on the magnetic anisotropy of single crystal $Ni_{80}Fe_{20}$

M. Kateb, J. T. Gudmundsson and S. Ingvarsson 2019

AIP Advances 9 (3) 2019, 035308 (5pp)

AIP Advances ARTICLE scitation.org/journal/adv

Effect of atomic ordering on the magnetic anisotropy of single crystal $Ni_{80}Fe_{20}$

Cite as: AIP Advances 9, 035308 (2019); doi: 10.1063/1.5088602
Submitted: 11 January 2019 • Accepted: 26 February 2019 •
Published Online: 8 March 2019

Movaffaq Kateb,[1,a] Jon Tomas Gudmundsson,[1,2,b] and Snorri Ingvarsson[1,c]

AFFILIATIONS

[1]Science Institute, University of Iceland, Dunhaga 3, IS-107 Reykjavik, Iceland
[2]Department of Space and Plasma Physics, School of Electrical Engineering and Computer Science, KTH–Royal Institute of Technology, SE-100 44 Stockholm, Sweden

[a]Electronic mail: mkk4@hi.is
[b]Electronic mail: tumi@hi.is
[c]Electronic mail: sthi@hi.is

ABSTRACT

We investigate the effect of atomic ordering on the magnetic anisotropy of $Ni_{80}Fe_{20}$ at.% (Py). To this end, Py films were grown epitaxially on MgO(001) using dc magnetron sputtering (dcMS) and high power impulse magnetron sputtering (HiPIMS). Aside from twin boundaries observed in the latter case, both methods present high quality single crystals with cube-on-cube epitaxial relationship as verified by the polar mapping of important crystal planes. However, X-ray diffraction results indicate higher order for the dcMS deposited film towards $L1_2$ Ni_3Fe superlattice. This difference can be understood by the very high deposition rate of HiPIMS during each pulse which suppresses adatom mobility and ordering. We show that the dcMS deposited film presents biaxial anisotropy while HiPIMS deposition gives well defined uniaxial anisotropy. Thus, higher order achieved in the dcMS deposition behaves as predicted by magnetocrystalline anisotropy i.e. easy axis along the [111] direction that forced in the plane along the [110] direction due to shape anisotropy. The uniaxial behaviour in HiPIMS deposited film then can be explained by pair ordering or more recent localized composition non-uniformity theories. Further, we studied magnetoresistance of the films along the [100] directions using an extended van der Pauw method. We find that the electrical resistivities of the dcMS deposited film are lower than in their HiPIMS counterparts verifying the higher order in the dcMS case.

I. INTRODUCTION

The phenomenon of *uniaxial anisotropy* in permalloy $Ni_{80}Fe_{20}$ at.% (Py) films and its correlation with microstructure has attracted considerable scientific and industrial interest for decades. The proposed explanations for uniaxial anisotropy include oriented defects and oxides,[1,2] directional ordering of Fe/Ni atoms pairs,[3] shape anisotropy of an elongated ordered phase,[4] composition variation between grains[5] and more recently, localized composition non-uniformity.[6] No one of these can account for all instances of uniaxial anisotropy in the Py system, and one or more could contribute simultaneously.

Epitaxial, single crystal Py films have a perfect lattice, while the arrangement of Ni and Fe atoms may contain varying degrees of order. Among the explanations above, only the pair ordering and the localized composition non-uniformity are applicable in such a case. Py has vanishingly small magnetocrystalline anisotropy and magnetostriction, and low coercivity, but extremely large magnetic permeability.[7,8] This makes it a unique system in which to study e.g. induced uniaxial anisotropy. Single crystal Py films have been deposited epitaxially by numerous techniques, including thermal evaporation,[7,9,10] electron beam evaporation,[11] molecular beam epitaxy (MBE),[12–14] ion beam sputtering,[15,16] rf magnetron sputtering,[17,18] dc magnetron sputtering,[19] and pulsed laser deposition.[20] Most of these deposition methods have resulted in a single crystal Py(001) film on MgO(001) with biaxial anisotropy in the plane, and the easy directions being [110] or [100]. Unfortunately, studies that focused on the growth of single crystal Py did not discuss the effect of ordering at all. Most of these studies used a low deposition rate, which normally results in higher order. On the other hand, the study

AIP Advances ARTICLE scitation.org/journal/adv

of atomic order is limited to annealing a quenched specimen at about 500 °C for a very long time.[3,21–23]

Several groups have shown that an increase in atomic order results in deterioration of the anisotropy constant K_1.[3,22,24,25] Uniaxial anisotropy can be induced in single crystal Py by applying an *in-situ* magnetic field during deposition,[7,15,16] or by post annealing[26] in magnetic field. It has been shown that magnetic field induced anisotropy strongly depends on the crystal orientation of the Py for both deposition and annealing in a magnetic field[7,27] i.e. it is most efficient along the ⟨111⟩ direction, less so along the ⟨110⟩ direction and least along the ⟨100⟩ direction.

Another method of inducing uniaxial anisotropy is deposition under an angle with respect to the substrate normal. We have shown that deposition under a 35° angle is more effective than applying a 70 Oe *in-situ* magnetic field when depositing polycrystalline films.[28,29] We have also demonstrated growth of polycrystalline Py films under an angle using high power impulse magnetron sputtering (HiPIMS) and compared with films deposited by conventional dc magnetron sputtering (dcMS).[30] During HiPIMS deposition high power pulses of low frequency and low duty cycle are applied to a magnetron target which results in highly ionized sputtered material.[31] The HiPIMS discharge provides a highly ionized flux of the metallic species and the averaged ion energy is significantly higher in the HiPIMS discharge than in dcMS discharge and this energetic metallic ions are created during the active phase of the discharge pulse.[32–34] For both methods, deposition under an angle with respect to the substrate induces very well-defined uniaxial anisotropy in the film. Schuhl *et al.*[35] showed that tilt deposition breaks the symmetry between two in-plane easy axes, appearing as a stepped easy axis magnetization loop along the flux direction. However the method of inducing uniaxial anisotropy using tilt deposition of a single crystal Py has not been studied so far. In this work we demonstrate the epitaxial growth of *single crystal* Py films on MgO(001) substrates, by HiPIMS and by dcMS both deposited under an incident angle of 35°. We study the effect of the two above mentioned sputtering methods, whose adatom energy differs by order(s) of magnitude, on the structure, order and magnetic anisotropy of the films. It might be tempting to think that the high adatom energy involved in HiPIMS would cause severe structural damage, but there appear to be only very subtle structural disparities, while the ordering and magnetic anisotropy, however, are vastly different.

II. METHOD

The substrates were single-side polished single crystalline MgO(001) with surface roughness < 5 Å, and with lateral dimension of 10×10 mm^2 and 0.5 mm thickness (Latech Scientific Supply Pte. Ltd.). The MgO substrates were used as received without any cleaning but were baked for an hour at 400 °C in vacuum for dehydration. The Py thin films were deposited in a custom built ultra-high vacuum magnetron sputter chamber with a base pressure of < 5×10^{-7} Pa. The deposition was performed with argon of 99.999 % purity as the working gas at 0.33 Pa pressure using $Ni_{80}Fe_{20}$ target of 75 mm in diameter and 1.5 mm thickness. During deposition, the substrates were rotated 360° back and forth at ~12.8 rpm with 300 ms stop in between. Further detail on our deposition geometry can be found elsewhere.[28–30]

For dcMS deposition a dc power supply (MDX 500, Advanced Energy) was used and the power was maintained at 150 W. For HiPIMS deposition, the power was supplied by a SPIK1000A pulser unit (Melec GmbH) operating in the unipolar negative mode at constant voltage, which in turn was charged by a dc power supply (ADL GS30). The pulse length was 250 μs and the pulse repetition frequency was 100 Hz. The average power during HiPIMS deposition was maintain around 151 W. The HiPIMS deposition parameters were recorded by a home-made LabVIEW program communicating with the setup through high speed data acquisition (National Instruments).

X-ray diffractometry (XRD) was carried out using a X'pert PRO PANalitical diffractometer (Cu K_α, wavelength 0.15406 nm) mounted with a hybrid monochromator/mirror on the incident side and a 0.27° collimator on the diffracted side. A line focus was used with a beam width of approximately 1 mm. The film thickness, density and surface roughness was determined by low-angle X-ray reflectivity (XRR) measurements with an angular resolution of 0.005°. The data from the XRR measurements were fitted using a commercial X'pert reflectivity program.

For the (002) pole figure the $\theta - 2\theta$ was set to a corresponding peak obtained in the normal XRD. However, the (111) and (022) peaks do not appear in the normal XRD. To this end, first a rough pole scan was done according to $\theta - 2\theta$ found in the literature. This roughly gives the in-plane (ϕ) and out-of-plane (ψ) angles of those planes with respect to the film surface. Then we scan $\theta - 2\theta$ at the right ϕ and ψ to find each (111) and (022) peak. Finally, a more precise pole scan is made again at the new $\theta - 2\theta$ values. Obviously, the $\theta - 2\theta$ values reported in the literature might be slightly different than for our samples due to strain in the film and accuracy of calibration. The ψ was calibrated using the (002) peak of MgO normal to the substrate. In a similar way, the narrow MgO(200) peak in-plane of the substrate was utilized for calibration of ϕ.

To obtain hysteresis loops, we use a homebuilt high sensitivity magneto-optical Kerr effect (MOKE) looper with HeNe laser light source. We used variable steps in the magnetic field i.e. 0.1 Oe steps around transitions of the easy direction, 0.5 Oe steps for the hard axis and before transitions of the easy direction and 1 Oe steps for higher field at saturation.

For the anisotropic magnetoresistance (AMR) measurements we utilized Price[36] extension to van der Pauw (vdP)[37,38] method. We have already shown that the vdP measurement is more reliable in the AMR measurements since it is less geometry dependent compared to conventional Hall-bar method.[29] Originally, vdP was developed for determining isotropic resistivity and ordinary Hall mobility of uniform and continuous thin films of arbitrary shape and has been used extensively for semiconductor characterization. In the vdP method, four small contacts must be placed on the sample perimeter e.g. as illustrated in Fig. 1. The measured resistances should satisfy vdP equation[38]

$$\exp\left(-\frac{\pi d}{\rho_{\mathrm{iso}}}R_{\mathrm{AB,CD}}\right) + \exp\left(-\frac{\pi d}{\rho_{\mathrm{iso}}}R_{\mathrm{AD,CB}}\right) = 1 \qquad (1)$$

where ρ_{iso} is the isotropic resistivity and d is the film thickness. The resistance $R_{\mathrm{AB,CD}}$ is measured by forcing current through the path AB and picking up the voltage at the opposite side between CD and $R_{\mathrm{AD,CB}}$ is similarly defined. Note that Eq. (1) is independent of sample shape and distances between contacts. This behavior is a direct

AIP Advances ARTICLE scitation.org/journal/adv

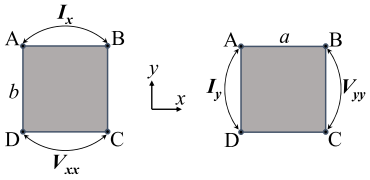

FIG. 1. Schematic illustration of set of measurements in vdP method.

result of conformal mapping i.e. a sample has been mapped upon a semi-infinite half-plane with contacts along the edge in which the contact distances cancel out.

It has been shown that the vdP method can be extended to the case of anisotropic films if two of three principle resistivity axis are in the film plane while the 3rd is perpendicular. In that case, ρ_{iso} obtained from Eq. (1) stands for the geometric mean of the in-plane principle resistivities i.e. $\rho_{iso} = \sqrt{\rho_1\rho_2}$.[39,40] In principle, the vdP method is based on conformal mapping and thus it should remain valid if an anisotropic medium with lateral dimensions of $a \times b$ mapped into an isotropic one with new dimensions e.g. $a \times b'$. In practice one can make a rectangular sample with sample sides parallel to the principle resistivities.[36,39] Assuming the principle resistivities are aligned with x and y directions in Fig. 1, the principle resistivities ρ_x and ρ_y can be obtained from Price's[36] extension, as

$$\sqrt{\frac{\rho_x}{\rho_y}} = -\frac{b}{\pi a}\ln\left(\tanh\left[\frac{\pi d R_{AD,CB}}{16\rho_{iso}}\right]\right) \tag{2}$$

where a and b are the side lengths of a rectangular sample and $R_{AD,CB}$ is resistance along the b sides as described above.

Eq. (2) yields to the ratio of principle resistivities and the individual values can subsequently be obtained by

$$\rho_x = \rho_{iso}\sqrt{\frac{\rho_x}{\rho_y}} \tag{3}$$

and

$$\rho_y = \rho_{iso}\left(\sqrt{\frac{\rho_x}{\rho_y}}\right)^{-1} \tag{4}$$

For the AMR measurement according to Bozorth's[41] notation one must measure resistivity with saturated magnetization parallel ($\rho_\parallel$) and perpendicular ($\rho_\perp$) to current direction. The AMR ratio is given by[42]

$$\mathrm{AMR} = \frac{\Delta\rho}{\rho_{ave}} = \frac{\rho_\parallel - \rho_\perp}{\frac{1}{3}\rho_\parallel + \frac{2}{3}\rho_\perp} \tag{5}$$

Assuming the x-axis being the current direction, the AMR response can be presented as ρ_x which only depends on the direction of saturated magnetization

$$\rho_x = \rho_\parallel + \Delta\rho\cos^2\phi \tag{6}$$

here ϕ stands for angle between current (x) and saturated magnetization direction.

It is worth noting that Eq. (6) states that the resistivity is only dependent on ϕ, not on the initial magnetization direction of the films. This is because $\rho_\parallel$ and $\rho_\perp$ are measured at saturation magnetization where the entire domains are assumed to be aligned to external magnetic field.[41]

III. RESULTS AND DISCUSSION

A. HiPIMS discharge waveforms

The discharge current and voltage waveform are a characteristic of the HiPIMS process, which provides important information on both the instrument (the pulser unit) and the physics of ionization. Fig. 2 shows the current and voltage waveforms of the HiPIMS discharge recorded during deposition. It can be seen that a nearly rectangular voltage pulse of 250 μs length was applied to the cathode target. The oscillations at the beginning and after ending the voltage pulse initiate from internal inductance of the power supply, which creates a resonant circuit along with the capacitance of the cathode target and the parasitic capacitance of the cables. There is also a local minimum corresponding to the current rise at 80 μs.

The discharge current is initiated about 70 μs into the voltage pulse. The discharge current peaks at 110 μs into the pulse and then decays until it is cut-off. As described by Lundin *et al.*[43] the current waveforms can be divided into three distinct regions. (I) A strong gas compression due to the rapid accumulation of sputtered flux as plasma ignites which give rise to current to the peak value. This is followed by (II) rarefaction i.e. collision of sputter flux with the working gas which results in heating and expansion of the working gas and consequently current decay. More recently, it has been shown that the later mechanism is dominating for rarefaction at higher pressures and ionization loss is dominating otherwise.[44] (III) A steady state plasma till the end of the voltage pulse which gives a relatively flat current plateau.

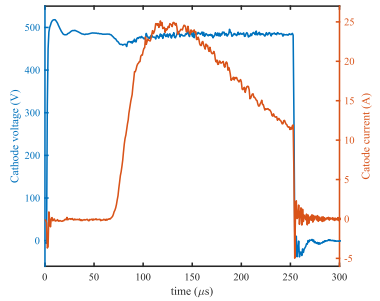

FIG. 2. The discharge current and voltage waveforms at 0.33 Pa with the pulse frequency of 100 Hz and pulse length 250 μs.

AIP Advances ARTICLE scitation.org/journal/adv

It has been shown that increased pressures can prolong current decay time to the end of pulse and eliminate plateau regions.[43] We believe this is highly unlikely the case in Fig. 2. We have already shown that 0.33 Pa is in vicinity of minimum pressure i.e. lower pressures results in non-linear increase of delay time for current onset and increase time from current onset to peak current which is nearly constant at higher pressures.[50] Thus pressure is low enough to capture the third stage of the current evolution but, the short pulse length here does not allow it to appear.

It is worth mentioning that, although we have tried to maintain the HiPIMS average power the same as dcMS power (at 150 W), the HiPIMS pulse voltage and peak current (465 V and 25 A) are well above dcMS counterparts (321 V and 463 mA).

B. Microstructure

1. XRR

Values of film thickness, film density and surface roughness obtained from fitting of the measured XRR curves are shown in Table I. The surface roughnesses obtained here are slightly lower than previously reported values using dcMS.[19] The mass density of HiPIMS deposited film is higher than for the dcMS deposited counterpart. It is somewhat lower than for polycrystalline films deposited by dcMS and HiPIMS (8.7 g/cm^3)[30] and the bulk density of 8.73 g/cm^3 (Ref. 45 (p. 2-6)). Accounting for the epitaxial strain the densities here are within a reasonable range.

It is worth mentioning that, during each HiPIMS pulse, the deposition rate is much higher during the active discharge phase than for dsMS i.e. more than 50 times accounting 250 μs pulse width and 100 Hz frequency.

2. XRD

Permalloy has a fcc structure while both metastable hcp[14,17,46] and bcc[8,47,48] Py phases have been reported in ultrathin films. Fig. 3 illustrates the symmetric $\theta - 2\theta$ XRD pattern of the epitaxial films obtained by both deposition methods. In the out-of-plane XRD, fcc (002) peak is the only detectable Py peak. This indicates that the (002) planes of Py are very well aligned to that of the MgO substrate i.e. Py(001) ∥ MgO(001). Similar results were obtained by measurement in-plane of epitaxial films ($\psi = 90°$) along the [100] directions of MgO i.e. normal to substrate edges. Furthermore, in-plane measurements along the ⟨110⟩ direction of MgO (substrate diagonals) show (220) peaks from both the MgO substrate and the Py film. These indicate a orientation relationship of Py [100] ∥ MgO [100] and Py [110] ∥ MgO [110] i.e. the [100] and [110] directions of Py are fully aligned with those of the MgO substrate. Thus, in spite of the large lattice mismatch (15.84%), high quality single crystal Py(a_{Py} = 3.548 Å) film can be established on a MgO(a_{MgO} = 4.212 Å) substrate for both deposition techniques. Furthermore, we compared the in-plane peaks along the ⟨100⟩ and ⟨010⟩ directions (not shown here) and detected no difference in lattice parameter even with a precise scan i.e. angular resolution 0.0001° and 10 s counting

TABLE I. Values of film thickness, film density and surface roughness obtained by fitting the XRR measurement results.

Growth technique	Thickness (nm)	Deposition rate (Å/s)	Density (g/cm^3)	Roughness (Å)
HiPIMS	45.74	0.97	8.38	6.75
dcMS	37.50	1.50	8.32	6.33

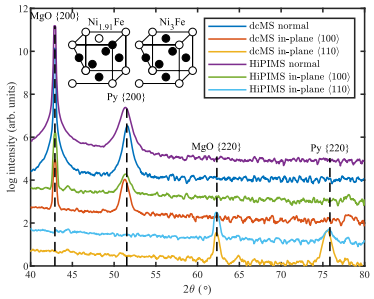

FIG. 3. The symmetric XRD pattern of the epitaxial films deposited by HiPIMS (right) and dcMS (left). The vertical dashed lines show the peak position of bulk Py and MgO. The curves are shifted manually for clarity.

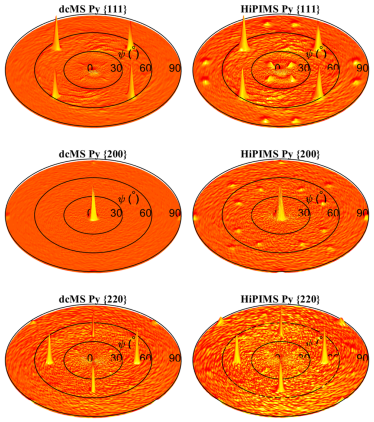

FIG. 4. The pole figures obtained for Py {111}, {200} and {220} planes of epitaxial films deposited by HiPIMS and dcMS. The height represents normalized log intensity in arbitrary units.

AIP Advances ARTICLE scitation.org/journal/adv

time. This means we observed identical in-plane strain along the [100] directions in both of the films.

In the dcMS case, the Py(002) peak shows a slight shift towards higher angles in the normal XRD scan. This is accompanied by the shift of in-plane peaks towards smaller angles. Thus, tensile strain at the film-substrate interface generates slight compression normal to the film plane.[49] However, in the HiPIMS case, both the in-plane *and* out-of-plane peaks are shifted towards smaller angles. This would indicate tensile strain in all tree dimension that is impossible. However, we attribute the shift of (002) peak in the HiPIMS case to departure from the $L1_2$ Ni_3Fe superlattice.[50] As pointed out by O'Handley (Ref. 51 (p. 548)), the Ni_3Fe phase exists in either a disordered or well ordered structure. It has been shown that an ordered Ni_3Fe phase can be detected as a shift of XRD peaks towards larger angles[3,23,51] and narrower peaks.[21,23] In addition, the intensity of XRD peaks is expected to increase with the higher order.[51] (p. 549) All these conditions can be observed in our dcMS deposited film, indicating that it is more ordered than its HiPIMS counterpart. The more disordered arrangement in the HiPIMS deposition can be attributed to the high deposition rate during each pulse which suppresses adatom mobility.

3. Pole figures

Fig. 4 illustrates pole figures for the main Py planes of our epitaxial films. In the {200} pole figure, there is an intense spot at $\psi = 0$ that verifies that the (002) plane is lying parallel to the substrate i.e. epitaxial relationship of Py(001) ‖ MgO(001) for both dcMS and HiPIMS deposited films. There is also a weak spot with four-fold symmetry at $\psi = 90^\circ$ due to in-plane diffraction of {200} planes parallel to substrate edges in both films. This indicates there are Py {100} planes parallel to the substrate edges i.e. Py[100] ‖ MgO[100]. The {220} pole figures, also depict four-fold symmetry of {220} planes at ψ angle of 45 and 90° as expected from symmetry in a cubic single crystal for both films. In both of the {111} pole figures, there is a four-fold spot at $\phi = 45^\circ$ and $\psi = 54.74^\circ$ which is in agreement with the angle between (002) and {111} planes. However, compared to the (002) spots the {111} and {220} planes are slightly elongated radially, along the ψ axis. This indicates a lattice constant expanded in-plane of the substrate for both films, in agreement with shift observed in the in-plane XRDs (cf. Fig. 3). The FWHM of the spots are always narrower for the dcMS deposited epitaxial film indicating higher order in this case.

The extra dots that appear in the {111} pole figure of the HiPIMS deposited film belong to twin boundaries as have also been reported for epitaxially deposited Cu using thermal evaporation[52] and HiPIMS.[53] The existence of twin boundaries in the Py is a signature of high deposition rate which has been observed previously in evaporated[9,54] and electro-deposited[5] films and studied in detail using TEM.[54–56] It can be seen that these dots at 23° also appear in the dcMS deposited film but with very small intensity. This indicates that the fraction of twin boundaries is much lower in the dcMS deposited film. In addition, there are three spots with four-fold symmetry in the {200} pole figure of the HiPIMS deposited film which do not appear in the dcMS counterpart. The three dot pattern in the {200} pole figure has been characterized as an auxiliary sign of twin boundaries in the film.[53] It is worth noting that these extra dots in both {200} and {111} plane were characterized by a $\theta - 2\theta$ scan (not shown here) to make sure they belong to the Py film.

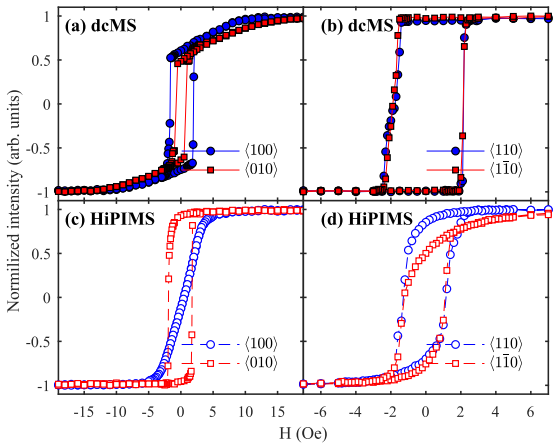

FIG. 5. The average hysteresis loops of the epitaxial films obtained by MOKE measurements along the [100] and [110] directions of the epitaxial Py films.

AIP Advances ARTICLE scitation.org/journal/adv

C. Magnetic properties

Fig. 5 compares the results of in-plane MOKE measurements along the [100] and [110] directions of both the epitaxial films. Fig. 5(a–b) indicate a biaxial behaviour in the dcMS deposited film consisting of two easy axes along the [110] directions with H_c of ~2 Oe. This is consistent with the ⟨111⟩ direction being the easy direction of the Py crystal and the magnetization being forced in-plane along the ⟨110⟩ directions due to shape anisotropy.[9,57] Along the [100] directions the MOKE response is relatively hard i.e. open hysteresis with a gradual saturation outside the hysteresis. The gradual saturation can be explained by an out-of-plane component of the magnetization.[58] In polycrystalline films, the out-of-plane element of magnetization increases with increase in the film thickness[59,60] and it gives perpendicular anisotropy at trans-critical thicknesses.[1,2,61] In single crystal films, however, it appears that an out-of-plane component of the magnetization is generally the case.[12,19,62]

Fig. 5(a) also shows that the ⟨100⟩ and ⟨010⟩ directions are not completely equivalent for our dcMS deposited film. The ⟨100⟩ direction presents larger coercivity (~2 Oe) and saturates at 12 Oe but the ⟨010⟩ direction gives ~1 Oe coercivity and saturates at 15 – 18 Oe. This difference arises from the fact that ⟨100⟩ is the direction of sputter flux during the 300 ms stop time while reversing the rotation. Such a short time is enough to define uniaxial anisotropy in the polycrystalline film using both dcMS and HiPIMS.[30] However, it appears that for the epitaxial film deposited by dcMS, our deposition geometry is not enough to induce uniaxial anisotropy along the [100] direction in agreement with the previous study of Schuhl *et al.*[35]

As shown in Fig. 5(c–d) the HiPIMS deposited epitaxial film shows very well-defined uniaxial anisotropy indicated by a linear hard axis trace without hysteresis and slightly rounded easy axis loop along the [100] directions. The anisotropy field (H_k) of the HiPIMS epitaxial film is 3.5 Oe, i.e. much lower than the values observed for polycrystalline films deposited by HiPIMS on Si/SiO_2 (11 – 14.5 Oe).[30] However the coercivity (H_c) of 1.8 Oe here is very close to that of polycrystalline films i.e. 2 – 2.7 Oe. We have shown that in polycrystalline films the H_c depends on the film density and increases as the film density drops.[30] In principle the H_c of a film depends on the domain boundary structure which has been proved to be dependent on the film thickness.[63] However, since the grain size changes with the film thickness, it is a common mistake to correlate H_c with the grain size. We have shown that for a range of film thicknesses (10 – 250 nm) the grain size changes continuously while H_c only changes with the domain wall transition i.e. Néel to Bloch to cross-tie.[28]

A question that might arise here is what makes the HiPIMS deposited epitaxial film present uniaxial anisotropy. It has been shown by several groups that formation of ordered Ni_3Fe results in lower uniaxial anisotropy constant (K_1).[3,22,24,25,27] According to both pair ordering[3] and localized composition non-uniformity[6] theories, uniaxial anisotropy is not expected for a highly symmetric Ni_3Fe. While in the case of HiPIMS deposited film, lower order results in uniaxial anisotropy.

D. Transport properties

Fig. 6 shows the AMR response of epitaxial films to the rotation of 24 Oe in-plane saturated magnetization. This field is large enough to saturate both films in any direction. The θ here stands for angle between applied magnetic field and the ⟨100⟩ direction of films and should not to be confused with the ϕ in Eq. (6) i.e. the angle between current direction and magnetic field. The result of Eq. (6) is also plotted for comparison as indicated by the black line. Even though, the dcMS deposited film is thinner than the HiPIMS counterpart, the resistivities in the dcMS case are all lower than the HiPIMS ones. This behaviour is in contradiction with the Fuchs model[64] which predicts lower resistivity for thicker films. It can be explained in terms of higher Ni_3Fe order achieved in the dcMS deposited film. It has been shown previously that the resistivity depends on the order and decreases upon increase in Ni_3Fe order.[22]

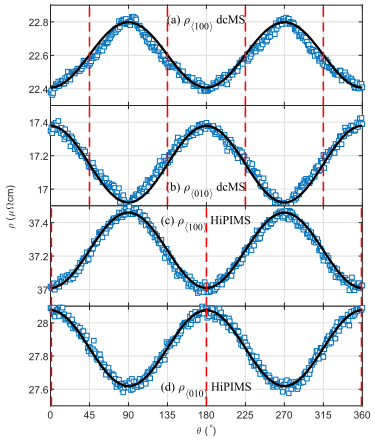

FIG. 6. The AMR obtained by resistivity measurements along the [100] directions of Py films deposited by (a – b) dcMS and (c – d) HiPIMS during rotation of 24 Oe magnetic field. The θ here stands for angle of in-plane magnetization with the ⟨100⟩ direction. The black lines indicate the result of fitting with Eq. (6). The vertical dashed lines indicate the direction of easy axes.

It can be seen that the AMR response of the epitaxial film deposited with HiPIMS conforms better with Eq. (6) than its dcMS counterpart. In the dcMS case, the deviation from Eq. (6) occurs at about 45 – 85°, 95 – 135° and so on. Since the deviation is symmetric around 90° (the ⟨010⟩ orientation) it is less likely associated with a pinning mechanism of some domains. Presumably, the deviation originates form switching some domains towards the easy axis at 45 and 135, 225 and 315° i.e. [110] orientations. This so-called quasi-static switching in single crystal Py has been studied using torque measurements, as characteristics of biaxial anisotropy.[9]

TABLE II. Summary of the AMR results of epitaxial films. (All resistivity values are in $\mu\Omega$-cm unit.)

Deposition method	Current direction	$\rho_{\parallel}$	$\rho_{\perp}$	$\Delta\rho$	ρ_{ave}	AMR (%)
		($\mu\Omega$-cm)				
dcMS	⟨100⟩	22.19	22.80	0.39	23.06	1.70
dcMS	⟨010⟩	16.92	16.46	0.46	16.77	2.74
HiPIMS	⟨100⟩	37.46	37.91	0.45	37.76	1.19
HiPIMS	⟨010⟩	27.16	27.62	0.46	27.47	1.67

The AMR values obtained by Eq. (5) along the ⟨100⟩ and ⟨010⟩ directions are summarized in Table II. We have recently shown that in polycrystalline films the AMR response is different along the hard and easy axis of the film.[29] It appears that the AMR response is always lower along the ⟨100⟩ (direction of flux) in the epitaxial films. It is also evident that higher order reduces resistivity and increases AMR.

IV. SUMMARY

In summary, we have deposited $Ni_{80}Fe_{20}$ (001) films by HiPIMS and dcMS. We have characterized them carefully with detailed X-ray measurements, finding only rather subtle structural differences. The pole figures display a signature of twin boundaries (stacking faults) in the HiPIMS deposited film and it appears to be slightly more strained or disordered, regarding dispersion of Ni and Fe atoms, than the dcMS deposited film. However, the differences in the magnetic properties of said films are vast. The dcMS deposited film has biaxial symmetry in the plane, with easy directions [110] as one might expect for a bulk fcc magnetic material (the ⟨111⟩ direction is out of plane and shape anisotropy forces magnetization into the plane of the film). The HiPIMS deposited film exhibits different magnetic symmetry, as it has uniaxial anisotropy with ⟨100⟩ as the easy direction. Furthermore, the film is magnetically soft and has an anisotropy field of only 3.5 Oe, which is lower than most results we have obtained for polycrystalline films. We attributed the uniaxial anisotropy to less ordered dispersion of Ni and Fe at the atomic level in the film deposited by HiPIMS due to high deposition rate of HiPIMS during the discharge pulse.

ACKNOWLEDGMENTS

The authors would like to acknowledge helpful comments and suggestions from Dr. Fridrik Magnus and Dr. Arni S. Ingason on the structure characterization. This work was partially supported by the Icelandic Research Fund (Rannis) Grant Nos. 196141, 130029 and 120002023, and the Swedish Government Agency for Innovation Systems (VINNOVA) contract No. 2014-04876.

REFERENCES

[1]Y. Sugita, H. Fujiwara, and T. Sato, "Critical thickness and perpendicular anisotropy of evaporated permalloy films with stripe domains," Appl. Phys. Lett. **10**, 229–231 (1967).
[2]H. Fujiwara and Y. Sugita, "Perpendicular anisotropy of evaporated magnetic films," IEEE Trans. Magn. **4**, 22–25 (1968).
[3]S. Chikazumi, "Ferromagnetic properties and superlattice formation of iron-nickel alloys (I)," J. Phys. Soc. Jpn. **5**, 327–333 (1950).
[4]S. Kaya, "Uniaxial anisotropy of a permalloy crystal," Rev. Modern Phys. **25**, 49 (1953).
[5]J. R. Kench and S. B. Schuldt, "Concerning the origin of uniaxial magnetic anisotropy in electrodeposited permalloy films," J. Appl. Phys. **41**, 3338–3346 (1970).
[6]D. C. M. Rodrigues, A. B. Klautau, A. Edström, J. Rusz, L. Nordström, M. Pereiro, B. Hjörvarsson, and O. Eriksson, "Magnetic anisotropy in permalloy: Hidden quantum mechanical features," Phys. Rev. B **97**, 224402 (2018).
[7]S. Chikazumi, "Epitaxial growth and magnetic properties of single-crystal films of iron, nickel, and permalloy," J. Appl. Phys. **32**, S81–S82 (1961).
[8]L. F. Yin, D. H. Wei, N. Lei, L. H. Zhou, C. S. Tian, G. S. Dong, X. F. Jin, L. P. Guo, Q. J. Jia, and R. Q. Wu, "Magnetocrystalline anisotropy in permalloy revisited," Phys. Rev. Lett. **97**, 067203 (2006).
[9]A. Yelon, O. Voegeli, and E. Pugh, "Switching properties of single-crystal Ni–Fe films," J. Appl. Phys. **36**, 101–108 (1965).
[10]D. S. Lo, "Magnetic switching in Ni–Fe single-crystal films," J. Appl. Phys. **37**, 3246–3258 (1966).
[11]O. Song, C. A. Ballentine, and R. C. O'Handley, "Giant surface magnetostriction in polycrystalline Ni and NiFe films," Appl. Phys. Lett. **64**, 2593–2595 (1994).
[12]J. C. A. Huang, T. E. Wang, C. C. Yu, Y. M. Hu, P. B. Lee, and M. S. Yang, "Epitaxial growth and characterization of (100) and (110) permalloy films," J. Cryst. Growth **171**, 442–446 (1997).
[13]T. Tanaka, M. Ohtake, F. Kirino, and M. Futamoto, "Preparation and characterization of NiFe epitaxial thin films grown on MgO(100) and $SrTiO_3$(100) single-crystal substrates," IEEE Trans. Magn. **45**, 2515–2518 (2009).
[14]T. Tanaka, M. Ohtake, F. Kirino, and M. Futamoto, "Microstructure of NiFe epitaxial thin films grown on MgO single-crystal substrates," IEEE Trans. Magn. **46**, 345–348 (2010).
[15]I. Hashim and H. A. Atwater, "In situ magnetic and structural analysis of epitaxial $Ni_{80}Fe_{20}$ thin films for spin-valve heterostructures," J. Appl. Phys. **75**, 6516–6518 (1994).
[16]I. Hashim, H. S. Joo, and H. A. Atwater, "Structural and magnetic properties of epitaxial $Ni_{80}Fe_{20}$ thin films on Cu/Si," Surf. Rev. Lett. **2**, 427–437 (1995).
[17]J. Higuchi, M. Ohtake, Y. Sato, F. Kirino, and M. Futamoto, "NiFe epitaxial films with hcp and fcc structures prepared on bcc-Cr underlayers," Thin Solid Films **519**, 8347–8350 (2011).
[18]T. Ohtani, T. Kawai, M. Ohtake, and M. Futamoto, "Influence of crystallographic orientation on the magnetic properties of NiFe, Co, and Ni epitaxial fcc films grown on single-crystal substrates," J. Korean Phys. Soc. **63**, 778–783 (2013).
[19]F. Michelini, L. Ressier, J. Degauque, P. Baules, A. Fert, J. Peyrade, and J. Bobo, "Permalloy thin films on MgO(001): Epitaxial growth and physical properties," J. Appl. Phys. **92**, 7337–7340 (2002).
[20]S. Rao, J. Prater, F. Wu, S. Nori, D. Kumar, and J. Narayan, "Integration of epitaxial permalloy on Si (100) through domain matching epitaxy paradigm," Curr. Opin. Solid State Mater. Sci. **18**, 1–5 (2014).
[21]A. Lutts and P. M. Gielen, "The order-disorder transformation in $FeNi_3$," Physica Status Solidi (B) **41**, K81–K84 (1970).
[22]K. Hausmann, U. Hofmann, and M. Wolf, "On the influence of atomic order in Ni_3Fe on the magnetic anisotropy and the electrical resistivity," Physica Status Solidi (A) **6**, 161–164 (1971).
[23]X. J. Wan, Y. X. Chen, A. P. Chen, and S. R. Yan, "The influence of atomic order on H_2-induced environmental embrittlement of Ni_3Fe intermetallics," Intermetallics **13**, 454–459 (2005).
[24]S. Tsukahara and H. Kawakatsu, "Magnetic domain pattern and magnetocrystalline anisotropy in epitaxially grown thin films of Fe, Ni, and Ni-Fe alloys," Journal of the Physical Society of Japan **21**, 313–325 (1966).
[25]R. M. Bozorth, *Ferromagnetism* (Wiley-VCH, New York, 1993), p. 571.
[26]R. M. Bozorth, "Theory of the heat treatment of magnetic materials," Physi. Rev. **46**, 232–233 (1934).
[27]S. Chikazumi, "Study of magnetic annealing on Ni_3Fe single crystal," J. Phys. Soc. Jpn. **11**, 551–558 (1956).

[28]M. Kateb and S. Ingvarsson, "Thickness-dependent magnetic and magnetoresistance properties of permalloy prepared by field assisted tilt sputtering," in *2017 IEEE Sensors Applications Symposium (SAS)* (IEEE, Glassboro, New Jersey, 13–15 March 2017) pp. 1–5.
[29]M. Kateb, E. Jacobsen, and S. Ingvarsson, "Application of an extended van der Pauw method to anisotropic magnetoresistance measurements of ferromagnetic films," J. Phys. D Appl. Phys. **52**, 075002 (2019).
[30]M. Kateb, H. Hajihoseini, J. T. Gudmundsson, and S. Ingvarsson, "Comparison of magnetic and structural properties of permalloy grown by dc and high power impulse magnetron sputtering," J. Phys. D Appl. Phys. **51**, 285005 (2018).
[31]J. T. Gudmundsson, N. Brenning, D. Lundin, and U. Helmersson, "The high power impulse magnetron sputtering discharge," Journal of Vacuum Science and Technology A **30**, 030801 (2012).
[32]J. Bohlmark, M. Lattemann, J. T. Gudmundsson, A. P. Ehiasarian, Y. A. Gonzalvo, N. Brenning, and U. Helmersson, "The ion energy distributions and ion flux composition from a high power impulse magnetron sputtering discharge," Thin Solid Films **515**, 1522–1526 (2006).
[33]D. Lundin, P. Larsson, E. Wallin, M. Lattemann, N. Brenning, and U. Helmersson, "Cross-field ion transport during high power impulse magnetron sputtering," Plasma Sources Science and Technology **17**, 035021 (2008).
[34]G. Greczynski, J. Lu, M. P. Johansson, J. Jensen, I. Petrov, J. E. Greene, and L. Hultman, "Role of Ti^{n+} and Al^{n+} ion irradiation (n = 1, 2) during $Ti_{1-x}Al_xN$ alloy film growth in a hybrid HIPIMS/magnetron mode," Surface and Coatings Technology **206** (2012).
[35]A. Schuhl, P. Galtier, O. Durand, J. R. Childress, and R. Kergoat, "Magnetic and transport properties of permalloy thin films grown by molecular beam epitaxy," Appl. Phys. Lett. **65**, 913–915 (1994).
[36]W. Price, "Electric potential and current distribution in a rectangular sample of anisotropic material with application to the measurement of the principal resistivities by an extension of van der Pauw's method," Solid-State Electronics **16**, 753–762 (1973).
[37]L. J. van der Pauw, "A method of measuring specific resistivity and hall effect of discs of arbitrary shape," Philips Research Reports **13**, 1–9 (1958).
[38]L. J. van der Pauw, "A method of measuring the resistivity and hall coefficient on the lamella of arbitrary shape," Philips Technical Review **20**, 220–224 (1958).
[39]J. Hornstra and L. J. van der Pauw, "Measurement of the resistivity constants of anisotropic conductors by means of plane-parallel discs of arbitrary shape," International Journal of Electronics **7**, 169–171 (1959).
[40]W. Price, "Extension of van der Pauw's theorem for measuring specific resistivity in discs of arbitrary shape to anisotropic media," Journal of Physics D: Applied Physics **5**, 1127 (1972).
[41]R. M. Bozorth, "Magnetoresistance and domain theory of iron-nickel alloys," Physical Review **70**, 923 (1946).
[42]T. McGuire and R. Potter, "Anisotropic magnetoresistance in ferromagnetic 3d alloys," IEEE Trans. Magn. **11**, 1018–1038 (1975).
[43]D. Lundin, N. Brenning, D. Jadernas, P. Larsson, E. Wallin, M. Lattemann, M. A. Raadu, and U. Helmersson, "Transition between the discharge regimes of high power impulse magnetron sputtering and conventional direct current magnetron sputtering," Plasma Sources Science and Technology **18**, 045008 (2009).
[44]C. Huo, M. A. Raadu, D. Lundin, J. T. Gudmundsson, A. Anders, and N. Brenning, "Gas rarefaction and the time evolution of long high-power impulse magnetron sputtering pulses," Plasma Sources Science and Technology **21**, 045004 (2012).
[45]C. W. T. McLyman, *Transformer and inductor design handbook*, 4th ed. (CRC Press, Boca Raton, Forida, 2011).
[46]J.-C. A. Huang, Y. M. Hu, C. C. Yu, C. H. Tsao, and C. H. Lee, "Structural and magnetic characterizations of hcp $Ni_{1-x}Fe_x$ ($0 < x < 20\%$) films," Physical Review B **57**, 11517 (1998).
[47]J. Yang, A. Barna, K. Makihara, M. Hashimoto, and P. B. Barna, "Growth structure and properties of Fe rich Fe-Ni alloy films deposited on MgO(001) by dc-biased plasma-sputtering," Thin Solid Films **347**, 85–90 (1999).
[48]S. Minakawa, M. Ohtake, M. Futamoto, F. Kirino, and N. Inaba, "Influence of composition on the crystal structure of Fe-Ni alloy epitaxial thin film deposited on Cr(211) underlayer," Journal of the Magnetics Society of Japan **40**, 137–147 (2016).
[49]T. Tanaka, M. Ohtake, F. Kirino, and M. Futamoto, "Microstructure of NiFe epitaxial thin films grown on MgO single-crystal substrates," IEEE Transactions on Magnetics **46**, 345–348 (2010).
[50]O. Dahl, "Cold-work deformation and recovery in alloys with orderly atom configuration," Zeitschrift Für Metallkunde **28**, 133 (1936).
[51]R. C. O'Handley, *Modern Magnetic Materials: Principles and Applications* (John Wiley & Sons, 2000).
[52]L. Chen, L. Andrea, Y. P. Timalsina, G.-C. Wang, and T.-M. Lu, "Engineering epitaxial-nanospiral metal films using dynamic oblique angle deposition," Cryst. Growth Des. **13**, 2075–2080 (2013).
[53]F. Cemin, D. Lundin, C. Furgeaud, A. Michel, G. Amiard, T. Minea, and G. Abadias, "Epitaxial growth of Cu (001) thin films onto Si (001) using a single-step HiPIMS process," Sci. Rep. **7**, 1655 (2017).
[54]A. Baltz, "Influence of vacuum conditions on epitaxially grown permalloy films," Journal of Applied Physics **34**, 1575–1580 (1963).
[55]N. Thangaraj, K. M. Krishnan, and R. Farrow, "Microstructure and giant magnetoresistance in granular and multilayer magnetic thin films," Scripta Metall. Mater. **33**, 1667–1677 (1995).
[56]F. M. Ross, K. M. Krishnan, N. Thangaraj, R. F. C. Farrow, R. F. Marks, A. Ceballada, S. S. P. Parkin, M. F. Toney, M. Huffman, C. P. De Araujo *et al.*, "Applications of electron microscopy in collaborative industrial research," MRS Bulletin **21**, 17–23 (1996).
[57]M. Ohtake, Y. Sato, J. Higuchi, T. Tanaka, F. Kirino, and M. Futamoto, "Epitaxial growth of metastable hcp-Ni and hcp-NiFe thin films on Au (100) fcc single-crystal underlayers and their structure characterization," Jpn. J. Appl. Phys. **50**, 103001 (2011).
[58]Z. Shi, H.-Y. Jiang, S.-M. Zhou, Y.-L. Hou, Q.-L. Ye, and M. Su Si, "Effect of band filling on anomalous Hall conductivity and magneto-crystalline anisotropy in NiFe epitaxial thin films," AIP Advances **6**, 015101 (2016).
[59]M. Romera, R. Ranchal, D. Ciudad, M. Maicas, and C. Aroca, "Magnetic properties of sputtered permalloy/molybdenum multilayers," Journal of Applied Physics **110**, 083910 (2011).
[60]E. F. Silva, M. A. Corrêa, R. D. Della Pace, C. C. P. Cid, P. R. Kern, M. Carara, C. Chesman, O. A. Santos, R. L. Rodríguez-Suárez, A. Azevedo *et al.*, "Thickness dependence of the magnetic anisotropy and dynamic magnetic response of ferromagnetic NiFe films," Journal of Physics D: Applied Physics **50**, 185001 (2017).
[61]A. Svalov, I. Aseguinolaza, A. Garcia-Arribas, I. Orue, J. Barandiaran, J. Alonso, M. Fernández-Gubieda, and G. Kurlyandskaya, "Structure and magnetic properties of thin permalloy films near the transcritical state," IEEE Trans. Magn. **46**, 333–336 (2010).
[62]R. Loloee and M. Crimp, "Effect of growth temperature on the structure and magnetic properties of sputtered biepitaxial (111) permalloy films," J. Appl. Phys. **92**, 4541–4544 (2002).
[63]T. Miyazaki, T. Ajima, and F. Sato, "Dependence of magnetoresistance on thickness and substrate temperature for 82Ni-Fe alloy film," Journal of Magnetism and Magnetic Materials **81**, 86–90 (1989).
[64]K. Fuchs, "The conductivity of thin metallic films according to the electron theory of metals," Mathematical Proceedings of the Cambridge Philosophical Society **34**, 100–108 (1938).

Paper V

Role of ionization fraction on the surface roughness, density, and interface mixing of the films deposited by thermal evaporation, dc magnetron sputtering, and HiPIMS: An atomistic simulation

M. Kateb, H. Hajihoseini, J. T. Gudmundsson and S. Ingvarsson 2019

Journal of Vacuum Science and Technology A 37 (3) 2019, 031306 (8pp)

Role of ionization fraction on the surface roughness, density, and interface mixing of the films deposited by thermal evaporation, dc magnetron sputtering, and HiPIMS: An atomistic simulation

Movaffaq Kateb,[1,a)] Hamidreza Hajihoseini,[1,2] Jon Tomas Gudmundsson,[1,2] and Snorri Ingvarsson[1]
[1]*Science Institute, University of Iceland, Dunhaga 3, IS-107 Reykjavik, Iceland*
[2]*Department of Space and Plasma Physics, School of Electrical Engineering and Computer Science, KTH Royal Institute of Technology, SE-100 44 Stockholm, Sweden*

(Received 1 March 2019; accepted 11 April 2019; published 30 April 2019)

The effect of ionization fraction on the epitaxial growth of Cu film on Cu (111) substrate at room temperature is explored. Three deposition methods, thermal evaporation, dc magnetron sputtering (dcMS), and high power impulse magnetron sputtering (HiPIMS) are compared. Three deposition conditions, i.e., fully neutral, 50% ionized, and 100% ionized flux were considered thermal evaporation, dcMS, and HiPIMS, respectively, for ~20 000 adatoms. It is shown that higher ionization fraction of the deposition flux leads to smoother surfaces by two major mechanisms, i.e., decreasing clustering in the vapor phase and bicollision of high energy ions at the film surface. The bicollision event consists of local amorphization which fills the gaps between islands followed by crystallization due to secondary collisions. The bicollision events are found to be very important to prevent island growth to become dominant and increase the surface roughness. Regardless of the deposition method, epitaxial Cu thin films suffer from stacking fault areas (twin boundaries) in agreement with recent experimental results. Thermal evaporation and dcMS deposition present negligible interface mixing while HiPIMS deposition presents considerable interface mixing. *Published by the AVS.*
https://doi.org/10.1116/1.5094429

I. INTRODUCTION

High power impulse magnetron sputtering (HiPIMS) is an ionized physical vapor deposition (PVD) technique that has attracted significant interest over the past two decades.[1,2] By pulsing the cathode target to a high power density with unipolar voltage pulses, at low duty cycle, and low repetition frequency, high electron density is achieved.[1–3] In conventional dc magnetron sputtering (dcMS), the plasma density is limited by the thermal load on the target and is usually on the order of $10^{15}-10^{17}$ per cubic meter,[4–6] and the ionization mean free path for the sputtered material is of the order of 50 cm.[3] Thus, the fraction of ionized species of the target material is, therefore, low, typically well below 10%.[7] Consequently, the majority of particles reaching the substrate surface are electrically neutral, and the ions are ions of the rare working gas. In HiPIMS, this problem is solved by applying high power impulses with a low duty cycle. The high power leads to peak electron densities exceeding 10^{19} m^{-3} in the vicinity of the cathode target.[8–10] The high density of electrons increases the probability for ionizing collisions between the sputtered atoms and energetic electrons and results in a high degree of ionization of the sputtered material. Values up to 70% have been reported for the ionization flux fraction in the case of Cu (Ref. 11), and copper ions have been observed to be dominant (up to 92%) in total ion fluxes to the substrate.[12] Besides the atoms and ions that collide with the substrate have energy distribution ranging 0–100 eV which is higher than that of dcMS deposition (0–40 eV).[12–14] As a result, HiPIMS presents denser,[15] smoother,[16,17] and void-free[18] coatings compared to conventional sputtering methods. In spite of huge theoretical and experimental efforts on understanding different aspects of HiPIMS deposition, the atomistic mechanisms that contribute to the film properties are not well demonstrated so far.

Atomistic simulations, namely, Monte Carlo (MC)[19–22] and molecular dynamics (MD),[23,24] have shown promise in the investigation of PVD processes owing to their atomistic resolution. In this regard, PVD in the absence of ions and vapor phase collisions has been extensively studied. However, most of these simulations only cover low energy PVD, similar to molecular beam epitaxy, where the evaporated species have energy in the 0.1–2 eV range.[25] The films deposited at such conditions and at relatively low temperatures are mainly suffering from porous and columnar microstructure[19,26,27] which is more pronounced in oblique deposition,[25–28] while the increased substrate temperature[25,29–32] and/or increased adatom energy[25,31,32] leads to a void-free film. This is mainly due to the fact that low energy deposition encourages island growth, but the growth mode changes to layer-by-layer (Frank–van der Merwe) growth as the incident atom energy is increased to 10 eV.[32,33] Further increase in energy of incident atoms (10–40 eV) causes interruption of layer-by-layer growth and leads to interface mixing between film and substrate.[32,34,35] Since the interface mixing has some similarities to the thermal spike in bulk ion mixing, energetic deposition is considered simplified model of sputter deposition in MD simulation.[34] For instance, it has been shown that pollution of

a)Author to whom correspondence should be addressed: mkk4@hi.is

sputtered flux with high energy atoms, as mimic of partially ionization flux, leads to amorphization of the film[36] and fully energetic deposition gives smooth amorphous film.[37]

An alternative method to model sputtering conditions is demonstrated in atomistic simulation of ion assisted PVD. Müller[20,21,23,24] was probably the first who considered a deposition using a flux consisting of both neutral adatoms and rare ions. He showed that bombarding the film with low energy rare ions removes bridging on top of the voids and thus leads to densification and texture refinement.[23,24] He studied the effect of rare ion to neutral ratio, the rare ion energy, and adatom energy on the void formation in the film which can be correlated to the tensile stress in the film. It has also been shown that ion-assisted PVD can cause texture refinement.[38,39] In addition, ion-assisted deposition can be used for more uniform deposition of Cu into trenches and vertical interconnect access (VIA).[40,41] Furthermore, it has been shown that for the case of Cu deposition, the ion energy has a major effect on the surface roughness compared to the ion incident angle.[42] More recently, Xie *et al.*[43] proposed a distribution function to mimic the kinetics energies of sputtered flux at the substrate surface in MD simulation. This allows a more realistic simulation but the method is still limited to a distribution function, e.g., Thompson.

In spite of these huge efforts, many of the above mentioned studies suffer from being performed in 2D,[23,24] using simplified force fields, e.g., hard sphere or Lennard-Jones,[26,27,35,38] and limited number of deposited species.[35] Thus, the previous studies were limited to only early stage of deposition, due to lack of computation power. There are also some studies on the accelerated simulation that are focused on the more realistic (slow) deposition rates.[28,44] The energy distribution in the flux has also been neglected which might be a reasonable assumption in thermal evaporation but it is necessary to include for the realization of ionized PVDs.[13] In addition, the effect of ionized flux on the film microstructure has never been discussed. Thus, they were unable to reflect ion–ion repulsion within the plasma as well as resputtering of the film due to bombardment of high energy ions.

The aim of the present study is to consider the effect of ionized flux of the deposition species as a major difference between evaporation, dcMS, and HiPIMS deposition in the MD framework. To this end, the film density, surface roughness, microstructure, and interface mixing are probed during film deposition at the atomic resolution.

II. METHOD

MD simulations were performed by solving Newton's equation of motion[45] using the large-scale atomistic/molecular massively parallel simulator (LAMMPS) open source code.[46–48]

The thermal evaporation flux, dcMS flux, and the HiPIMS flux were assumed to be fully neutral, 50% ionized, and fully ionized, respectively. The solid phase and neutrals interaction was modeled using embedded-atom method (EAM) potentials.[49,50] The total potential energy of atom i, E_i, is described by

$$E_i = F_i(\rho_i) + \frac{1}{2}\sum_{i\neq j}\phi_{ij}(r_{ij}), \tag{1}$$

where F_i is the embedding energy of atom i into electron density ρ_i and ϕ_{ij} is a pair potential interaction of atom i and j at distance r_{ij}. The multibody nature of the EAM potential is a result of the embedding energy term, i.e., ρ_i itself depends on electron density of neighboring atoms ρ_{ij},

$$\rho_i = \sum_{i\neq j}\rho_{ij}(r_{ij}). \tag{2}$$

The ion–ion interaction in the flux was modeled via Ziegler–Biersack–Littmark (ZBL)[51] (chap. 2) potential which takes into account both short range Coulombic interaction and long range screening

$$V(r_{ij}) = \frac{Z_i Z_j e^2}{4\pi\varepsilon_0 r_{ij}}\Phi\left(\frac{r_{ij}}{a}\right), \tag{3}$$

where Z_i and Z_j are the atomic numbers of ion i and ion j, respectively, the ions that belong to Coulombic term. e and ε_0 stand for elementary charge and vacuum permittivity, respectively.

The universal screening function in reduced unit is defined as

$$\Phi\left(\frac{r_{ij}}{a}\right) = \sum_{n=1}^{4} a_n e^{-c_n r_{ij}/a}, \tag{4}$$

where a is the ZBL modification of Bohr's universal reduced coordinate with 0.8853 derived from the Thomas-Fermi model

$$a = \frac{0.8853 a_0}{Z_i^{0.23} + Z_j^{0.23}}, \tag{5}$$

with a_0 being the Bohr radius and a_n is the normalizing factor, i.e., $\sum a_n = 1$

$$a_n = 0.18175, 0.50986, 0.28022, 0.02817,$$
$$c_n = 3.19980, 0.94229, 0.40290, 0.20162.$$

We would like to remark that the ZBL potential present 5% standard deviation from experimental values while the deviation for the popular Moliere potential can be very large (237%) (chap. 2).[51] The cutoff was considered to be 2.552 Å which is large enough to model sputtering,[52] and a switching function was also considered to smoothly ramp energy and force to zero at cutoff.

Ion-neutral and ion-film interactions were modeled using a hybrid based on both EAM and ZBL potentials. This allows resputtering from the film due to the repulsive force of the ZBL potential. Once an ion collides with the surface it may be either scattered back or it stabilizes at the surface. If it stands at the surface for a short time (1 ps) or implants into sublayers, it enters into the solid phase, and thus its interatomic potential is defined by EAM afterward. This may multiply the computation cost but it is necessary to realize

and retain deposition condition otherwise surface etching and incident ions scattering are expected.

The substrate was considered to be a single crystal Cu with its ⟨111⟩ orientation parallel to the growth direction, which means a (111) plane is exposed to the deposition flux. The initial configuration consisted of a fixed monolayer, a thermostat layer (3 monolayers), and a surface layer (12 monolayers) all with $77 \times 90\,\text{Å}^2$ lateral dimensions. The initial velocities of substrate atoms were defined randomly from a Gaussian distribution at the appropriate temperature of 300 K, and the substrate energy was minimized afterward.

For all deposition methods, the flux ratios of atoms/ions were inserted 150 nm above the substrate surface with random energy ranging 0–100 eV. We assumed a uniform distribution for all three deposition methods. In the case of dcMS, 50% ionization is expected to have the same energy distribution for ions and neutrals. The inserting process was a single atom/ion each 0.1 ps with initial velocity parallel to the substrate normal which gave a linear equal deposition rate in all cases. The HiPIMS deposition is normally performed using 50–400 μs long pulses[2] which is longer than the simulation times achieved in MD. Here, the impulse nature of HiPIMS was neglected, and deposition was assumed to remain for the entire time.

The time integration of the equation of the motion was performed regarding microcanonical ensemble (NVE) with a timestep of 5 fs. Since practical deposition is performed in the vacuum, the heat associated with particle's collision cannot be removed so efficiently, and hence the NVE ensemble provides a realistic representation of such systems. The Langevin thermostat[53] was only applied to the specified layer with a damping of 5 ps. It is worth mentioning that the damping is not due to the fact that Langevin thermostat does the time integration. But it modifies the forces instead which reproduce deceleration of ions implanted into the film with unique precision.

The first and simplest structure analysis is offered by $G(r)$ or pair correlation function written as

$$G(r) = \langle 4\pi r^2 \rho_a dr \rangle_T, \tag{6}$$

where ρ_a is the atom numbers density, r is the distance from reference particle, and dr determines the bin size. The angle brackets, i.e., $\langle\rangle_T$, denote time average at constant T.

The $G(r)$ describes how density varies as a function of distance in a system of particles from a reference particle. This results in a pattern of several peaks corresponding to number and distance of nearest neighbors (NNs) which applies to a wide range of materials. The amorphization as a result of ion bombardment causes variation in the density and can be detected by shifting and broadening of peaks in the $G(r)$ pattern. However, complex solid-state transition, such as fcc to hcp with constant coordination number and even distance, is very hard to determine with $G(r)$.

Common neighbor analysis (CNA) has shown to be a promising tool for structure characterization due to possibility of distinction between allotropic transitions and melting process. The CNA identifies the crystal structure of each atom based on the concept of bond-orientational order parameter (BOP) developed by Steinhardt *et al.*[54] Briefly, the CNA determines the local crystal structure based on the decomposition of the first NNs obtained from $G(r)$ in different angles.[55] Unlike to the BOP, CNA is sensitive to angles between pairs of NNs and can distinguish between fcc and hcp. Thus, a twin grain boundary can be determined based on slight angle difference between the first NNs, while it holds entire properties of an fcc atom.

The OVITO package[56] were used to generate atomistic illustrations.[57]

III. RESULTS AND DISCUSSION

A. Interface mixing

Figure 1 shows the Cu films in yellow deposited by the three different methods on an identical flat substrate indicated by red. For thermal evaporation and dcMS deposition shown in Figs. 1(a) and 1(b), no interface mixing is observed. It can be seen that the full ionization of the depositing species in HiPIMS effectively increases the interface mixing [see Fig. 1(c)]. Thus, it can be expected that HiPIMS deposited film present the highest adhesion to the substrate, while

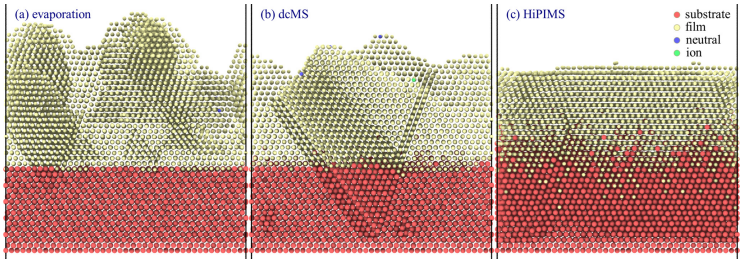

FIG. 1. Illustration of interface mixing using (a) thermal evaporation, (b) dcMS, and (c) HiPIMS after 2.5 ns deposition. To distinguish between film/substrate, the film atoms are illustrated with smaller diameter.

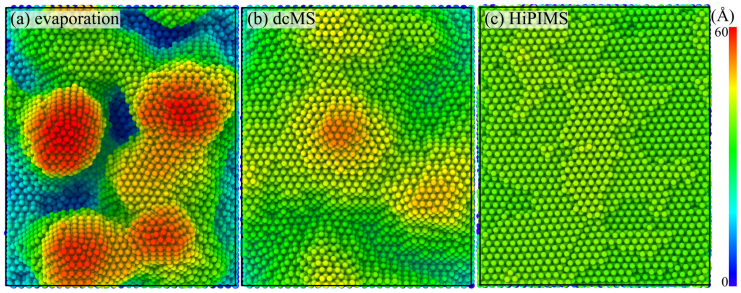

FIG. 2. Surface topology obtained using (a) thermal evaporation, (b) dcMS, and (c) HiPIMS deposition with similar deposition time and energy distribution. The deep blue indicates substrate surface and red denotes thickness higher than 6 nm.

thermal evaporation and dcMS present negligible difference in terms of adhesion. Moreover, better electrical contact can be expected due to interface mixing. It has been already shown using MC simulation that when an ion with a few hundreds of eV energy strikes the surface of a low density film, with less than 80% of theoretical density, it can penetrate to an average depth of a few nanometers.[20,21] In the case of our HiPIMS deposition, adatoms can be found maximum at 1.5 nm depth of substrate surface. This difference might be due to the fact that the previous MC simulation were performed in 2D, using Ar^+ ions and Moliere potential. The interface mixing has been found to be sensitive to the temporal lattice excitations localized in the vicinity of atom impacts.[34] In the present result, the interface mixing is associated with alternating localized amorphization and mixing due to energetic impacts. In dcMS deposition, limited number of energetic impacts occurs at the surface and interface mixing is negligible, while in HiPIMS deposition such event becomes dominant and thus interface mixing is considerable. These results are in agreement with the recent experimental comparison of Cu films deposited on Si with a native oxide using dcMS and HiPIMS.[58] At identical conditions, only Cu deposited by HiPIMS can pass through the native oxide and form epitaxial film.

B. Surface roughness

Figure 2 shows the top view of the films deposited by thermal evaporation, dcMS, and HiPIMS with identical deposition time and energy distribution. The dark blue here shows the substrate surface, and atoms that are 6 nm above the substrate are identified by red. It can be clearly seen that the thermal evaporated film presents very rough surface compared to the sputtered films. This is due to the fact that during thermal evaporation, neutral atoms form clusters before arriving at film/substrate surface. One may think that the surface roughness obtained in thermal evaporation here is an artificial effect of relatively high deposition rate or short simulation time compared to time required for surface diffusion. Such island growth has been reported for the deposition of Cu on Cu with experimental rate and modeling diffusion process through accelerated dynamic simulation.[28] Thus, the film obtained by thermal evaporation is extremely nonuniform at the atomic level. In the HiPIMS deposition, however, the repulsion between ions does not allow clustering when maximum uniformity of deposition occurs as can be seen in Fig. 2(c). Due to the distribution of energy in the flux, neutrals/ions with higher kinetic energy are able to diffuse longer at the surface than low energy adatoms. As a result, the formation of islands is still possible in the ionized flux case. The secondary mechanism here is energetic impacts of ions into subsurface atoms which causes local amorphization and fills the gaps between islands with atomically flat surface.

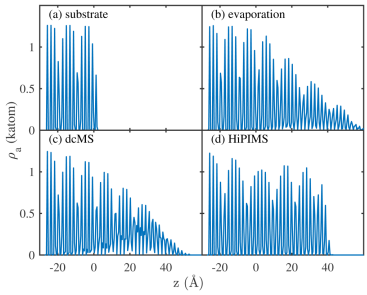

FIG. 3. Histogram of spatial distribution of atoms (atomic density, ρ_a) along the deposition direction with $z = 0$ being the substrate surface.

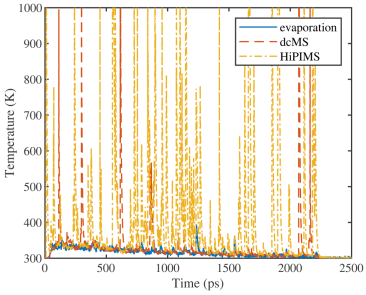

FIG. 4. Variation of temperature in the thermostat layer during deposition using thermal evaporation, dcMS, and HiPIMS.

The energetic ions themselves are the result of strong repulsive force between ions. Further collision of energetic ions causes recrystallization of amorphous regions which maintain smooth surface. We observed both of the above mentioned mechanisms, i.e., clustering and energetic collision during dcMS deposition that give an intermediate surface roughness as seen in Fig. 2(b).

Previously, it has been claimed that the only mechanism of redistribution of surface atoms is collapse of height advantaged islands at low energy deposition (~ 2 eV) and ballistic displacement of atoms at higher energies (in the 2–10 eV range).[33] We did not observe such mechanisms even during thermal evaporation which gives columns with an average cross section of ~ 3 and 6 nm height [cf. Fig. 2(a)]. In fact, the previous study was limited to two or three monolayer islands and thus was able to reflect the early stage of deposition. The second difference here arises from the fact that we applied a distribution of energy and ionization fraction to the flux which leads to more realistic result compared to flux with monodispersed energy.

C. Film density

In Fig. 3, the atomic density, ρ_a, is compared with the deposition direction, z, for the three deposition methods. The substrate pattern after relaxation shows very sharp transition at the surface $z = 0$ as seen in Fig. 3(a). A similar pattern is obtained after HiPIMS deposition which is known as a sign of layer-by-layer growth[23] as can be seen in Fig. 3(d). On the other hand, thermal evaporation and dcMS deposition result in a gradual decay which is a characteristic of island growth[33] as can be seen in Figs. 3(b) and 3(c), respectively.

D. Temperature

Figure 4 compares the variation of temperature with deposition time in thermal evaporation, dcMS, and HiPIMS deposition. It can be seen that during thermal evaporation, the temperature rises to ~ 340 K within the early stage of deposition and gradually decays to 300 K during the deposition. We observe local peaks in thermal evaporation that belong to clusters colliding to the substrate surface. However, the temperature variation related to cluster collision is very limited, ranging 10–20 K. In contrast, the sputtering methods consisted of several thermal spikes, some of them exceeding 1000 K. During the deposition of atoms with energy in the range of 0.1–10 eV, without ions, the thermal spikes are not sufficiently strong to cause redistribution of surface atoms.[33] Müller[20] showed by theoretical calculation that low energy ion impact can generate thermal spike and cause structure modification, although he used energetic Ar^+ ions with energy of 150 eV for demonstration of the effect. We did not observe any rearrangement at the surface due to small thermal peaks following cluster impacts. As mentioned before, we have noticed that the effect of thermal spikes is not only limited to the microstructure modification but also it is responsible for lower surface roughness obtained with the sputtering methods compared to the thermal evaporation. Since during HiPIMS deposition more thermal spikes occur than during dcMS deposition, it is expected to present a smoother surface (cf. Fig. 2) accordingly. This has indeed been observed experimentally.[16,17]

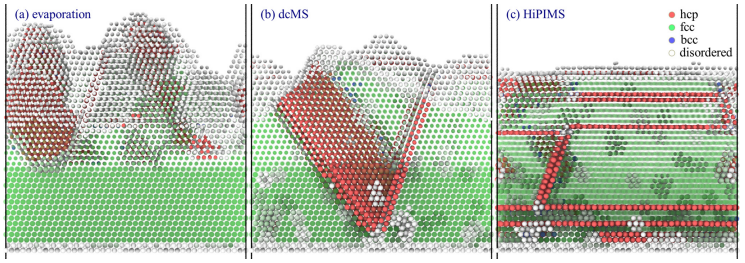

FIG. 5. Analysis of the local structure using CNA with red, green, and white, respectively, being fcc, hcp, and disordered atoms for (a) thermal evaporation, (b) dcMS, and (c) HiPIMS. To distinguish between film/substrate, the film atoms are illustrated with smaller diameter.

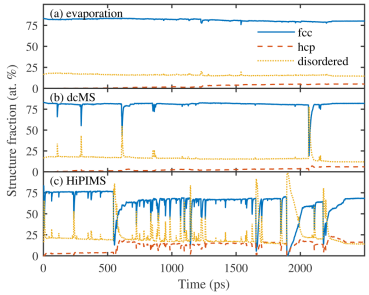

FIG. 6. Variation of fcc, hcp, and disordered fraction during deposition by (a) thermal evaporation, (b) dcMS, and (c) HiPIMS, respectively.

E. Microstructure

The microstructures obtained by the three different deposition methods are shown in Figs. 5(a)–5(c). The color contrast obtained by adoptive CNA which can distinguish between different crystal structures, i.e., fcc, hcp, bcc, and disordered atoms indicated by green, red, blue, and white, respectively. In the current simulation dimensions, all methods providing a single crystal Cu film aside from stacking faults (twin boundaries) and point defects. The formation of stable twin boundaries in the oblique deposition Cu on Cu (001) has been reported previously using accelerated MD simulation.[28] The existence of stacking fault areas has also been verified experimentally by polar mapping of the (111) planes in the epitaxial Cu deposited by thermal evaporation[59] and HiPIMS.[58] Also, we have recently demonstrated experimentally the existence of twin boundaries in epitaxial $Ni_{80}Fe_{20}$ (at. %) film deposited with both dcMS and HiPIMS.[60] Temporal formation of stacking faults and twin boundaries in the plane of Cu (111) during sputtering deposition was observed which has been reported previously during low energy deposition of Cu on Cu (111)[61] and Al on Cu (111).[62]

It is worth noting that during thermal evaporation, the substrate (indicated by bigger atoms) remains unchanged, whereas in the dcMS and HiPIMS deposition both stacking faults and point defects are introduced into the substrate. This essentially means utilizing ions in the deposition flux enables the modification of substrate structure in agreement with previous studies.[23,24,38] However, in these studies, the ions were considered to be Ar^+ whose impact gives smaller momentum than Cu^+ ions utilized here. Thus, in the previous studies, the structure modification was limited to densification[23,24] and reorientation of grains.[38]

F. High energy collisions

Figure 6 shows the variation of structure fraction during deposition by each method. At the early stage of deposition, the largest fraction is the fcc structure due to a single crystal substrate and minor fraction consists of disordered atoms, those located at the surface. During thermal evaporation, as shown in Fig. 6(a), these fractions are nearly constant except a slight increase in the fraction of hcp atoms which is associated with twin boundaries in the film [cf. Fig. 5(a)]. There are also some minor peaks in the fraction of disordered

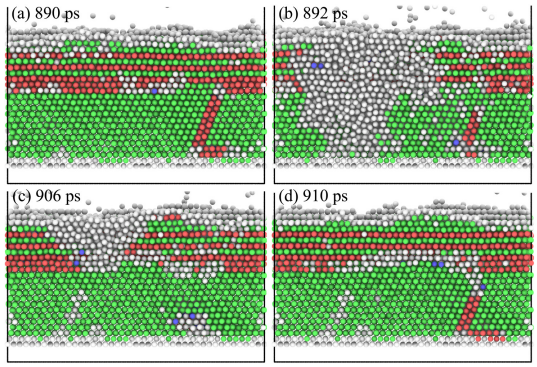

FIG. 7. Sequence of amorphization and crystallization during HiPIMS deposition due to high energy ion bombardment. (a) Before collision at 890 ps, (b) right after high energy collision at 892 ps, and (c)–(d) after secondary collisions at 906–910 ps. The red, green, blue, and white atoms, respectively, are fcc, hcp, bcc, and disordered atoms.

atoms and those are attributed to cluster impacts on the surface which generates temporary an amorphous phase at the cluster-film interface. The dcMS deposition also presents similar result except for the fact that the peaks in the fraction of disordered atoms become considerable as shown in Fig. 6(b). It is worth mentioning that the peaks observed here are due to impacts of high energy ions rather than clusters.

In contrast with thermal evaporation and dcMS, the initial fractions are not conserved during HiPIMS deposition as shown in Fig. 6(c). For instance, ~ 20% increase in hcp fraction is observed after a significant amorphization peak at 550 ps which is associated with ~ 20 % decrease in the fcc fraction. Unlike both thermal evaporation and dcMS, the peaks in the fraction of disordered atoms are associated with pits in both fcc and hcp fractions. This is due to the fact that the fraction of hcp atoms or stacking fault areas generated during HiPIMS deposition is much larger (~ 20 %) than for other methods. Thus, the hcp fraction can be affected by high energy ion bombardment.

Figure 7 shows the sequence of amorphization and crystallization events during HiPIMS deposition. Figure 7(a) shows the film before collision and which seems single crystalline aside from some stacking fault areas. In Fig. 7(b), it can be clearly seen that an amorphous region appears in the film deep down to the bottom of the substrate. The amorphization during bombardment has been reported previously.[36,38] As time passes, the amorphous phase disappears as shown in Figs. 7(c) and 7(d). It is worth noting that after amorphization and recrystallization the film microstructure has remained nearly unchanged.

IV. CONCLUSION

Using MD simulations, it is shown that HiPIMS deposition presents a smoother surface than less ionized deposition methods representing dcMS and thermal evaporation. It is shown that the surface roughness is the product of clustering in the vapor phase and island growth on the substrate surface. The former can be reduced by an increase in ionized flux fraction as a consequence of repulsion of ions of the same polarity. However, reducing island growth is more complex and it occurs through so-called bicollision of high energy ions. First, a high energy ion implants into sublayers and causes local amorphization which fills the gaps between islands. Secondary ion bombardment causes recrystallization and maintains a smooth surface. There is no high energy ion in the thermal evaporation which presents an extremely rough surface. However, during dcMS deposition, the number of bicollision events are rare as detected by thermal spikes in the film. As a result, the dcMS process presents an intermediate roughness between thermal evaporation and HiPIMS. In the HiPIMS, fully ionized flux increases the number of high energy ions significantly and the probability of bicollision events, and thus minimum surface roughness is achieved. This also contributes to interface mixing and gives superior adhesion in HiPIMS deposition compared to other methods.

ACKNOWLEDGMENTS

This work was partially supported by the University of Iceland Research Funds for doctoral students, the Icelandic Research Fund (Grant Nos. 196141, 130029, and 120002023), and the Swedish Government Agency for Innovation Systems (VINNOVA) (Contract No. 2014-04876).

[1]U. Helmersson, M. Lattemann, J. Bohlmark, A. P. Ehiasarian, and J. T. Gudmundsson, Thin Solid Films **513**, 1 (2006).
[2]J. T. Gudmundsson, N. Brenning, D. Lundin, and U. Helmersson, J. Vac. Sci. Technol. A **30**, 030801 (2012).
[3]J. T. Gudmundsson, Vacuum **84**, 1360 (2010).
[4]S.-H. Seo and H.-Y. Chang, J. Appl. Phys. **96**, 1310 (2004).
[5]J.-H. I. Sang-Hun Seo and H.-Y. Chang, Plasma Sources Sci. Technol. **15**, 256 (2006).
[6]P. Sigurjonsson and J. T. Gudmundsson, J. Phys. Conf. Ser. **100**, 062018 (2008).
[7]C. Christou and Z. H. Barber, J. Vac. Sci. Technol. A **18**, 2897 (2000).
[8]J. T. Gudmundsson, J. Alami, and U. Helmersson, Surf. Coat. Tech. **161**, 249 (2002).
[9]J. Bohlmark, J. T. Gudmundsson, J. Alami, M. Lattemann, and U. Helmersson, IEEE Trans. Plasma Sci. **33**, 346 (2005).
[10]S. M. Meier, A. Hecimovic, T. V. Tsankov, D. Luggenhölscher, and U. Czarnetzki, Plasma Sources Sci. Technol. **27**, 035006 (2018).
[11]V. Kouznetsov, K. Macák, J. M. Schneider, U. Helmersson, and I. Petrov, Surf. Coat. Tech. **122**, 290 (1999).
[12]J. Vlček, P. Kudláček, K. Burcalová, and J. Musil, EPL **77**, 45002 (2007).
[13]J. Bohlmark, M. Lattemann, J. T. Gudmundsson, A. P. Ehiasarian, Y. A. Gonzalvo, N. Brenning, and U. Helmersson, Thin Solid Films **515**, 1522 (2006).
[14]J. Lin, J. J. Moore, W. D. Sproul, B. Mishra, J. A. Rees, Z. Wu, R. Chistyakov, and B. Abraham, Surf. Coat. Tech. **203**, 3676 (2009).
[15]M. Samuelsson, D. Lundin, J. Jensen, M. A. Raadu, J. T. Gudmundsson, and U. Helmersson, Surf. Coat. Tech. **205**, 591 (2010).
[16]F. Magnus, A. S. Ingason, O. B. Sveinsson, S. Olafsson, and J. T. Gudmundsson, Thin Solid Films **520**, 1621 (2011).
[17]K. Sarakinos, J. Alami, and M. Wuttig, J. Phys. D Appl. Phys. **40**, 2108 (2007).
[18]J. Alami, P. O. Å. Persson, D. Music, J. T. Gudmundsson, J. Bohlmark, and U. Helmersson, J. Vac. Sci. Technol. A **23**, 278 (2005).
[19]K.-H. Müller, J. Appl. Phys. **58**, 2573 (1985).
[20]K.-H. Müller, J. Vac. Sci. Technol. A **4**, 184 (1986).
[21]K.-H. Müller, J. Appl. Phys. **59**, 2803 (1986).
[22]B. W. Dodson, Crit. Rev. Solid State **16**, 115 (1990).
[23]K.-H. Müller, Phys. Rev. B **35**, 7906 (1987).
[24]K.-H. Müller, J. Appl. Phys. **62**, 1796 (1987).
[25]X. Zhou, R. Johnson, and H. Wadley, Acta Mater. **45**, 1513 (1997).
[26]D. Henderson, M. H. Brodsky, and P. Chaudhari, Appl. Phys. Lett. **25**, 641 (1974).
[27]S. Kim, J. Henderson, and P. Chaudhari, Thin Solid Films **47**, 155 (1977).
[28]B. C. Hubartt, X. Liu, and J. G. Amar, J. Appl. Phys. **114**, 083517 (2013).
[29]M. Schneider, A. Rahman, and I. K. Schuller, Phys. Rev. Lett. **55**, 604 (1985).
[30]M. Schneider, I. K. Schuller, and A. Rahman, Phys. Rev. B **36**, 1340 (1987).
[31]R. W. Smith and D. J. Srolovitz, J. Appl. Phys. **79**, 1448 (1996).
[32]Q. Y. Zhang, J. Y. Tang, and G. Q. Zhao, Nucl. Instrum. Methods Phys. Res. B **135**, 289 (1998).
[33]C. M. Gilmore and J. A. Sprague, Phys. Rev. B **44**, 8950 (1991).
[34]J. A. Sprague and C. M. Gilmore, Thin Solid Films **272**, 244 (1996).
[35]E. Lugscheider and G. von Hayn, Surf. Coat. Tech. **116**, 568 (1999).
[36]J. Houska, Surf. Coat. Tech. **254**, 131 (2014).
[37]X. Chen, Y.-W. Wang, X. Liu, X.-Y. Wang, X.-B. Wang, S.-D. An, and Y.-Q. Zhao, Appl. Surf. Sci. **345**, 162 (2015).
[38]L. Dong and D. J. Srolovitz, J. Appl. Phys. **84**, 5261 (1998).
[39]L. Dong and D. J. Srolovitz, Appl. Phys. Lett. **75**, 584 (1999).
[40]C.-C. Hwang, G.-J. Huang, J.-G. Chang, and S.-P. Ju, J. Appl. Phys. **91**, 3569 (2002).
[41]C.-C. Hwang, J.-G. Chang, M.-H. Weng, and H.-C. Lin, J. Vac. Sci. Technol. B **21**, 2404 (2003).

[42]M.-H. Su and J.-M. Lu, Comput. Mater. Sci. **38**, 386 (2006).
[43]L. Xie, P. Brault, J.-M. Bauchire, A.-L. Thomann, and L. Bedra, J. Phys. D Appl. Phys. **47**, 224004 (2014).
[44]J. A. Sprague, F. Montalenti, B. P. Uberuaga, J. D. Kress, and A. F. Voter, Phys. Rev. B **66**, 205415 (2002).
[45]M. P. Allen and D. J. Tildesley, *Computer Simulation of Liquids* (Oxford University, Oxford, 1989).
[46]S. Plimpton, J. Comput. Phys. **117**, 1 (1995).
[47]S. J. Plimpton and A. P. Thompson, MRS Bull. **37**, 513 (2012).
[48]LAMMPS website, 2018, see: http://lammps.sandia.gov/.
[49]M. S. Daw and M. I. Baskes, Phys. Rev. Lett. **50**, 1285 (1983).
[50]M. S. Daw and M. I. Baskes, Phys. Rev. B **29**, 6443 (1984).
[51]J. Ziegler, J. Biersack, and U. Littmark, *The Stopping and Range of Ions in Matter* (Pergamon, New York, 1985), Vol. 1.
[52]K. K. Kammara, R. Kumar, and F. S. Donbosco, Comput. Part. Mech. **3**, 3 (2016).
[53]T. Schneider and E. Stoll, Phys. Rev. B **17**, 1302 (1978).
[54]P. J. Steinhardt, D. R. Nelson, and M. Ronchetti, Phys. Rev. B **28**, 784 (1983).
[55]H. Tsuzuki, P. S. Branicio, and J. P. Rino, Comput. Phys. Commun. **177**, 518 (2007).
[56]Ovito website, Version 2.9.0, see: http://ovito.org/.
[57]A. Stukowski, Model. Simul. Mater. Sci. Eng. **18**, 015012 (2009).
[58]F. Cemin, D. Lundin, C. Furgeaud, A. Michel, G. Amiard, T. Minea, and G. Abadias, Sci. Rep. **7**, 1655 (2017).
[59]L. Chen, L. Andrea, Y. P. Timalsina, G.-C. Wang, and T.-M. Lu, Cryst. Growth Des. **13**, 2075 (2013).
[60]M. Kateb, J. T. Gudmundsson, and S. Ingvarsson, AIP Adv. **9**, 035308 (2019).
[61]X. W. Zhou and H. N. G. Wadley, Acta Mater. **47**, 1063 (1999).
[62]Y. Cao, J. Zhang, T. Sun, Y. Yan, and F. Yu, Appl. Surf. Sci. **256**, 5993 (2010).

References

Alami, J., Petersson, P. O. A., Music, D., Gudmundsson, J. T., Bohlmark, J., and Helmersson, U. (2005). Ion-assisted physical vapor deposition for enhanced film deposition on non-flat surfaces. *Journal of Vacuum Science and Technology A*, 23(2):278–280.

Allen, M. P. and Tildesley, D. J. (1989). *Computer Simulation of Liquids*. Oxford University Press, Oxford.

Ašmontas, S., Kleiza, J., and Kleiza, V. (2008). A method for measuring the specific electrical conductivity of an anisotropically conductive medium. *Acta Physica Polonica A*, 113(6):1559–1569.

Auby, R. and Bernard, M. (1969). Principal of measuring resistivity in an anisotropic field. *Comptes rendus de l'Académie des Sciences B*, 268(20):1284.

Azzawi, S., Ganguly, A., Tokaç, M., Rowan-Robinson, R. M., Sinha, J., Hindmarch, A. T., Barman, A., and Atkinson, D. (2016). Evolution of damping in ferromagnetic/nonmagnetic thin film bilayers as a function of nonmagnetic layer thickness. *Physical Review B*, 93:054402.

Azzawi, S., Hindmarch, A., and Atkinson, D. (2017). Magnetic damping phenomena in ferromagnetic thin-films and multilayers. *Journal of Physics D: Applied Physics*, 50(47):473001.

Baltz, A. (1963). Influence of vacuum conditions on epitaxially grown permalloy films. *Journal of Applied Physics*, 34(6):1575–1580.

Barranco, A., Borras, A., Gonzalez-Elipe, A. R., and Palmero, A. (2016). Perspectives on oblique angle deposition of thin films: From fundamentals to devices. *Progress in Materials Science*, 76:59–153.

Beaurepaire, E., Merle, J.-C., Daunois, A., and Bigot, J.-Y. (1996). Ultrafast spin dynamics in ferromagnetic nickel. *Physical review letters*, 76(22):4250.

Bogart, L. (2010). *An investigation of the structure, pinning and magnetoresistance of domain walls in Ni_81Fe_19 planar nanowires*. PhD thesis, Durham University.

Bohlmark, J., Gudmundsson, J. T., Alami, J., Lattemann, M., and Helmersson, U. (2005). Spatial electron density distribution in a high-power pulsed magnetron discharge. *IEEE Transactions on Plasma Science*, 33(2):346–347.

Borup, K. A., Fischer, K. F., Brown, D. R., Snyder, G. J., and Iversen, B. B. (2015). Measuring anisotropic resistivity of single crystals using the van der pauw technique. *Physical Review B*, 92(4):045210.

Bozorth, R. M. (1946). Magnetoresistance and domain theory of iron-nickel alloys. *Physical Review*, 70(11-12):923.

Bozorth, R. M. (1956). *Ferromagnetism*. D. Van Nostrand, Princeton, New Jersey.

Bozorth, R. M., Dillinger, J. F., and Kelsall, G. A. (1934). Magnetic material of high

permeability attained by heat treatment in a magnetic field. In Severinghaus, W. L., editor, *Minutes of the Washington Meeting, April 26-28, 1934*, volume 45, pages 742–743. American Physical Society.

Buckley, O. and McKeehan, L. (1925). Effect of tension upon magnetization and magnetic hysteresis in permalloy. *Physical Review*, 26(2):261.

Cemin, F., Lundin, D., Furgeaud, C., Michel, A., Amiard, G., Minea, T., and Abadias, G. (2017). Epitaxial growth of Cu (001) thin films onto Si (001) using a single-step HiPIMS process. *Scientific Reports*, 7(1):1655.

Chason, E. and Mayer, T. M. (1997). Thin film and surface characterization by specular X-ray reflectivity. *Critical Reviews in Solid State and Materials Sciences*, 22(1):1–67.

Chen, L., Andrea, L., Timalsina, Y. P., Wang, G.-C., and Lu, T.-M. (2013). Engineering epitaxial-nanospiral metal films using dynamic oblique angle deposition. *Crystal Growth & Design*, 13(5):2075–2080.

Chen, M.-M., Gharsallah, N., Gorman, G. L., and Latimer, J. (1991). Ternary NiFeX as soft biasing film in a magnetoresistive sensor. *Journal of Applied Physics*, 69(8):5631–5633.

Chikazumi, S. (1950). Ferromagnetic properties and superlattice formation of iron-nickel alloys (I). *Journal of the Physical Society of Japan*, 5(5):327–333.

Chikazumi, S. (1956). Study of magnetic annealing on Ni_3Fe single crystal. *Journal of the Physical Society of Japan*, 11(5):551–558.

Chikazumi, S. (1961). Epitaxial growth and magnetic properties of single-crystal films of iron, nickel, and permalloy. *Journal of Applied Physics*, 32(3):S81–S82.

Chikazumi, S. (1964). *Physics of Magnetism*. John Wiley & Sons, New York.

Chikazumi, S. (1997). *Physics of Ferromagnetism*. Oxford University Press, New York, 2nd edition.

Chikazumi, S. and Oomura, T. (1955). On the origin of magnetic anisotropy induced by magnetic annealing. *Journal of the Physical Society of Japan*, 10(10):842–849.

Choe, G. (1999). Giant interface magnetostriction and temperature dependence in NiFe films encapsulated with Ta and Al_2O_3 layers. *IEEE Transactions on Magnetics*, 35(5):3838–3840.

Christou, C. and Barber, Z. H. (2000). Ionization of sputtered material in a planar magnetron discharge. *Journal of Vacuum Science and Technology A*, 18(6):2897–2907.

Collins, A. J., Prior, C. J., and Hicks, R. C. J. (1981). The magnetic properties of r.f.-sputtered permalloy and mumetal films. *Thin Solid Films*, 86(2–3):165–174.

Cullity, B. D. and Graham, C. D. (1972). *Introduction to Magnetic Materials*. John Wiley & Sons, 2nd edition.

Dahl, O. (1936). Cold-work deformation and recovery in alloys with orderly atom configuration. *Zeitschrift Für Metallkunde*, 28:133.

d'Aquino, M. (2004). *Nonlinear Magnetization Dynamics in Thin-Films and Nanoparticles*. PhD thesis, University of Naples.

den Broeder, F., Kuiper, D., van de Mosselaer, A., and Hoving, W. (1988). Perpendicular magnetic anisotropy of Co-Au multilayers induced by interface sharpening. *Physical Review Letters*, 60(26):2769.

Dong, L. and Srolovitz, D. J. (1998). Texture development mechanisms in ion beam assisted deposition. *Journal of Applied Physics*, 84(9):5261–5269.

Fuchs, K. (1938). The conductivity of thin metallic films according to the electron theory of metals. *Mathematical Proceedings of the Cambridge Philosophical Society*, 34(1):100–108.

Fujii, Y., Nakajima, K., Suzuki, M., and Kimura, K. (2014). Surface and interface roughness estimations by X-ray reflectivity and RBS measurements. *Surface and Interface Analysis*, 46(12-13):1208–1211.

Fujiwara, H. and Sugita, Y. (1968). Perpendicular anisotropy of evaporated magnetic films. *IEEE Transactions on Magnetics*, 4(1):22–25.

Ganguly, A., Azzawi, S., Saha, S., King, J. A., Rowan-Robinson, R. M., Hindmarch, A. T., Sinha, J., Atkinson, D., and Barman, A. (2015). Tunable magnetization dynamics in interfacially modified $Ni_{81}Fe_{19}$/Pt bilayer thin film microstructures. *Scientific Reports*, 5:17596.

Gradmann, U. and Müller, J. (1968). Flat ferromagnetic, epitaxial 48ni/52fe (111) films of few atomic layers. *Physica Status Solidi (B)*, 27(1):313–324.

Gudmundsson, J. T., Alami, J., and Helmersson, U. (2002). Spatial and temporal behavior of the plasma parameters in a pulsed magnetron discharge. *Surface and Coatings Technology*, 161(2-3):249–256.

Gudmundsson, J. T., Brenning, N., Lundin, D., and Helmersson, U. (2012). The high power impulse magnetron sputtering discharge. *Journal of Vacuum Science and Technology A*, 30(3):030801.

Hajihoseini, H., Kateb, M., Ingvarsson, S., and Gudmundsson, J. (2018). Effect of substrate bias on properties of HiPIMS deposited vanadium nitride films. *Thin Solid Films*, 663:126–130.

Hausmann, K., Hofmann, U., and Wolf, M. (1971). On the influence of atomic order in Ni_3Fe on the magnetic anisotropy and the electrical resistivity. *Physica Status Solidi (A)*, 6(1):161–164.

Helmersson, U., Lattemann, M., Bohlmark, J., Ehiasarian, A. P., and Gudmundsson, J. T. (2006). Ionized physical vapor deposition (IPVD): A review of technology and applications. *Thin Solid Films*, 513(1-2):1–24.

Hirayama, S., Kasai, S., and Mitani, S. (2017). Interface perpendicular magnetic anisotropy in ultrathin Ta/NiFe/Pt layered structures. *Japanese Journal of Applied Physics*, 57(1):013001.

Hornstra, J. and van der Pauw, L. J. (1959). Measurement of the resistivity constants of anistotropic conductors by means of plane-parallel discs of arbitrary shape. *International Journal of Electronics and Control*, 7(2):169–171.

Houska, J. (2014). Quantitative investigation of the role of high-energy particles in Al_2O_3 thin film growth: A molecular-dynamics study. *Surface and Coatings Technology*, 254:131–137.

Hubartt, B. C., Liu, X., and Amar, J. G. (2013). Large-scale molecular dynamics simulations of glancing angle deposition. *Journal of Applied Physics*, 114(8):083517.

Hubert, A. and Schäfer, R. (2008). *Magnetic domains: the analysis of magnetic microstructures*. Springer Science & Business Media.

Hubička, Z., Gudmundsson, J. T., Larsson, P., and Lundin, D. (2020). Ch 2 - Hardware and power management for high power impulse magnetron sputtering. In Lundin, D., Minea, T., and Gudmundsson, J. T., editors, *High Power Impulse Magnetron Sputtering*, pages 49 – 80. Elsevier.

Huo, C., Raadu, M. A., Lundin, D., Gudmundsson, J. T., Anders, A., and Brenning, N. (2012). Gas rarefaction and the time evolution of long high-power impulse magnetron sputtering pulses. *Plasma Sources Science and Technology*, 21(4):045004.

Johnson, M. T., Bloemen, P. J. H., Den Broeder, F. J. A., and de Vries, J. J. (1996). Magnetic anisotropy in metallic multilayers. *Reports on Progress in Physics*, 59(11):1409.

Kateb, M., Gudmundsson, J. T., and Ingvarsson, S. (2019a). Effect of atomic ordering on the magnetic anisotropy of single crystal $Ni_{80}Fe_{20}$. *AIP Advances*, 9(3):035308.

Kateb, M., Gudmundsson, J. T., and Ingvarsson, S. (2019b). Tailoring interface mixing and magnetic properties of Permalloy/Pt multilayers. In Banerjee, P., Gudmundsson, K., Lakhtakia, A., and Subramanyam, G., editors, *International Workshop on Thin Films for Electronics, Electro-Optics, Energy, and Sensors 2019*, volume 11371, page 1137101. International Society for Optics and Photonics, SPIE.

Kateb, M., Hajihoseini, H., Gudmundsson, J. T., and Ingvarsson, S. (2018). Comparison of magnetic and structural properties of permalloy grown by dc and high power impulse magnetron sputtering. *Journal of Physics D: Applied Physics*, 51(28):285005.

Kateb, M., Hajihoseini, H., Gudmundsson, J. T., and Ingvarsson, S. (2019c). Role of ionization fraction on the surface roughness, density, and interface mixing of the films deposited by thermal evaporation, dc magnetron sputtering, and HiPIMS: An atomistic simulation. *Journal of Vacuum Science and Technology A*, 37(3):031306.

Kateb, M. and Ingvarsson, S. (2017). Thickness-dependent magnetic and magnetoresistance properties of permalloy prepared by field assisted tilt sputtering. In *2017 IEEE Sensors Applications Symposium (SAS)*, pages 1–5, 13–15 March, Glassboro, New Jersey. IEEE.

Kateb, M., Jacobsen, E., and Ingvarsson, S. (2019d). Application of an extended van der Pauw method to anisotropic magnetoresistance measurements of ferromagnetic films. *Journal of Physics D: Applied Physics*, 52(7):075002.

Kaya, S. (1938). Die überstrukturbildung in den nickel= eisen legierungen und das permalloyproblem. *Journal of the Faculty of Science, Hokkaido Imperial University: Series 2 Physics*, 2(2):29–53.

Kaya, S. (1953). Uniaxial anisotropy of a permalloy crystal. *Review of Modern Physics*, 25(1):49.

Kench, J. R. and Schuldt, S. B. (1970). Concerning the origin of uniaxial magnetic anisotropy in electrodeposited permalloy films. *Journal of Applied Physics*, 41(8):3338–3346.

Kim, Y. and Silva, T. J. (1996). Magnetostriction characteristics of ultrathin permalloy films. *Applied Physics Letters*, 68(20):2885–2886.

Kirilyuk, A., Kimel, A. V., and Rasing, T. (2010). Ultrafast optical manipulation of magnetic order. *Review of Modern Physics*, 82(3):2731.

Kleiza, J., Sapagovas, M., and Kleiza, V. (2007). The extension of the van der pauw method to anisotropic media. *Informatica*, 18(2):253–266.

Kools, J. (1995). Effect of energetic particle bombardment during sputter deposition on the properties of exchange-biased spin-valve multilayers. *Journal of Applied Physics*, 77(7):2993–2998.

Kouznetsov, V., Macák, K., Schneider, J. M., Helmersson, U., and Petrov, I. (1999). A novel pulsed magnetron sputter technique utilizing very high target power densities. *Surface and Coatings Technology*, 122(2-3):290–293.

Kwon, H., Lee, S. H., and Kim, J. K. (2015). Three-dimensional metal-oxide nanohelix arrays fabricated by oblique angle deposition: fabrication, properties, and applications. *Nanoscale Research Letters*, 10(1):369.

Lundin, D., Brenning, N., Jadernas, D., Larsson, P., Wallin, E., Lattemann, M., Raadu, M. A., and Helmersson, U. (2009). Transition between the discharge regimes of high power impulse magnetron sputtering and conventional direct current magnetron sputtering. *Plasma Sources Science and Technology*, 18(4):045008.

Lutts, A. and Gielen, P. M. (1970). The order-disorder transformation in $FeNi_3$. *Physica Status Solidi (B)*, 41(1):K81–K84.

Magnus, F., Ingason, A. S., Olafsson, S., and Gudmundsson, J. T. (2012). Nucleation and resistivity of ultrathin TiN films grown by high power impulse magnetron sputtering. *IEEE Electron Device Letters*, 33(7):1045 – 1047.

Magnus, F., Ingason, A. S., Sveinsson, O. B., Olafsson, S., and Gudmundsson, J. T. (2011). Morphology of TiN thin films grown on SiO_2 by reactive high power impulse magnetron sputtering. *Thin Solid Films*, 520(5):1621–1624.

Mahieu, S., Ghekiere, P., Depla, D., and De Gryse, R. (2006). Biaxial alignment in sputter deposited thin films. *Thin Solid Films*, 515(4):1229–1249.

McGuire, T. and Potter, R. (1975). Anisotropic magnetoresistance in ferromagnetic 3d alloys. *IEEE Transactions on Magnetics*, 11(4):1018–1038.

Meier, S. M., Hecimovic, A., Tsankov, T. V., Luggenhölscher, D., and Czarnetzki, U. (2018). First measurements of the temporal evolution of the plasma density in HiPIMS discharges using THz time domain spectroscopy. *Plasma Sources Science and Technology*, 27(3):035006.

Miccoli, I., Edler, F., Pfnür, H., and Tegenkamp, C. (2015). The 100th anniversary of the four-point probe technique: the role of probe geometries in isotropic and anisotropic systems. *Journal of Physics: Condensed Matter*, 27(22):223201.

Montgomery, H. (1971). Method for measuring electrical resistivity of anisotropic materials. *Journal of applied physics*, 42(7):2971–2975.

Moreau-Luchaire, C. (2016). *Tailoring the interfacial properties of magnetic multilayers for the observation of skyrmions at room temperature*. PhD thesis, Université Paris-Saclay.

Müller, K.-H. (1986a). Model for ion-assisted thin-film densification. *Journal of Applied Physics*, 59(8):2803–2807.

Müller, K.-H. (1986b). Monte Carlo calculation for structural modifications in ion-assisted thin film deposition due to thermal spikes. *Journal of Vacuum Science and Technology A*, 4(2):184–188.

Néel, L. (1954). Superficial magnetic anisotropy and orientation superstructures. *Journal of Physics and Radium*, 15(4):225–239.

Néel, L. (1959). Directional order and diffusion aftereffect. *Journal of Applied Physics*, 30(4):S3–S8.

Néel, L., Pauleve, J., Pauthenet, R., Laugier, J., and Dautreppe, D. (1964). Magnetic properties of an iron—nickel single crystal ordered by neutron bombardment. *Journal of Applied Physics*, 35(3):873–876.

O'Handley, R. C. (2000). *Modern Magnetic Materials: Principles and Applications*. John Wiley & Sons.

Ohtake, M., Sato, Y., Higuchi, J., Tanaka, T., Kirino, F., and Futamoto, M. (2011).

Epitaxial growth of metastable hcp-Ni and hcp-NiFe thin films on Au (100) fcc single-crystal underlayers and their structure characterization. *Japanese Journal of Applied Physics*, 50(10R):103001.

Ohtani, T., Kawai, T., Ohtake, M., and Futamoto, M. (2013). Influence of crystallographic orientation on the magnetic properties of NiFe, Co, and Ni epitaxial fcc films grown on single-crystal substrates. *Journal of Korean Physical Society*, 63(3):778–783.

Pálsson, G. K., Rennie, A., and Hjörvarsson, B. (2008). Examination of the reliability of x-ray techniques for determining hydrogen-induced volume changes. *Physical Review B*, 78(10):104118.

Parkin, S., Mansour, A., and Felcher, G. (1991). Antiferromagnetic interlayer exchange coupling in sputtered Fe/Cr multilayers: Dependence on number of Fe layers. *Applied Physics Letters*, 58(14):1473–1475.

Parkin, S., More, N., and Roche, K. (1990). Oscillations in exchange coupling and magnetoresistance in metallic superlattice structures: Co/Ru, Co/Cr, and Fe/Cr. *Physical Review Letters*, 64(19):2304.

Parkin, S. S. P. (1991). Systematic variation of the strength and oscillation period of indirect magnetic exchange coupling through the 3d, 4d, and 5d transition metals. *Physical Review Letters*, 67:3598–3601.

Phuoc, N. N., Tee Soh, W., Chai, G., and Ong, C. (2013). Investigation of magnetic properties and microwave characteristics of obliquely sputtered NiFe/MnIr bilayers. *Journal of Applied Physics*, 113(7):073902.

Price, W. (1972). Extension of van der Pauw's theorem for measuring specific resistivity in discs of arbitrary shape to anisotropic media. *Journal of Physics D: Applied Physics*, 5(6):1127.

Price, W. (1973). Electric potential and current distribution in a rectangular sample of anisotropic material with application to the measurement of the principal resistivities by an extension of van der Pauw's method. *Solid-State Electronics*, 16(7):753–762.

Rijks, T. G., Lenczowski, S., Coehoorn, R., and de Jonge, W. (1997). In-plane and out-of-plane anisotropic magnetoresistance in $Ni_{80}Fe_{20}$ thin films. *Physical Review B*, 56(1):362–366.

Rodrigues, D. C. M., Klautau, A. B., Edström, A., Rusz, J., Nordström, L., Pereiro, M., Hjörvarsson, B., and Eriksson, O. (2018). Magnetic anisotropy in permalloy: Hidden quantum mechanical features. *Physical Review B*, 97:224402.

Ross, F. M., Krishnan, K. M., Thangaraj, N., Farrow, R. F. C., Marks, R. F., Cebollada, A., Parkin, S. S. P., Toney, M. F., Huffman, M., De Araujo, C. P., et al. (1996). Applications of electron microscopy in collaborative industrial research. *MRS Bulletin*, 21(5):17–23.

Rottmayer, R. E., Batra, S., Buechel, D., Challener, W. A., Hohlfeld, J., Kubota, Y., Li, L., Lu, B., Mihalcea, C., Mountfield, K., et al. (2006). Heat-assisted magnetic recording. *IEEE Transactions on Magnetics*, 42(10):2417–2421.

Samuelsson, M., Lundin, D., Jensen, J., Raadu, M. A., Gudmundsson, J. T., and Helmersson, U. (2010). On the film density using high power impulse magnetron sputtering. *Surface and Coatings Technology*, 205(2):591–596.

Sang-Hun Seo, J.-H. I. and Chang, H.-Y. (2006). Experimental investigation of plasma dynamics in dc and short-pulse magnetron discharges. *Plasma Sources Science and*

Technology, 15(2):256–265.

Schindler, A. and Salkovitz, E. (1960). Effect of applying a magnetic field during neutron irradiation on the magnetic properties of Fe–Ni alloys. *Journal of Applied Physics*, 31(5):S245–S246.

Seo, S.-H. and Chang, H.-Y. (2004). Electron transport in the downstream region of planar unbalanced magnetron discharge. *Journal of Applied Physics*, 96(3):1310–1317.

Sigurjonsson, P. and Gudmundsson, J. T. (2008). Plasma parameters in a planar dc magnetron sputtering discharge of argon and krypton. *Journal of Physics: Conference Series*, 100:062018.

Slonczewski, J. C. (1963). Magnetic annealing. In Rado, G. T. and Suhl, H., editors, *Magnetism*, volume 1, pages 205–242. Academic Press, New York.

Smith, D. O. (1959). Anisotropy in permalloy films. *Journal of Applied Physics*, 30(4):S264–S265.

Solovev, P., Izotov, A., and Belyaev, B. (2017). Microstructural and magnetic properties of thin obliquely deposited films: A simulation approach. *Journal of Magnetism and Magnetic Materials*, 429:45–51.

Solt, K. (1985). Magnetic, structural and magnetoresistive properties of magnetron-sputtered thin Ni–Fe films. *Thin Solid Films*, 125(3):251–256.

Song, O., Ballentine, C. A., and O'Handley, R. C. (1994). Giant surface magnetostriction in polycrystalline Ni and NiFe films. *Applied Physics Letters*, 64(19):2593–2595.

Sugita, Y., Fujiwara, H., and Sato, T. (1967). Critical thickness and perpendicular anisotropy of evaporated permalloy films with stripe domains. *Applied Physics Letters*, 10(8):229–231.

Sun, Y., Sullivan, C. R., Li, W., Kopp, D., Johnson, F., and Taylor, S. T. (2007). Soft magnetic properties of obliquely deposited Co–Zr–O films. *IEEE Transactions on Magnetics*, 43(12):4060–4063.

Svalov, A., Aseguinolaza, I., Garcia-Arribas, A., Orue, I., Barandiaran, J., Alonso, J., Fernández-Gubieda, M., and Kurlyandskaya, G. (2010). Structure and magnetic properties of thin permalloy films near the "transcritical" state. *IEEE Transactions on Magnetics*, 46(2):333–336.

Swartzendruber, L. (1964). Four-point probe measurement of non-uniformities in semiconductor sheet resistivity. *Solid-State Electronics*, 7(6):413–422.

Tanaka, T., Ohtake, M., Kirino, F., and Futamoto, M. (2010). Microstructure of NiFe epitaxial thin films grown on MgO single-crystal substrates. *IEEE Transactions on Magnetics*, 46(2):345–348.

Thangaraj, N., Krishnan, K. M., and Farrow, R. (1995). Microstructure and giant magnetoresistance in granular and multilayer magnetic thin films. *Scripta Metallurgica et Materialia*, 33(10-11):1667–1677.

Tiilikainen, J., Tilli, J.-M., Bosund, V., Mattila, M., Hakkarainen, T., Sormunen, J., and Lipsanen, H. (2007). Accuracy in x-ray reflectivity analysis. *Journal of Physics D: Applied Physics*, 40(23):7497.

Uhlir, A. (1955). The potentials of infinite systems of sources and numerical solutions of problems in semiconductor engineering. *Bell Labs Technical Journal*, 34(1):105–128.

Valdes, L. B. (1954). Resistivity measurements on germanium for transistors. *Proceedings of the IRE*, 42(2):420–427.

van der Pauw, L. J. (1958a). A method of measuring specific resistivity and Hall effect of discs of arbitrary shape. *Philips Research Reports*, 13(1):1–9.

van der Pauw, L. J. (1958b). A method of measuring the resistivity and Hall coefficient on the lamella of arbitrary shape. *Philips Technical Review*, 20(8):220–224.

van der Pauw, L. J. (1961). Determining of resistivity tensor and Hall tensor of anisotropic conductors. *Philips Research Reports*, 16:187–195.

Vartanyants, I., Ern, C., Donner, W., Dosch, H., and Caliebe, W. (2000). Strain profiles in epitaxial films from x-ray bragg diffraction phases. *Applied Physics Letters*, 77(24):3929–3931.

Velicu, I.-L., Neagu, M., Chiriac, H., Tiron, V., and Dobromir, M. (2012). Structural and magnetic properties of FeCuNbSiB thin films deposited by HiPIMS. *IEEE Transactions on Magnetics*, 48(4):1336 – 1339.

Vernyhora, I., Tatarenko, V., and Bokoch, S. (2012). Thermodynamics of fcc-Ni–Fe alloys in a static applied magnetic field. *ISRN Thermodynamics*, 2012.

Wan, X. J., Chen, Y. X., Chen, A. P., and Yan, S. R. (2005). The influence of atomic order on H_2-induced environmental embrittlement of Ni_3Fe intermetallics. *Intermetallics*, 13(5):454–459.

Wasscher, J. D. (1961). Note on four-point resistivity measurements on anisotropic conductors. *Philips Research Reports*, 16(4):301–306.

Wasscher, J. D. (1969). Electrical transport phenomena in MnTe, an antiferromagnetic semiconductor. *Philips Research Reports Supplements*, No. 8.

Woods, S. I., Ingvarsson, S., Kirtley, J. R., Hamann, H. F., and Koch, R. H. (2002). Local magnetic anisotropy control in NiFe thin films via ion irradiation. *Applied Physics Letters*, 81(7):1267–1269.

Yang, M. M. and Aboaf, J. A. (1989). rf-diode sputtered permalloy film. *Journal of Applied Physics*, 66(8):3734–3740.

Yelon, A., Voegeli, O., and Pugh, E. (1965). Switching properties of single-crystal Ni–Fe films. *Journal of Applied Physics*, 36(1):101–108.

Yin, L. F., Wei, D. H., Lei, N., Zhou, L. H., Tian, C. S., Dong, G. S., Jin, X. F., Guo, L. P., Jia, Q. J., and Wu, R. Q. (2006). Magnetocrystalline anisotropy in permalloy revisited. *Physical Review Letters*, 97(6):067203.

Zaumseil, P. (2015). High-resolution characterization of the forbidden Si 200 and Si 222 reflections. *Journal of Applied Crystallography*, 48(2):528–532.

7 Appendix MOKE

Two magneto-optic effects can distinguish one domain from another, either as a difference in color or in the degree of light and dark.

7.1 Kerr effect

This effect is a rotation of the plane of polarization of a light beam during reflection from a magnetized specimen. The amount of rotation is small, generally much less than one degree, and depends the material and on the direction and magnitude of the magnetization relative to the plane of incidence of the light beam. Specifically, the degree of rotation depends on the component of magnetization parallel to the direction of propagation of the light beam. Figure 7.1 shows the experimental arrangement. Light from a source passed through a polarizer which transmits only plane polarized light, or naturally polarized light from a laser, is incident on the specimen. For simplicity the specimen is assumed to contain only two domains, magnetized anti-parallel to each other as indicated by the arrows. During reflection the plane of polarization of beam 1 is rotated one way and that of beam 2 the other way, because they have encountered oppositely magnetized domains. The light then passes through an analyzer and into a low-power microscope. The analyzer is now rotated until it is "crossed" with respect to reflected beam 2; this beam is therefore extinguished and the lower domain appears dark. However, the analyzer in this position is not crossed with respect to beam 1, because the plane of polarization of beam 1 has been rotated with respect to that of beam 2. Therefore beam 1 is not extinguished, and the upper domain appears light.

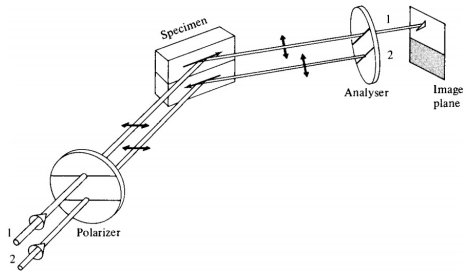

Figure 7.1. The principle of domain characterization by MOKE.

7.2 Faraday effect

This effect is a rotation of the plane of polarization of a light beam as it is transmitted through a magnetized specimen. The optical system is the same as the Kerr effect system, except that source, polarizer, specimen, analyzer, and microscope are all in line. The method is, of course, limited to specimens thin enough, or transparent enough, to transmit light; it is applied most often to thin sections of ferrimagnetic oxides, up to about 0.1 mm in thickness, although metallic films less than 400 Å thick have also been examined.

For thin sections of oxides, the amount of the Faraday rotation is a few degrees. This results in high contrast between adjoining domains and yields photographs of remarkable clarity. Like the Kerr method, the Faraday method is unrestricted as to temperature and is excellent for wall motion studies.